SYNTHESIS, CHARACTERIZATION AND APPLICATION OF METAL-ORGANIC FRAMEWORKS

BY

LINGJUAN SHEN

DISSERTATION

Submitted in the partial fulfillment of the requirements
for the degree of Doctor of Philosophy in Chemistry
in the Graduate College of the
University of Illinois at Urbana-Champaign, 2012

Urbana, Illinois

Doctoral Committee:

Professor Gregory S. Girolami, Chair
Professor Richard I. Masel
Professor Kenneth S. Suslick
Professor Andrew A. Gewirth

Abstract

Metal-organic frameworks (MOFs), also known as porous coordination polymers, are porous materials in which metal-containing nodes are connected by organic bridges. A larger variety of inorganic and organic components can be used to construct MOFs, and this versatility has enabled the rational design and assembly of materials having novel topologies and exceptional properties.

Luminescent MOFs are potentially useful as chemically-selective sensors. We have discovered a new luminescent MOF synthesized by treating Eu(III) ions with 2,2′-bipyridine-5,5′-dicarboxylic acid in *N*,*N*-diethylformamide (DEF). The X-ray crystal structure of the resulting material, $Eu_2(C_{12}H_6N_2O_4)_3(DEF)_4(H_2O)_5$, shows that it is a MOF with large channels (25×15 Å), and that the carboxylate groups but not the nitrogen atoms of the bipyridine units are bonded to the europium centers. Surface area measurements on the desolvated material confirmed that the material shows permanent porosity. When this material is exposed to 1,3,5-trinitrotoluene (TNT) or smaller nitroaromatics, the fluorescence of this MOF was significantly quenched. In contrast, 1,1-diphenyl-2-picrylhydrazine, a larger nitroaromatic, do not cause quenching.

Treatment of Zn(II) ions with 2,2′-bipyridine-5,5′-dicarboxylic acid and formic acid gives a different MOF, $Zn_3(C_{12}H_6N_2O_4)_2(O_2CH)_2 \bullet 2DEF$. Crystallographic studies show that this compound crystallizes in a chiral space group $P4_12_12$ by spontaneous resolution, although the specimen we examined was a racemic twin. Two of the zinc atoms are five-coordinate, whereas the other zinc atom has an octahedral coordination environment. The nano-pores, which have cross sections of 0.78×1.53 nm, are arranged in a herringbone fashion along the *c* axis.

The ability of MOFs to withstand high pressures is necessary for many of the most interesting potential applications of MOFs. We carried out a high pressure study of the metal organic framework Zn_4O(1,4-benzenedicarboxylate)$_3$ (IRMOF-1) up to 8.93 GPa, using a synchrotron radiation source and a diamond anvil cell. Both as-synthesized and desolvated samples of IRMOF-1 retained some crystallinity to 6.57 GPa (65 700 atm) and 4.32 GPa (43 2 00 atm), respectively. Both begin to convert to a new material even at pressures as low as 0.21 GPa; for the as-synthesized and desolvated material, this process is essentially complete at 8.33 and 5.17 GPa. The diffraction pattern suggests that pressure promotes a hydrolysis reaction; the water molecules necessary for this reaction were absorbed from the atmosphere during sample handling after desolvation. Some amorphization occurs along with the formation of the new phase.

Acknowledgments

First of all, I want to thank my advisors Gregory Girolami and Richard Masel for their guidance through my PhD research. I appreciate your precious time and valuable advice on my research and thesis. Also, I would like to thank my committee members Professor Kenneth Suslick and Professor Andrew Gewirth. I'm very grateful to have your helpful suggestions during my research.

Thanks to Danielle Gray from X-ray diffraction Lab for helping me collect and solve X-ray data. Thanks to Dr. Wenge Yang from Advanced Photon Source at Argonne National Lab for the high pressure studies. Thanks to Julio Soares from Center for Microanalysis of Materials. I also thank all the staff members of the School of Chemical Sciences for their excellent service.

Thanks to past Masel Group members Tianjiao Wu, Richard Ni, Matt Luebbers, Qingmei Chen, Nicolas Londono, Kevin Lin and Rob Morgan. Especially, I would like to thank Tianjiao Wu for teaching me all the experiment details and skills. I'm really missing all those joyful days we spent together. Thanks to the Girolami Group members Noel, Chang, Jennifer Steele, Luke Davis, Justin Mallek, Joseph Macor, Peter Sempsrott, Tracy Hitt, Brian Trinh and Mark Allen. Thank you very much for your help, advice and discussion on my research and job talks.

At last, I would like to thank my family. I'm very grateful to my Mom and Dad for always being supportive. Thank you to my little brother to take care of everything when I am far away from home.

Table of Contents

CHAPTER 1: A Review of Metal-Organic Frameworks

Introduction

Metal-organic frameworks (MOFs), also known as porous coordination polymers,[1-4] are a new class of zeolite-like hybrid solids. They are usually crystalline compounds built from organic multi-dentate organic ligands and metal ions or clusters. The two components are held together by covalent bonds to form extended 3-D infinite network structures. The chemistry of MOFs is developing at an extraordinary pace: in recent years, as shown by the increase in the number of published papers and reviews (Figure 1.1).[5] MOFs have exceptionally large surface areas and many have permanent porosity. The highest surface areas reported to date are over 6,000 m^2/g.[6, 7] MOFs usually are crystalline solids, so that the exact positions of all atoms in the framework can often be identified and correlated with the measured properties.

The synthesis of MOFs is conducted under relatively mild conditions. Many kinds of functional groups can be incorporated directly into the structure, a feature that is sometimes problematic for zeolites and carbon based porous materials. More importantly, the pore size, the pore shape, the network topology, and the surface functionalities can be tuned systematically, which means that the structures and properties of MOFs may be tailored to suit the needs of a specific application. Porosity coupled with other properties enables MOFs to be guest-responsive multifunctional materials.

In this chapter, the development of MOFs will be reviewed. The applications of MOFs in gas adsorption, sensing and catalysis will also be discussed.

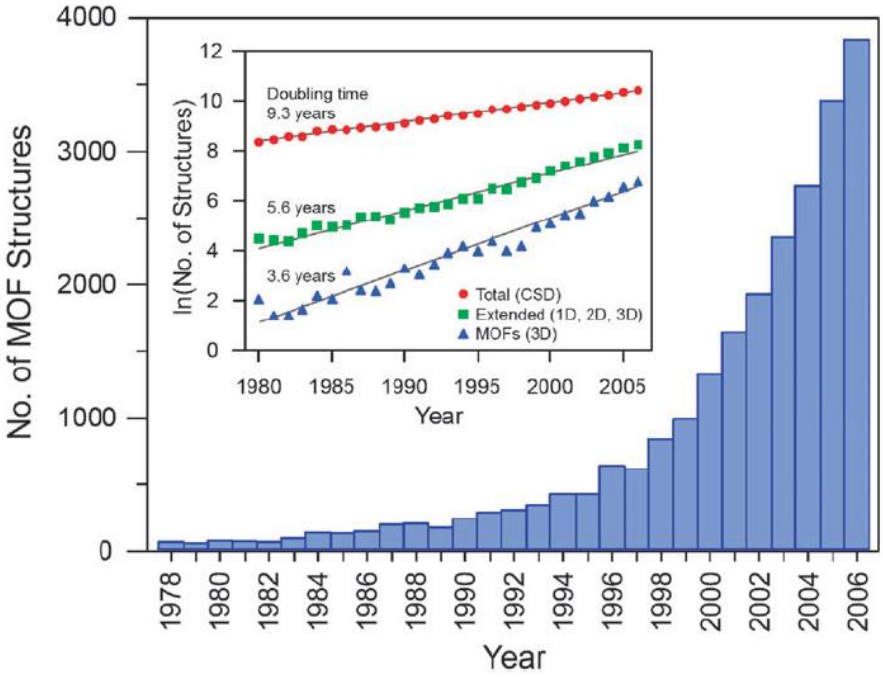

Figure 1.1. Number of metal–organic framework (MOF) structures reported in the Cambridge Structural Database (CSD) from 1978 through 2006.[5] The bar graph illustrates the recent dramatic increase in the number of reports, while the inset shows the natural log of the number of structures as a function of time, indicating the extraordinarily short doubling time for MOF structures compared to the total number of structures archived in the database.

Design and Synthesis of Metal-Organic Frameworks

MOFs are constructed from two key components: inorganic connectors and organic linkers. In principle, a wide range of structural, optical, electrical, magnetic, and catalytic properties can be incorporated into the frameworks by rational design.

Transition metal ions are often used as the inorganic components of MOFs. Different metal ions are well known to prefer different coordination numbers and geometries, such as linear, T- or Y-shaped, tetrahedral, square-planar, square-pyramidal, trigonal-bipyramidal, octahedral, trigonal-prismatic, and pentagonal-bipyramidal (Figure 1.2). For example, Cu(II) ions, which have d^9 electronic configurations, have a preference for square-planar and tetrahedral geometries, but can also be found with other coordination numbers, depending on the choice of ligand(s) and solvent(s).[8] Lanthanide ions are also often used to generate new and unusual network topologies due to their large coordination numbers (usually from 7 to 10).[9-12]

For the organic linker, there are a wide variety of choices as well. Ligands with rigid backbones are often preferred, because the rigidity makes it easier to predict the network geometry in advance of synthesis, and in addition the rigidity also helps to sustain the open-pore structure after the removal of the included solvent. The linkers can be electrically neutral, anionic, or cationic (Figure 1.3). The most frequently used neutral organic linkers are pyrazine and 4,4′-bipyridine (bpy).[13-15] These linkers are especially useful as pillars in the construction of pillared-layer in 3D networks.[16, 17] The most widely used anionic linkers are carboxylates,[18-23] because they have the ability to aggregate metal ions into clusters and thereby form more stable frameworks. Cationic organic ligands are relatively little used, owing to their low affinities for cationic metal ions.[24-26]

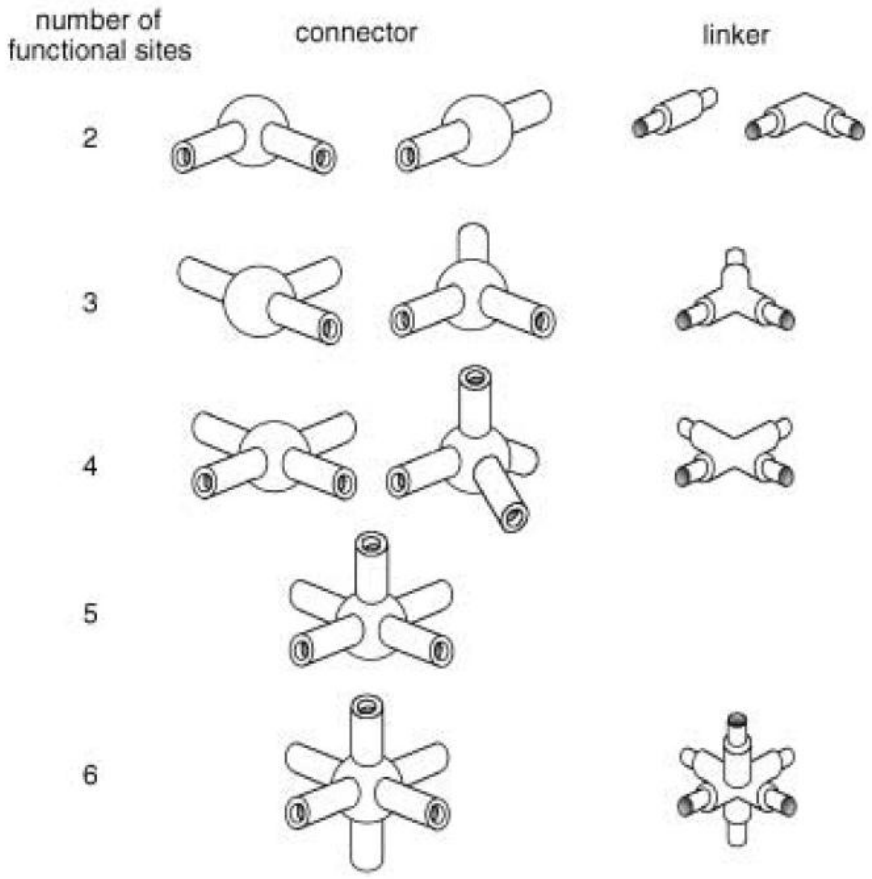

Figure 1.2. Components of MOFs.[4]

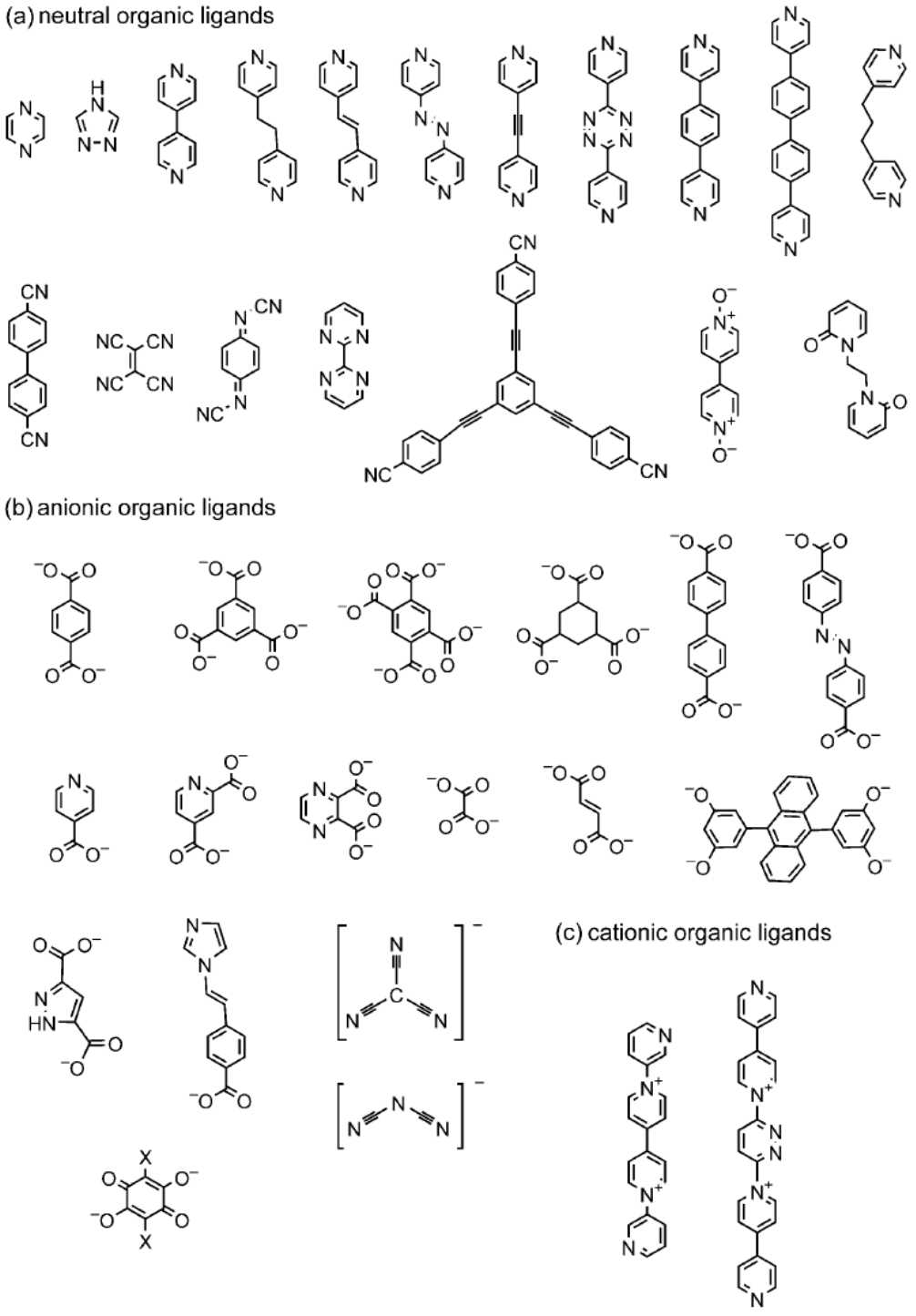

Figure 1.3. Examples of linkers used in MOFs.[4]

In most cases, MOFs are synthesized by means of solvothermal or hydrothermal methods,[27-31] in which the reactions are carried out in an organic solvent or in water at high-temperature in closed vessels. However, these methods typically require long reaction times, from several hours up to several months, depending upon the MOF of interest and the reaction solvent, reaction temperature, reagent concentrations, and other factors. A microwave-assisted process has been developed that allows the large scale synthesis of MOFs in a few minutes.[32-34] This method can also control the crystal size from near-millimeter down to sub-micrometer by manipulating the temperature and the concentration of reactants in solution.

In order to develop an environmentally friendly process, several researchers have studied the synthesis of MOFs under solvent-free condition.[35-37] The mechanochemical synthesis method involves the use of mechanical forces to drive the solventless reactions of metal oxides with organic ligands at room temperature using. In addition, the electrochemical synthesis of MOFs on the commercial scale is employed by BASF.[38] The metal ions are not introduced by adding metal salts, but instead are continuously generated by means of anodic dissolution. One advantage of this method is that it excludes unneeded anions during the syntheses, which contribute to the waste stream and can complicate the synthesis and purification. Basolite™ MOFs, which are manufactured by BASF by anodic dissolution, are currently being marketed by Sigma-Aldrich.

One of the key advantages of MOFs is the ability to integrate complex functionalities into the frameworks. Sometimes, however, installing functional groups of particular interest is hard to achieve during MOF synthesis, but fortunately incorporating the desired functionalities may be realized through post-synthetic modification (PSM), which is the chemical derivatization of

MOFs after their formation (Scheme 1.1a).[39] MOFs can be post-synthetically modified by means of several approaches, in which new functional groups are incorporated by means of non-covalent interactions,[40-42] coordinative interactions,[30, 43-45] or covalent interactions.[46-49] Some of the easiest methods to carry out PSM are protonation[46, 50] and doping.[51-53] Scheme 1.2b illustrates an example of PSM involving the zinc material IRMOF-3, which can be chemical modified with a diverse array of anhydrides and isocyanides. The advantages of the PSM method include: (1) the ability to incorporate a wider range of functional groups; (2) the ability to generate a series of functionally diverse MOFs with the same topology; (3) the ability to introduce multiple kinds of functional groups into the same framework.

Metal-Organic Frameworks for Gas storage and Separation

The energy needs of the US and the world are steadily increasing, which is leading to the steady depletion of fossil fuel reserves. Therefore, renewable ways to generate, store, and deliver energy are being intensively investigated. In addition, the currently is considerable public interest in ways to reduce carbon dioxide emissions, due to concerns about the implications of global warming.

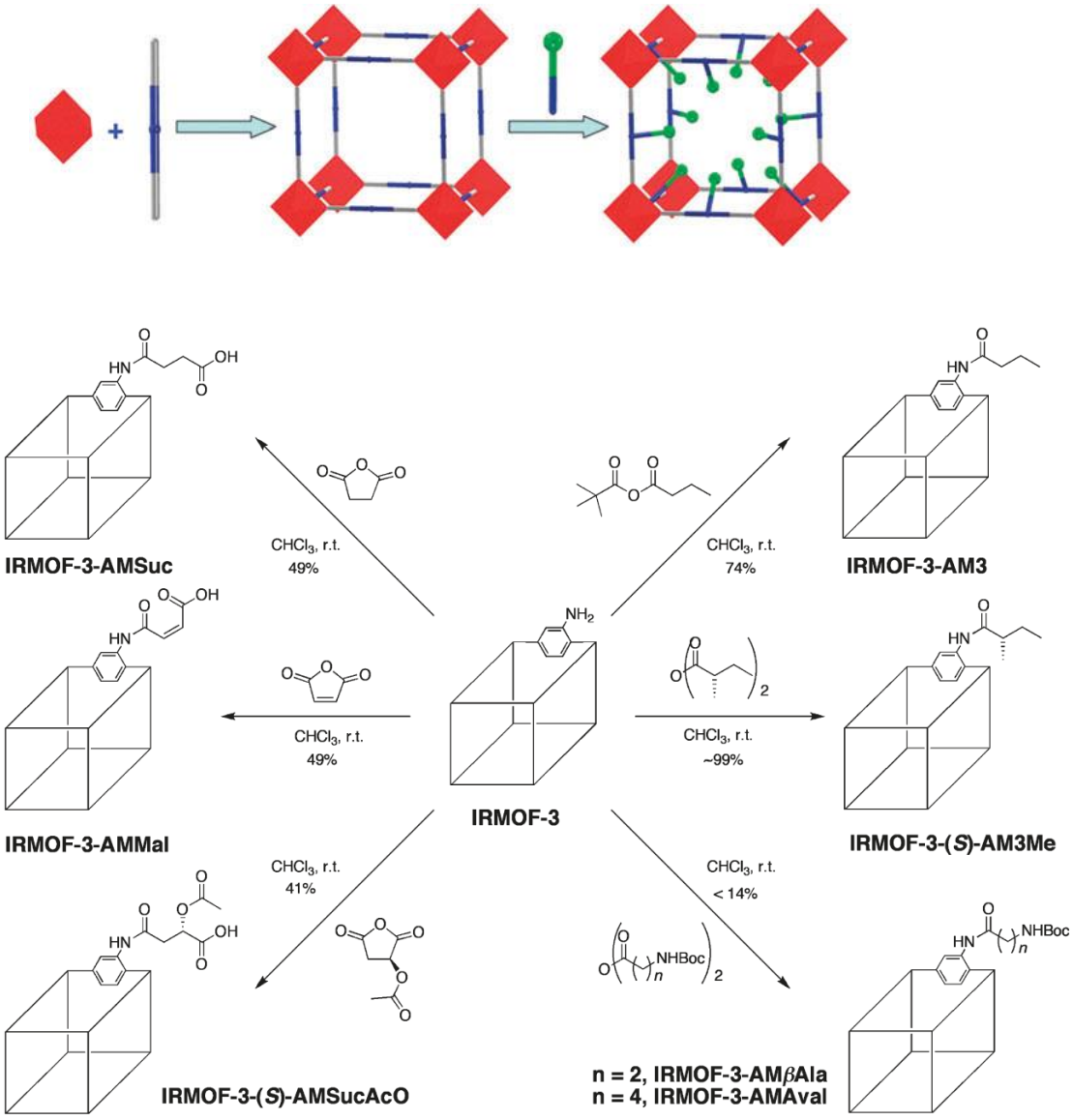

Scheme 1.1. (a) Examples of the post-synthetic modification of porous MOFs.[39] (b) Examples of post-synthetic modification reactions performed with IRMOF-3.[54]

Hydrogen has been considered as a near-ideal clean energy material due to its zero carbon content, and its high gravimetric energy density, which can nearly triple that of gasoline. Moreover, hydrogen can be generated from an almost inexhaustible resource -- water. One of the biggest bottlenecks to realizing a hydrogen economy is the lack of a safe, efficient, and economical on-board hydrogen storage system. In February 2009, the US department of Energy (DOE) set revised targets for a hydrogen storage system of 0.045 kg/kg for system gravimetric capacity and 0.028 kg/L for system volumetric capacity by the year 2010, and 0.055 kg/kg for system gravimetric capacity and 0.040 kg/L for system volumetric capacity by the year 2012. The ultimate targets are 0.075 kg/kg and 0.070 kg/L for gravimetric and volumetric storage, respectively. In addition, the storage system be able to operate between -40 and 85 °C and at pressures less than 100 bar, and should tolerate 1000 use-cycles by 2010 and 1500 use-cycles by 2015 (Table 1.1).[55]

Table 1.1. Revised DOE targets for on-board hydrogen storage systems.

Storage Parameters	Units	2010	2015	Ultimate
System Gravimetric Capacity (net useful energy/max. system mass)	kg H_2/kg system	0.045	0.055	0.075
System Volumetric Capacity (net useful energy/max. system volume)	kg H_2/L system	0.028	0.040	0.070
Min./max. delivery temperature	°C	−40/85	−40/85	−40/85
Cycle life (1/4 tank to full)	Cycles	1000	1500	1500
Max. delivery pressure from storage system	Atm (abs)	100	100	100
System fill time (for 5 kg H_2)	min	4.2	3.3	2.5

$Zn_4O(BDC)_3$ (BDC = 1,4-benzenedicarboxylate), also called IRMOF-1 or MOF-5, was one of the first MOFs investigated for hydrogen storage due to its high porosity, high surface area (4400 m^2/g), and stable structure in the absence of guest molecules.[56] The measured sorption isotherm for H_2 at 78 K reveals type I behavior, in which saturation is reached at low pressures followed by a pseudoplateau at higher pressures (Figure 1.4a). At 78 K and 1 bar, the H_2 uptake of IRMOF-1 is 4.5 weight percent, which corresponds to 17.2 H_2 per $Zn_4O(BDC)_3$ formula unit. At room temperature, the uptake of H_2 by IRMOF-1 increases linearly with pressure, and reaches 1.0 weight % at 20 bars (Figure 1.4b). Later research found that the H_2 uptake capacity of IRMOF-1 varies somewhat according to the method used to prepare and activate it.[56-66]

High-pressure hydrogen adsorption data at 77 K for selected porous MOFs are summarized in Table 1.2. Unfortunately, at room temperature most MOFs take up very little hydrogen even under high pressures, owing to the low interaction energy between the framework and physisorbed H_2, which has been modeled in several computational studies.[67-78] To overcome this problem, several researchers have made MOFs containing coordinatively unsaturated metal centers, which are able to chemisorb H_2 either as intact molecules or by oxidative addition.[79-82] This method has been shown to enhance the H_2 adsorption enthalpies.

Methane storage[83-85] and carbon dioxide capture by MOFs are also being intensively studied. A material called PCN-14, which contains copper(II) ions and 5,5′-(9,10-anthracene-diyl)di-isophthalate units, has the highest methane-adsorption capacity reported to date: 230 v/v at 290 K and 35 bar.[84] Carbon dioxide uptake has also been tested in other MOFs.[86, 87] One recent result is that CO_2 uptake can be greatly improved if pendant alkylamine functional groups are introduced into the pore surface of MOFs.[88, 89]

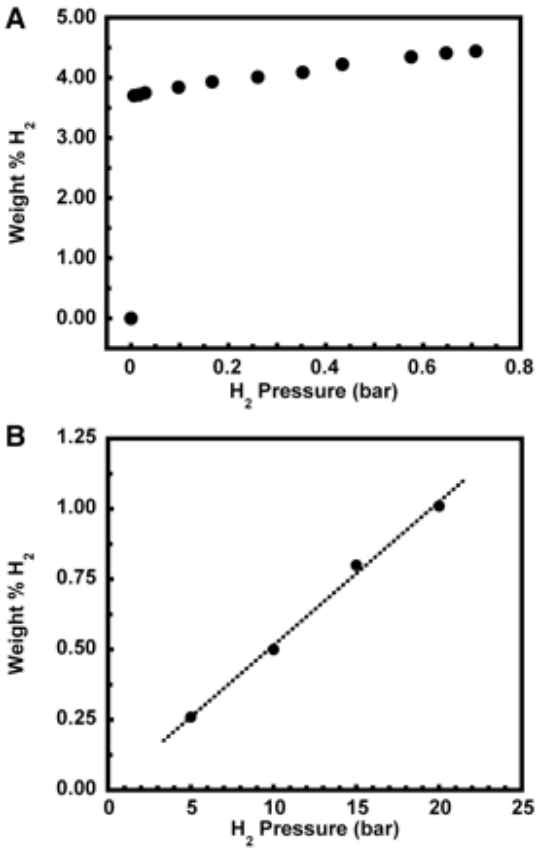

Figure 1.4. Hydrogen gas sorption isotherm for IRMOF-1 at (a) 78 K and (b) 298K.[56]

Table 1.2, High-pressure hydrogen adsorption data at 77K for selected porous MOFs.[90]

Compounds[a]	Surface area (m^2/g)		P/bar Excess (Absolute)	Gravimetric H_2 uptake (kg/kg)		Volumetric H_2 uptake (kg/L)	
	BET	Langmuir		Excess	Absolute	Excess	Absolute
$Ag_2[Ag_4(trz)_6]$, FMOF-1	810		77	0.0233		0.041	
Al(OH)(BDC), MIL-53 (Al)	1100	1590	16	0.038		0.037	
Cr(OH)(BDC), MIL-53 (Cr)	1100	1500	16	0.031			
$Cr_3OF(BTC)_2$, MIL-100		2700	90	0.0328		0.023	
$Cr_3OF(BDC)_3$, MIL-101		5900	80	0.061		0.0261	
Co(BDP)		2670	30	0.031			
$Co_2(BDC)_2(dabco)$	1595	2120	44	0.0411			
$HCu[(Cu_4Cl)_3(BTT)_8]$, Cu-BTT	1710	1770	30 (90)	0.042	0.057	0.038	0.053
Cu(dccptp)(NO_3)	268		20	0.0191		0.0239	
Cu_2(abtc), SNU-5		2850	50(50)	0.0522	0.0676	0.0378	0.0458
Cu_2(abtc), JUC-62			40	0.0471		0.0384	
Cu_2(aobtc), PCN-10	1407	1779	45(45)	0.042	0.0523	0.0322	0.0392
Cu_2(sbtc), PCN-11	1931	2442	45(45)	0.0504	0.0597	0.0378	0.0447
Cu_2(adip), PCN-14	1753	2176	45	0.0442		0.0366	
$Cu_2(BDC)_2(dabco)$	1300	1703	33.7	0.027			
$Cu_2(bpndc)_2(bpy)$, SNU-6		2910	70(70)	0.0487	0.1	0.0154	0.0316
Cu_2(bptc), MOF-505	1670	1830	20	0.0402		0.0373	
Cu_2(qptc), NOTT-101	2247		20 (60)	0.0607	0.06	0.0411	0.0431
Cu_2(tptc), NOTT-102	2942		20 (60)	0.0606	0.072	0.0436	0.0423
$Cu_2(C_{26}O_8H_{12})$, NOTT-103	2929		20 (60)	0.0651	0.0778		0.05
$Cu_2(C_{30}O_8H_{14})$, NOTT-110	2960		55 (55)	0.0543	0.0762		0.0468
$Cu_2(C_{30}O_8H_{16})$, NOTT-111	2930		48 (48)	0.0547	0.0736		0.0454
Cu_3(tdbb), NOTT-112	3800		40 (77)	0.0707	0.1		0.0503
$Cu_3(bhtc)_2$, UMCM-150	2300	3100	45	0.057		0.036	
$Cu_3(BTC)_2$, HKUST-1	1154	1958	50	0.036			
$Cu_3(tatb)_2$ (catenated), PCN-6		3800	50 (50)	0.072	0.095	0.0402	0.0528
$Cu_3(tatb)_2$ (non-catenated), PCN-6′		2700	50 (50)	0.042	0.058	0.0118	0.0162
$Cu_3(ttca)_2$, PCN-20	3525	4237	50	0.062			
$Cu_3[(Cu_4Cl)_3(tpb\text{-}3tz)_8]_2{\cdot}11CuCl_2$	1120	1200	30	0.028			
$Cu_4(TTPM)_2{\cdot}0.7CuCl_2$	2560	2745	20 (70)	0.041	0.056		0.041
$Cd_3(bpdc)_3$, JUC-48		880	40	0.028		0.02	
$Fe_3(OH)(pbpc)_3$	1200		20	0.0305		0.0331	
$Mn_3[(Mn_4Cl)_3(tpt\text{-}3tz)_8]_2$	1580	1700	25 (80)	0.037	0.045		0.037
$Mn_3[(Mn_4Cl)_3(BTT)_8]_2$, Mn-BTT	2100		50 (90)	0.051	0.069		0.06
$Ni(dhtp)_2$		1083	70	0.018			
$Ni_3(OH)(pbpc)_3$		1553	20	0.0415		0.0439	
$Ni_3O(adc)_3{\cdot}2(C_4H_{10}NO^+)$, PCN-19	723	823	48 (48)	0.0167	0.022	0.0159	0.021
$Sm_2Zn_3(oxdc)_6$	719		34	0.0119		0.0186	
$Zn(MeIM)_2$, ZIF-8	1630	1810	55	0.0301			
$Zn_2(abtc)(DMF)_2$, SNU-4		1460	50	0.037			
$Zn(NDC)(bpe)_{0.5}$		303	40	0.02			
Zn_2(dhtp), MOF-74, COP-27-Zn	950	1072	26	0.0221		0.0276	
$Zn_2(BDC)_2(dabco)$	1165	1488	83.2	0.0317			
$Zn_4O(FMA)_3$	1120	1618	39	0.052			
$Zn_4O(BDC)_3$, MOF-5, IRMOF-1	3800	4400	40 (100)	0.076	0.1	0.0421	0.066
$Zn_4O(BTB)_3$, MOF-177	4750	5640	66 (72)	0.076	0.112	0.032	0.048
$Zn_4O(dbdc)_3$, IRMOF-6	2804	3305	45	0.0463		0.0317	
$Zn_4O(hpdc)_3$, IRMOF-11	1984	2337	33.7	0.034		0.0267	
$Zn_4O(NDC)_3$, IRMOF-8		1818	15	0.036		0.0209	
$Zn_4O(ttdc)_3$, IRMOF-20	4024	4593	77.6	0.0625		0.0341	
$Zn_4O(T^2DC)(BTB)_{4/3}$, UMCM-2	5200	6060	46	0.0688			

[a] $abtc^{4-}$ = azobenzene-3,3′,5,5′-tetracarboxylate; $adip^{4-}$ = 5,5′-(9,10-anthracenediyl)di-isophthalate; adc^{2-} = 9,10-anthracenedicarboxylate; $aobtc^{4-}$ = azoxybenzene-3,3′,5,5′-tetracarboxylate; bdc^{2-} = 1,4-benzenedicarboxylate; BDP^{2-} = 1,4-benzenedipyrazolate; $bhtc^{3-}$ = biphenyl-3,4′,5-tricarboxylate; $bpdc^{2-}$ = 4,4′-biphenyldicarboxylate; bpe = 4,4′-*trans*-bis(4-pyridyl)-ethylene; $bpndc^{2-}$ = benzophenone-4,4′-dicarboxylate; $bptc^{4-}$ = 3,3′,5,5′-biphenyltetracarboxylate; bpy = 4,4′-bipyridine; H_3BTB = 1,3,5-tri(4-carboxyphenyl)benzene; BTC = benzenetricarboxylate; BTT^{3-} = 1,3,5-benzenetristetrazolate; dabco = 1,4-diazabicyclo[2.2.2]octane; $dbdc^{2-}$ = 1,2-dihydrocyclobutabenzene-3,6-dicarboxylate; H_4dhtp = 2,5-dihydroxyterephthalic acid; DMF = *N*,*N*′-dimethylformamide; FMA^{2-} = fumarate; $hpdc^{2-}$ = 4,5,9,10-tetrahydropyrene-2,7-dicarboxylate; $MeIM^-$ = 2-methylimidazole; NDC^{2-} = 2,6-naphthalenedicarboxylate; $oxdc^{2-}$ = oxydiacetate; $pbpc^{2-}$ = pyridine-3,5-bis(phenyl-4-carboxylate); $qptc^{4-}$ = quaterphenyl-3,3′′′,5,5′′′-tetracarboxylate; $sbtc^{4-}$ = *trans*-stilbene-3,3′,5,5′-tetracarboxylic acid; $tatb^{3-}$ = 4,4′,4′′-*s*-triazine-2,4,6-triyltribenzoate; T^2DC = thieno[3,2-*b*]thiophene-2,5-dicarboxylate; $tptc^{4-}$ = terphenyl-3,3′′,5,5′′-tetracarboxylate; $H_3tpb\text{-}3tz$ = 1,3,5-tri-*p*-(tetrazol-5-yl)phenyl-benzene; $H_3tpt\text{-}3tz$ = 2,4,6-tri-*p*-(tetrazol-5-yl)phenyl-*s*-triazine; trz^- = 1,2,4-triazolate; $ttdc^{2-}$ = thieno[3,2-*b*]thiophene-2,5-dicarboxylate; $ttpm^{4-}$ = tetrakis(4-tetrazolylphenyl)methane; ttca = triphenylene-2,6,10-tricarboxylate.

Metal-Organic Frameworks for Sensing

One important way to detect small amounts of an analyte of interest is luminescence quenching.[91] There are two basic types of luminescence. One is fluorescence, which is spin-allowed and has typical lifetimes about several nanoseconds. Another is phosphorescence, which is spin-forbidden and has lifetimes that can be as long as several seconds. A third type of light emission is scintillation, which is light emission stimulated by exposure to ionizing radiation.[92] Scintillation also has lifetimes on the order of 1 nanosecond.

There are several ways to make MOFs luminescent (Figure 1.5). The most common strategy is to incorporate luminescent inorganic metal centers. The most common choices for this property are lanthanide ions, especially Eu(III) and Tb(III), owing to the strong visible luminescence of these ions in the red and green regions, respectively. Although the electronic transitions of lanthanide ions are forbidden according to Laporte selection rules, which leads to weak absorbance and low quantum yields, the forbiddenness can be overcome by incorporating a strongly absorbing component called a lumophore into the MOF framework. When stimulated by irradiation, lumophores can transfer energy from their readily accessed triplet excited state to the Ln-emitting states, provided that there is strong vibronic coupling between the lumophore and the metal (Figure 1.6). This phenomenon is called the antenna effect, and it leads to a large increase in luminescence output by the lanthanide ion. Good organic lumophores are usually molecules with large conjugated pi systems. In the solid state, if lumophores are in close proximity, electronic interactions, such as ligand-to-ligand charge transfer, can affect the luminescence.[93]

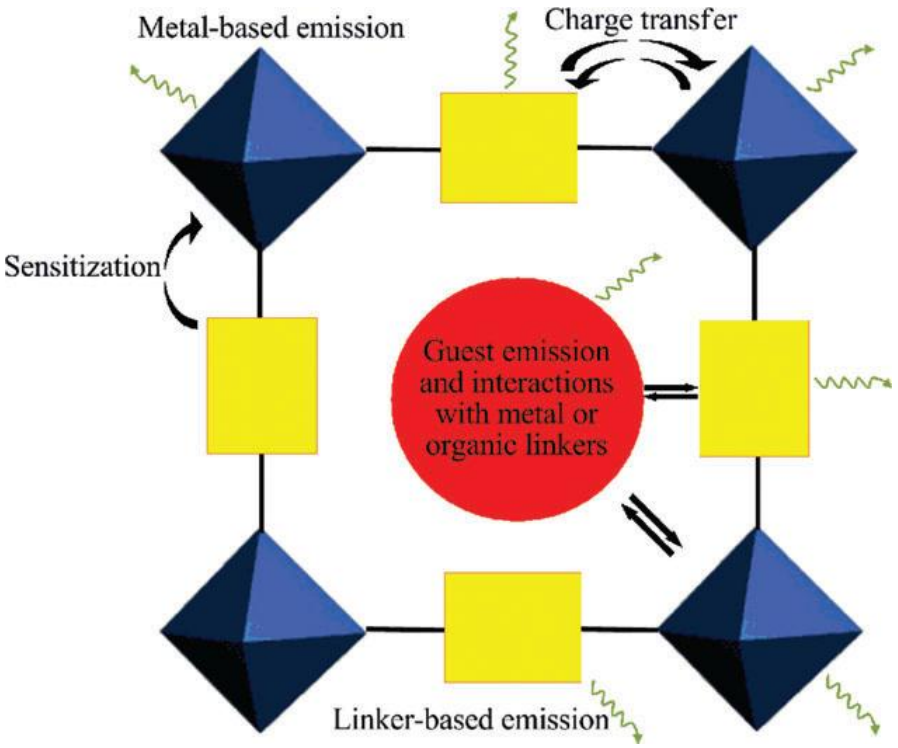

Figure 1.5. Representation of emission possibilities in a porous MOF, wherein metal clusters (blue octahedra) are linked by organic linkers (yellow rectangles) with an incorporated guest (red circle).[94]

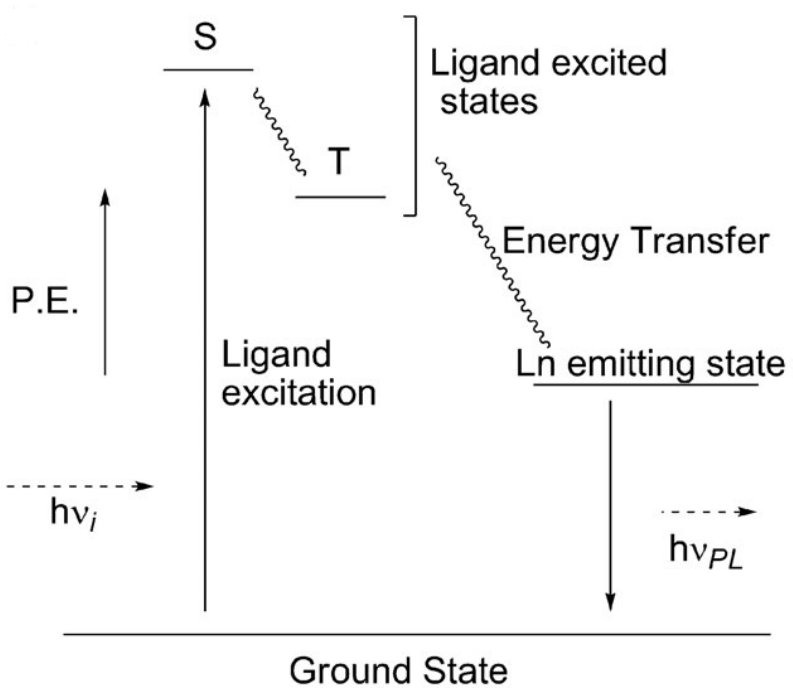

Figure 1.6. A schematic diagram of the antenna effect.[95]

Several different detection modes have been proposed as ways to use luminescent MOFs as potential sensors. One of these is wavelength shift: for example, the fluorescence emission wavelength of $Zn_4O(NTB)_2 \cdot 3DEF \cdot EtOH$ (H_3NTB = 4,4′,4′′-nitrilotrisbenzoic acid) shifts depending on the presence and identity of the guest molecules in the MOF.[96] The desolvation of this MOF leads to a blue-shift in the luminescence maximum due to the absence of π-π interactions between the interpenetration of nets.

Another detection mode employs intensity changes. The europium MOF Eu(BTC) exhibits a significant enhancement and quenching of it photoluminescence when it is exposed to DMF and acetone, respectively.[97] The same author later synthesized Tb(BTC) and $Eu(pdc)_{1.5}$ (pdc = pyridine-3,5-dicarboxylate), and showed that they are able to recognize and sense anions and metal ions, which bind to O-H groups and nitrogen atoms in the MOF, respectively.[98, 99] Luminescence quenching of MOFs has also been used in the detection of explosives. Li and coworkers developed a Zn-MOF that incorporates both 4,4′-biphenyldicarboxylate and 1,2-bipyridylethene linkers. The fluorescence of the MOF is quenched significantly by both 2,4-dinitrotoluene (DNT) and 2,3-dimethyl-2,3-dinitrobutane (DMNB) (Figure 1.7).[100]

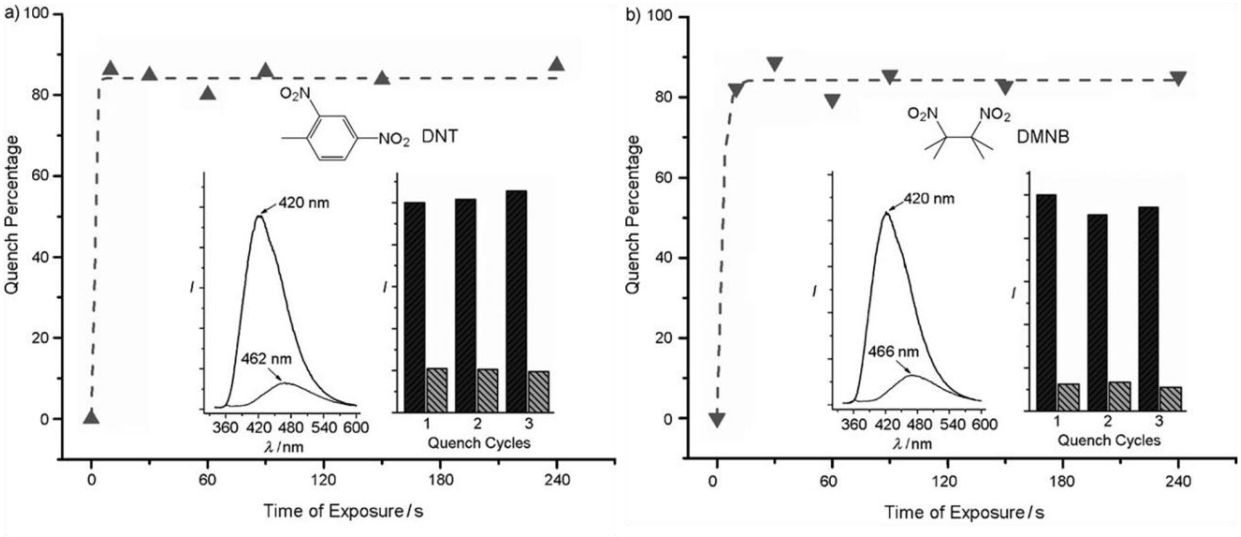

Figure 1.7. Time-dependent fluorescence quenching of a Zn MOF by (a) DNT (b) DMNB. The insets show the intensity change before and after exposing MOFs to explosive molecules for 10 seconds for the first three cycles.[100]

Metal-Organic Frameworks for Catalysis

MOFs can be used as heterogenenous catalysts. The well-defined pores and channels in MOFs enable them to be size- and shape-selective, much like zeolites, although the thermal stability of zeolites is much greater than that of MOFs. Despite this drawback, MOFs are promising materials as catalysts.

Catalytically active coordinately unsaturated metal sites can be introduced into MOFs in two ways, either as metal connecting points or as part of the linker (Scheme 1.2). As an example of the first approach, Long and coworkers synthesized a microporous MOF, $Mn_3[(Mn_4Cl)_3BTT_8(CH_3OH)_{10}]_2$ (H_3BTT = 1,3,5-benzenetristetrazol-5-yl), which can catalyze the transformation of selected aldehydes and ketones with cyanotrimethylsilane to the corresponding cyanosilylated products with high yield.[101] The unsaturated Mn^{2+} ions in the framework act as Lewis acid catalysts, and the MOF framework imposes size selectivity. An example of incorporating catalytically active metals into linkers is the synthesis of MOFs with metallophorphyrins. The PIZA-3 (porphyrinic illinois zeolite analogue-3), which is assembled from manganese(III) metalloporphyrins, is able to effect the catalytic hydroxylation of various linear and cyclic alkanes and the epoxidation of cyclic alkenes.[102] Recently, Hupp *et al.* reported a successful synthesis of MOFs with a variety of metallophorphyrins (containing Al^{3+}, Zn^{2+}, Pd^{2+}, Mn^{3+}, and Fe^{3+} ions).[103] They are all effective catalysts for the oxidation of alkenes and alkanes.

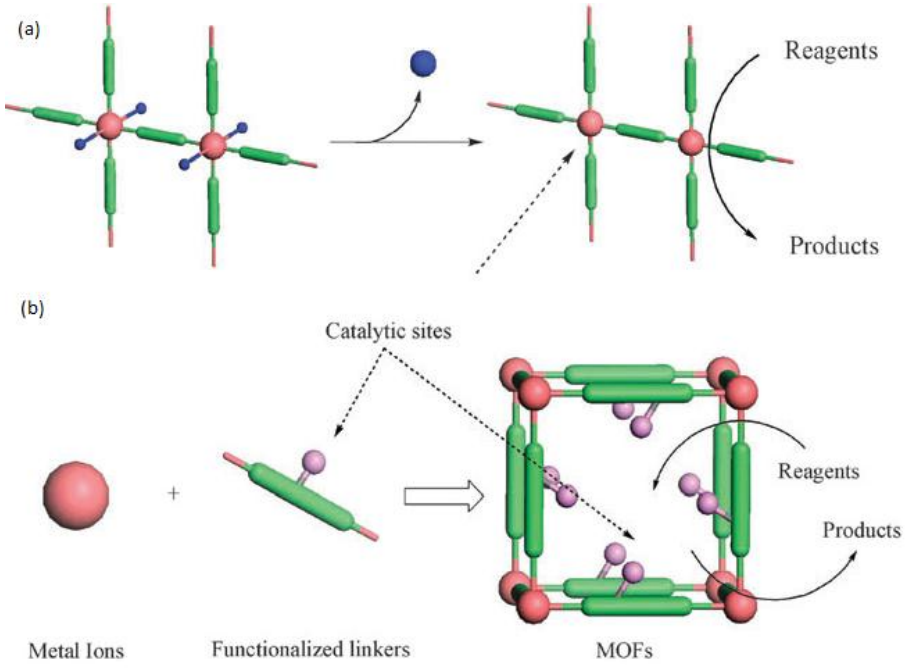

Scheme 1.2. (a) Coordinatively unsaturated metal connecting points as active catalytic sites. (b) Incorporation of active catalytic sites into the bridging ligands of MOFs.[104]

Much effort has been devoted to the development of homochiral MOFs able to serve as enantioselective catalysts. Homochiral MOFs can be synthesized from achiral components *via* self-resolution during crystal growth, or by enantioselective growth induced by chiral solvents, chiral templates, or chiral crystal seeds. [105-108] The more common way to construct chiral MOFs is to employ chiral organic ligands. Lin et al. synthesized a series of chiral MOFs from 1,1′-binaphthyl-derived chiral ligands, such as 1,1′-binaphthalene-2,2′-diol (BINOL) and, 2,2′-bis(diphenylphosphino)-1,1′-binaphthyl (BINAP).[109-111]

Despite the rapid and exciting development of MOFs, their commercial potential is still in its infancy. One obstacle is that many MOFs are not stable enough over long periods of use to be practical. Therefore, research needs to be carried out to overcome this obstacle.

References

1. S. R. Batten, S. M. Neville and D. R. Turner, *Coordination Polymers: Design, Analysis and Application*, 2008, 313-344.
2. K. Uemura, R. Matsuda and S. Kitagawa, *J. Solid State Chem.*, 2005, **178**, 2420-2429.
3. Z. Huang, H. B. Song, M. Du, S. T. Chen, X. H. Bu and J. Ribas, *Inorg. Chem.*, 2004, **43**, 931-944.
4. S. Kitagawa, R. Kitaura and S. Noro, *Angew. Chem., Int. Ed.*, 2004, **43**, 2334-2375.
5. J. R. Long and O. M. Yaghi, *Chem. Soc. Rev.*, 2009, **38**, 1213-1214.
6. H. Furukawa, N. Ko, Y. B. Go, N. Aratani, S. B. Choi, E. Choi, A. O. Yazaydin, R. Q. Snurr, M. O'Keeffe, J. Kim and O. M. Yaghi, *Science*, 2010, **329**, 424-428.

7. M. Hirscher, *Angew. Chem., Int. Ed.*, 2011, **50**, 581-582.

8. M. Wriedt and H. C. Zhou, *Dalton Trans.*, 2012, **41**, 4207-4216.

9. D. J. Hoffart and S. J. Loeb, *Angew. Chem., Int. Ed.*, 2005, **44**, 901-904.

10. X. D. Guo, G. S. Zhu, F. X. Sun, Z. Y. Li, X. J. Zhao, X. T. Li, H. C. Wang and S. L. Qiu, *Inorg. Chem.*, 2006, **45**, 2581-2587.

11. M. Gustafsson, A. Bartoszewicz, B. Martin-Matute, J. L. Sun, J. Grins, T. Zhao, Z. Y. Li, G. S. Zhu and X. D. Zou, *Chem. Mater.*, 2010, **22**, 3316-3322.

12. Q. F. Yang, X. B. Cui, Y. Chen, Z. Wang, J. H. Yu, J. Q. Xu and T. G. Wang, *Inorg. Chem. Commun.*, 2011, **14**, 320-323.

13. P. J. Hagrman, D. Hagrman and J. Zubieta, *Angew. Chem., Int. Ed.*, 1999, **38**, 2639-2684.

14. B. Moulton and M. J. Zaworotko, *Chem. Rev.*, 2001, **101**, 1629-1658.

15. M. J. Zaworotko, *Chem. Commun. (Cambridge, U. K.)*, 2001, 1-9.

16. P. Song, B. Liu, Y. Q. Li, J. Z. Yang, Z. M. Wang and X. G. Li, *CrystEngComm*, 2012, **14**, 2296-2301.

17. P. Pachfule, T. Panda, C. Dey and R. Banerjee, *CrystEngComm*, 2010, **12**, 2381-2389.

18. M. Eddaoudi, D. B. Moler, H. L. Li, B. L. Chen, T. M. Reineke, M. O'Keeffe and O. M. Yaghi, *Acc. Chem. Res.*, 2001, **34**, 319-330.

19. S. O. H. Gutschke, D. J. Price, A. K. Powell and P. T. Wood, *Angew. Chem., Int. Ed.*, 2001, **40**, 1920-1923.

20. T. J. Prior and M. J. Rosseinsky, *Chem. Commun. (Cambridge, U. K.)*, 2001, 495-496.

21. O. M. Yaghi, H. L. Li and T. L. Groy, *J. Am. Chem. Soc.*, 1996, **118**, 9096-9101.

22. H. Kumagai, C. J. Kepert and M. Kurmoo, *Inorg. Chem.*, 2002, **41**, 3410-3422.

23. M. E. Kosal, J. H. Chou, S. R. Wilson and K. S. Suslick, *Nat. Mater.*, 2002, **1**, 118-121.

24. J. Zhang, M. M. Matsushita, X. X. Kong, J. Abe and T. Iyoda, *J. Am. Chem. Soc.*, 2001, **123**, 12105-12106.

25. G. J. E. Davidson and S. J. Loeb, *Angew. Chem., Int. Ed.*, 2003, **42**, 74-77.

26. E. S. Lee, J. S. Heo and K. Kim, *Angew. Chem., Int. Ed.*, 2000, **39**, 2699-2701.

27. N. Stock and S. Biswas, *Chem. Rev.*, 2012, **112**, 933-969.

28. O. M. Yaghi and H. L. Li, *J. Am. Chem. Soc.*, 1995, **117**, 10401-10402.

29. W. B. Lin, Z. Y. Wang and L. Ma, *J. Am. Chem. Soc.*, 1999, **121**, 11249-11250.

30. S. S. Y. Chui, S. M. F. Lo, J. P. H. Charmant, A. G. Orpen and I. D. Williams, *Science*, 1999, **283**, 1148-1150.

31. D. N. Dybtsev, A. L. Nuzhdin, H. Chun, K. P. Bryliakov, E. P. Talsi, V. P. Fedin and K. Kim, *Angew. Chem., Int. Ed.*, 2006, **45**, 916-920.

32. Z. Ni and R. I. Masel, *J. Am. Chem. Soc.*, 2006, **128**, 12394-12395.

33. T. Chalati, P. Horcajada, R. Gref, P. Couvreur and C. Serre, *J. Mater. Chem.*, 2011, **21**, 2220-2227.

34. P. Silva, A. A. Valente, J. Rocha and F. A. A. Paz, *Cryst. Growth Des.*, 2010, **10**, 2025-2028.

35. W. B. Yuan, T. Friscic, D. Apperley and S. L. James, *Angew. Chem., Int. Ed.*, 2010, **49**, 3916-3919.

36. T. Friscic, D. G. Reid, I. Halasz, R. S. Stein, R. E. Dinnebier and M. J. Duer, *Angew. Chem., Int. Ed.*, 2010, **49**, 712-715.

37. A. Pichon and S. L. James, *CrystEngComm*, 2008, **10**, 1839-1847.

38. Mueller, U.; Puetter, H.; Hesse, M.; Wessel, H. WO 2005/049892.

39. Z. Q. Wang and S. M. Cohen, *Chem. Soc. Rev.*, 2009, **38**, 1315-1329.

40. B. F. Hoskins and R. Robson, *J. Am. Chem. Soc.*, 1990, **112**, 1546-1554.

41. Y. Liu, G. Li, X. Li and Y. Cui, *Angew. Chem., Int. Ed.*, 2007, **46**, 6301-6304.

42. M. Oh and C. A. Mirkin, *Angew. Chem., Int. Ed.*, 2006, **45**, 5492-5494.

43. C. D. Wu, A. Hu, L. Zhang and W. B. Lin, *J. Am. Chem. Soc.*, 2005, **127**, 8940-8941.

44. A. Vimont, J. M. Goupil, J. C. Lavalley, M. Daturi, S. Surble, C. Serre, F. Millange, G. Ferey and N. Audebrand, *J. Am. Chem. Soc.*, 2006, **128**, 3218-3227.

45. Y. K. Hwang, D. Y. Hong, J. S. Chang, S. H. Jhung, Y. K. Seo, J. Kim, A. Vimont, M. Daturi, C. Serre and G. Ferey, *Angew. Chem., Int. Ed.*, 2008, **47**, 4144-4148.

46. X. S. Wang, S. Q. Ma, D. F. Sun, S. Parkin and H. C. Zhou, *J. Am. Chem. Soc.*, 2006, **128**, 16474-16475.

47. K. K. Tanabe, Z. Q. Wang and S. M. Cohen, *J. Am. Chem. Soc.*, 2008, **130**, 8508-8517.

48. E. Dugan, Z. Q. Wang, M. Okamura, A. Medina and S. M. Cohen, *Chem. Commun. (Cambridge, U. K.)*, 2008, 3366-3368.

49. T. Haneda, M. Kawano, T. Kawamichi and M. Fujita, *J. Am. Chem. Soc.*, 2008, **130**, 1578-1579.

50. M. J. Ingleson, J. P. Barrio, J. Bacsa, C. Dickinson, H. Park and M. J. Rosseinsky, *Chem. Commun. (Cambridge, U. K.)*, 2008, 1287-1289.

51. K. L. Mulfort and J. T. Hupp, *J. Am. Chem. Soc.*, 2007, **129**, 9604-9605.

52. Y. W. Li and R. T. Yang, *J. Am. Chem. Soc.*, 2006, **128**, 726-727.

53. F. Schroeder, D. Esken, M. Cokoja, M. W. E. van den Berg, O. I. Lebedev, G. van Tendeloo, B. Walaszek, G. Buntkowsky, H. H. Limbach, B. Chaudret and R. A. Fischer, *J. Am. Chem. Soc.*, 2008, **130**, 6119-6130.

54. S. J. Garibay, Z. Q. Wang, K. K. Tanabe and S. M. Cohen, *Inorg. Chem.*, 2009, **48**, 7341-7349.

55. U.S. Department of Energy, Targets for on-board hydrogen storage systems: Current R&D focus is on 2015 targets with potential to meet ultimate targets (http://www1.eere.energy.gov/hydrogenandfuelcells/storage/current_technology.html).

56. N. L. Rosi, J. Eckert, M. Eddaoudi, D. T. Vodak, J. Kim, M. O'Keeffe and O. M. Yaghi, *Science*, 2003, **300**, 1127-1129.

57. S. S. Kaye, A. Dailly, O. M. Yaghi and J. R. Long, *J. Am. Chem. Soc.*, 2007, **129**, 14176-14177.

58. W. Zhou, H. Wu, M. R. Hartman and T. Yildirim, *J. Phys. Chem. C*, 2007, **111**, 16131-16137.

59. J. L. C. Rowsell, A. R. Millward, K. S. Park and O. M. Yaghi, *J. Am. Chem. Soc.*, 2004, **126**, 5666-5667.

60. B. Panella, M. Hirscher, H. Putter and U. Muller, *Adv. Funct. Mater.*, 2006, **16**, 520-524.

61. L. Pan, M. B. Sander, X. Y. Huang, J. Li, M. Smith, E. Bittner, B. Bockrath and J. K. Johnson, *J. Am. Chem. Soc.*, 2004, **126**, 1308-1309.

62. A. G. Wong-Foy, A. J. Matzger and O. M. Yaghi, *J. Am. Chem. Soc.*, 2006, **128**, 3494-3495.

63. B. Panella and M. Hirscher, *Adv. Mater.*, 2005, **17**, 538-541.

64. D. N. Dybtsev, H. Chun and K. Kim, *Angew. Chem., Int. Ed.*, 2004, **43**, 5033-5036.

65. J. Y. Lee, D. H. Olson, L. Pan, T. J. Emge and J. Li, *Adv. Funct. Mater.*, 2007, **17**, 1255-1262.

66. J. Liu, J. Y. Lee, L. Pan, R. T. Obermyer, S. Simizu, B. Zande, J. Li, S. G. Sankar and J. K. Johnson, *J. Phys. Chem. C*, 2008, **112**, 2911-2917.

67. R. C. Lochan and M. Head-Gordon, *Phys Chem Chem Phys*, 2006, **8**, 1357-1370.

68. T. Duren and R. Q. Snurr, *J. Phys. Chem. B*, 2004, **108**, 15703-15708.

69. H. Frost, T. Duren and R. Q. Snurr, *J. Phys. Chem. B*, 2006, **110**, 9565-9570.

70. H. Frost and R. Q. Snurr, *J. Phys. Chem. C*, 2007, **111**, 18794-18803.

71. E. Klontzas, A. Mavrandonakis, G. E. Froudakis, Y. Carissan and W. Klopper, *J. Phys. Chem. C*, 2007, **111**, 13635-13640.

72. E. Klontzas, A. Mavrandonakis, E. Tylianakis and G. E. Froudakis, *Nano Lett.*, 2008, **8**, 1572-1576.

73. E. Klontzas, E. Tylianakis and G. E. Froudakis, *J. Phys. Chem. C*, 2008, **112**, 9095-9098.

74. A. Mavrandonakis, E. Tylianakis, A. K. Stubos and G. E. Froudakis, *J. Phys. Chem. C*, 2008, **112**, 7290-7294.

75. S. S. Han, W. Q. Deng and W. A. Goddard, *Angew. Chem., Int. Ed.*, 2007, **46**, 6289-6292.

76. S. S. Han, H. Furukawa, O. M. Yaghi and W. A. Goddard, *J. Am. Chem. Soc.*, 2008, **130**, 11580-11581.

77. S. S. Han and W. A. Goddard, *J. Phys. Chem. C*, 2007, **111**, 15185-15191.

78. S. S. Han and W. A. Goddard, *J. Am. Chem. Soc.*, 2007, **129**, 8422-8423.

79. J. L. C. Rowsell and O. M. Yaghi, *Angew. Chem., Int. Ed.*, 2005, **44**, 4670-4679.

80. D. J. Collins and H. C. Zhou, *J. Mater. Chem.*, 2007, **17**, 3154-3160.

81. M. Dinca and J. R. Long, *Angew. Chem., Int. Ed.*, 2008, **47**, 6766-6779.

82. P. M. Forster, J. Eckert, B. D. Heiken, J. B. Parise, J. W. Yoon, S. H. Jhung, J. S. Chang and A. K. Cheetham, *J. Am. Chem. Soc.*, 2006, **128**, 16846-16850.

83. M. Eddaoudi, J. Kim, N. Rosi, D. Vodak, J. Wachter, M. O'Keeffe and O. M. Yaghi, *Science*, 2002, **295**, 469-472.

84. S. Q. Ma, D. F. Sun, J. M. Simmons, C. D. Collier, D. Q. Yuan and H. C. Zhou, *J. Am. Chem. Soc.*, 2008, **130**, 1012-1016.

85. I. Senkovska and S. Kaskel, *Microporous Mesoporous Mater.*, 2008, **112**, 108-115.

86. A. R. Millward and O. M. Yaghi, *J. Am. Chem. Soc.*, 2005, **127**, 17998-17999.

87. P. L. Llewellyn, S. Bourrelly, C. Serre, A. Vimont, M. Daturi, L. Hamon, G. De Weireld, J. S. Chang, D. Y. Hong, Y. K. Hwang, S. H. Jhung and G. Ferey, *Langmuir*, 2008, **24**, 7245-7250.

88. Y. S. Bae, O. K. Farha, J. T. Hupp and R. Q. Snurr, *J. Mater. Chem.*, 2009, **19**, 2131-2134.

89. A. Demessence, D. M. D'Alessandro, M. L. Foo and J. R. Long, *J. Am. Chem. Soc.*, 2009, **131**, 8784-8785.

90. S. Q. Ma and H. C. Zhou, *Chem. Commun. (Cambridge, U. K.)*, 2010, **46**, 44-53.

91. M. D. Allendorf, C. A. Bauer, R. K. Bhakta and R. J. T. Houk, *Chem. Soc. Rev.*, 2009, **38**, 1330-1352.

92. F. P. Doty, C. A. Bauer, A. J. Skulan, P. G. Grant and M. D. Allendorf, *Adv. Mater.*, 2009, **21**, 95-101.

93. J. C. Dai, X. T. Wu, Z. Y. Fu, C. P. Cui, S. M. Hu, W. X. Du, L. M. Wu, H. H. Zhang and R. O. Sun, *Inorg. Chem.*, 2002, **41**, 1391-1396.

94. M. D. Allendorf, C. A. Bauer, R. Bhakta and R. Houk, *Chem. Soc. Rev.*, 2009, **38**, 1330-1352.

95. N. Sabbatini, M. Guardigli and J. M. Lehn, *Coord. Chem. Rev.*, 1993, **123**, 201-228.

96. E. Y. Lee, S. Y. Jang and M. P. Suh, *J. Am. Chem. Soc.*, 2005, **127**, 6374-6381.

97. B. L. Chen, Y. Yang, F. Zapata, G. N. Lin, G. D. Qian and E. B. Lobkovsky, *Adv. Mater.*, 2007, **19**, 1693-1696.

98. B. Chen, L. Wang, F. Zapata, G. Qian and E. B. Lobkovsky, *J. Am. Chem. Soc*, 2008, **130**, 6718-6719.

99. B. L. Chen, L. B. Wang, Y. Q. Xiao, F. R. Fronczek, M. Xue, Y. J. Cui and G. D. Qian, *Angew. Chem., Int. Ed.*, 2009, **48**, 500-503.

100. A. J. Lan, K. H. Li, H. H. Wu, D. H. Olson, T. J. Emge, W. Ki, M. C. Hong and J. Li, *Angew. Chem., Int. Ed.*, 2009, **48**, 2334-2338.

101. S. Horike, M. Dinca, K. Tamaki and J. R. Long, *J. Am. Chem. Soc.*, 2008, **130**, 5854-5855.

102. K. S. Suslick, P. Bhyrappa, J. H. Chou, M. E. Kosal, S. Nakagaki, D. W. Smithenry and S. R. Wilson, *Acc. Chem. Res.*, 2005, **38**, 283-291.

103. O. K. Farha, A. M. Shultz, A. A. Sarjeant, S. T. Nguyen and J. T. Hupp, *J. Am. Chem. Soc.*, 2011, **133**, 5652-5655.

104. L. Q. Ma, C. Abney and W. B. Lin, *Chem. Soc. Rev.*, 2009, **38**, 1248-1256.

105. X. D. Zheng, M. Zhang, L. Jiang and T. B. Lu, *Dalton Trans.*, 2012, **41**, 1786-1791.

106. W. T. Liu, Y. C. Ou, Z. J. Lin and M. L. Tong, *CrystEngComm*, 2010, **12**, 3487-3489.

107. Q. Y. Liu, Y. L. Wang, N. Zhang, Y. L. Jiang, J. J. Wei and F. Luo, *Cryst. Growth Des.*, 2011, **11**, 3717-3720.

108. R. E. Morris and X. H. Bu, *Nature Chem.*, 2010, **2**, 353-361.

109. L. Q. Ma and W. B. Lin, *J. Am. Chem. Soc.*, 2008, **130**, 13834-13835.

110. L. Q. Ma, J. M. Falkowski, C. Abney and W. B. Lin, *Nature Chem.*, 2010, **2**, 838-846.

111. C. D. Wu, L. Zhang and W. B. Lin, *Inorg. Chem.*, 2006, **45**, 7278-7285.

CHAPTER 2: Design of a Metal-Organic Framework (MOF) Smart Dust for the Standoff Detection of Explosives

Introduction

The dangers associated with hidden sources of explosives and other hazardous substances can often be avoided if the analyte can be detected from a distance. TNT (2,4,6-trinitrotoluene) is one analyte of particular interest because it is a common explosive and an undesirable pollutant in soil, groundwater, and the food chain.[1] Trace amounts of TNT pose a threat to the environment and to human health; exposure can lead, *inter alia*, to hepatitis, aplastic anemia, and cancer.[2]

The detection of trace amounts of TNT is important for homeland and military security. Dogs have long been used to detect TNT, but they are expensive to train and they tire easily.[3] Traditional analytical techniques such as gas chromatography-mass spectrometry[4] and cyclic voltammetry[5] are very sensitive methods for detecting TNT, but these methods require expensive instrumentation or time-consuming procedures, thus requiring sample collection and asynchronous laboratory analysis.

One way to achieve "standoff" sensing is to use smart dusts, which generate a remotely-detectable signal when they are exposed to an analyte of interest. By distributing such a smart dust widely and exciting it remotely with a laser, the presence of suitable analytes can be detected from changes in the fluorescence. For example, Sailor and co-workers constructed smart dusts from porous silicon, whose fluorescence can be quenched by certain external chemical agents, including TNT, presumably by an electron-transfer mechanism.[6-8] Sensors based on

semiconducting organic polymers (SPOs) developed by Swager and co-workers have demonstrated ultra-trace detection of vapors of TNT and DNT (2,4-dinitrotoluene).[9-12] In these studies, however, it is not always clear whether the sensor is actually detecting TNT or DNT themselves (which have low volatilities), or whether the sensors are instead responding to small amounts of more volatile impurities that are present in these materials.

In this Chapter we report the design of a luminescent metal organic framework (MOF)[13-15] that in principle is able to serve as a smart dust for the remote detection of TNT. MOFs have large internal surface areas which are known to facilitate interactions with guest molecules.[16-19] This feature will be useful in "standoff detection" provided that the MOF pore size is large enough to admit the analyte of interest. In addition, MOFs can easily be made luminescent,[20-24] a property that is useful for molecule sensing because luminescence can easily be quenched in a chemically sensitive way.[25-27]

Recently, a few workers have investigated the use of MOFs in the detection of explosives.[28-31] Xiong et al. described a MOF able to serve as a preconcentrator for explosives, but the MOF itself was unable to serve as a sensor.[28, 29] Others have shown that the luminescent properties of MOFs can be used to detect electron-poor explosives such as 2,4-dinitrotoluene (DNT).[32] Interestingly, however, these papers specifically state that the pores in these MOFs are too small to accommodate the analytes, and that the fluorescence quenching does not involve close contacts between the luminescent centers and the analyte. As a result, the porous nature of the MOF structure is not essential to the activity of the solid.

Here we describe the first fluorescent MOF with pores that are large enough to accommodate explosive analytes. Furthermore, we show that the fluorescence is significantly

quenched only if the analyte is smaller than the MOF pores, so that detection is sensitive to both the size and electronic properties of the analyte. To achieve this goal, our MOF combines three attributes: (1) pore diameters large enough (10 Å) to accommodate TNT molecules, (2) structural elements with electron rich functional groups (bipyridine units)[28, 29, 33] that can interact with electron poor nitroaromatic molecules, and (3) fluorescent centers adjacent to the nitroaromatic "binding" sites.

Results and Discussion

The MOF we designed contains fluorescent Eu^{3+} metal centers linked into an open network by 2,2′-bipyridine-5,5′-dicarboxylate (L^{2-}) anions. The linkers play multiple roles: as structural units, as binding sites for the TNT analyte, and as antennae for the europium centers. The MOF was synthesized by means of a solvothermal reaction between $Eu(NO_3)_3 \cdot 5H_2O$ and 2,2′-bipyridine-5,5′-dicarboxylic acid in *N*,*N*-diethylformamide (DEF) at 100 ˚C as described in the experimental section. The as-prepared material was obtained as crystals (Figure 2.1) having the approximate formula $Eu_2(C_{12}N_2O_4H_6)_3(DEF)_4(H_2O)_5$. After this material was desolvated by extraction with chloroform followed by heating in vacuum at 120 ℃ for 3 h, the resulting MOF, which we will refer to as EuBPDC, has a bulk elemental analysis that corresponds to the formula $Eu_2(C_{12}N_2O_4H_6)_3(H_2O)_3$; as we will show, the remaining solvent molecules are bound to the europium centers.

The single crystal X-ray structure of the fully solvated MOF reveals the presence of a three-dimensional coordination framework with large channels that run along the *c*-axis; the channels have rhombus-shaped cross sections with dimensions of approximately 25 by 15 Å (Figure 2.2). The views along *a*- and *b*-axes, and tilted and perspective views down the *c*-axis,

are shown in Figure 2.3; the single crystal X-ray diffraction data are shown in Table 2.1, and selected bond distances and angles are listed in Table 2.2. The Eu to 2,2′-bipyridine-5,5′-dicarboxylate ratio is 2:3 as found in the microanalysis, which suggests that the linkers are fully deprotonated. There are two crystallographically independent Eu ions in the asymmetric unit, which are arranged in pairs separated by 4.188 Å. Both Eu centers are coordinated to eight oxygen atoms (all with Eu-O distances of ca. 2.4 Å), of which six on one Eu center and seven on the other are carboxylate oxygens (Figure 2.4). In addition to the coordinated carboxylate groups, three solvent molecules are coordinated per pair of Eu centers. Two of the sites on one Eu atom are water molecules (partly disordered with DEF). The third coordinating solvent molecule is a water molecule; the latter also forms a longer bond of 3.1 Å to the first Eu center.

In the fully solvated material, the channels are filled with free solvent molecules (mostly DEF) that are highly disordered. The BYPASS method in the PLATON[34] suite of programs showed that the electron density of the free solvent molecules corresponds to about 1065 electrons per unit cell. This amount, which is equivalent to approximately four DEF molecules per formula unit, is in agreement with the bulk microanalysis for the fully solvated material. In the fully solvated MOF, the two nitrogen atoms on the bipyridine backbone are probably hydrogen-bonded to solvent molecules in the channels, but these interactions are lost upon desolvation.

We can calculate from the crystallographic results that removal of the free solvent molecules should give a desolvated material in which the pore volume is 39% of the total volume. The channels within EuBPDC have diameters of about 10 Å, which is large compared to the 7 Å

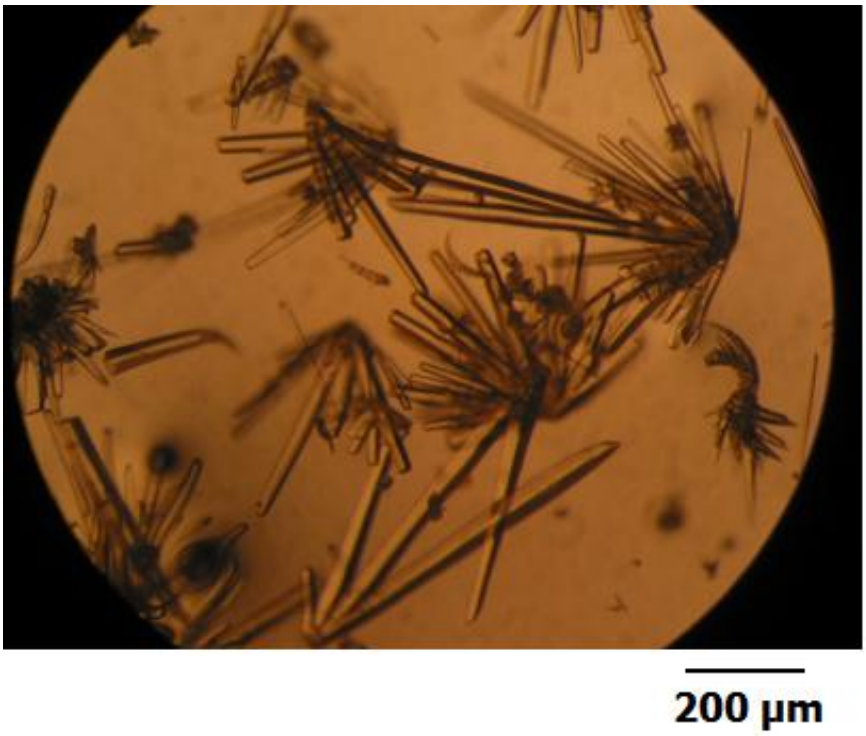

Figure 2.1. Image of as-synthesized EuBPDC.

Table 2.1. Crystal data and structure refinement for EuBPDC.

Empirical formula	$C_{40.35}H_{31.83}Eu_2N_{6.87}O_{15}$ (excluding free solvent)	
Formula weight	1156.86	
Temperature	123(3) K	
Wavelength	1.54187 Å	
Crystal system	Monoclinic	
Space group	*P* $2_1/c$	
Unit cell dimensions	a = 25.6101(18) Å	α = 90°
	b = 15.3773(3) Å	β = 98.578(7)°
	c = 16.8942(3) Å	γ = 90°
Volume	6578.8(5) $Å^3$	
Z	4	
Density (calculated)	1.168 Mg/m^3	
Absorption coefficient	13.948 mm^{-1}	
F(000)	2272.2 (excluding free solvent)	
Crystal size	0.05 x 0.04 x 0.008 mm^3	
Theta range for data collection	3.36 to 67.57°.	
Index ranges	-30<=h<=28, -18<=k<=18, -20<=l<=20	
Reflections collected	70695	
Independent reflections	11687 [R(int) = 0.1265]	
Completeness to theta = 67.57°	98.4 %	
Absorption correction	Semi-empirical from equivalents	
Max. and min. transmission	1.000 and 0.404	
Refinement method	Full-matrix least-squares on F^2	
Data / restraints / parameters	11687 / 1863 / 825	
Goodness-of-fit on F^2	0.995	
Final R indices [I>2sigma(I)]	R1 = 0.0793, wR2 = 0.2089	
R indices (all data)	R1 = 0.1073, wR2 = 0.2253	
Largest diff. peak and hole	1.725 and -1.210 $e.Å^{-3}$	

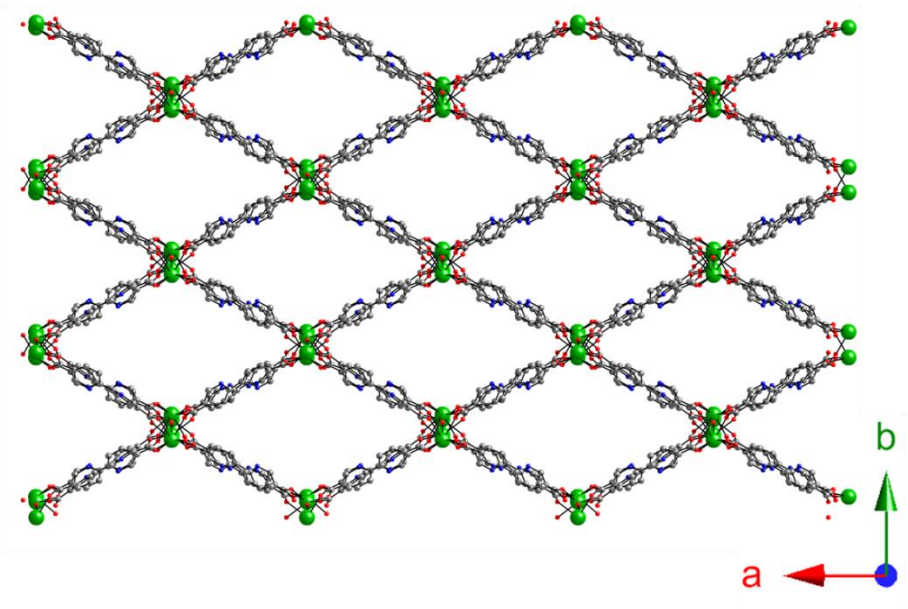

Figure 2.2. Ball-and-stick diagram of the X-ray crystal structure of EuBPDC, viewed down the c-axis. Key: grey = C; red = O; blue = N; green = Eu. The coordinated and free solvent molecules have been omitted for clarity.

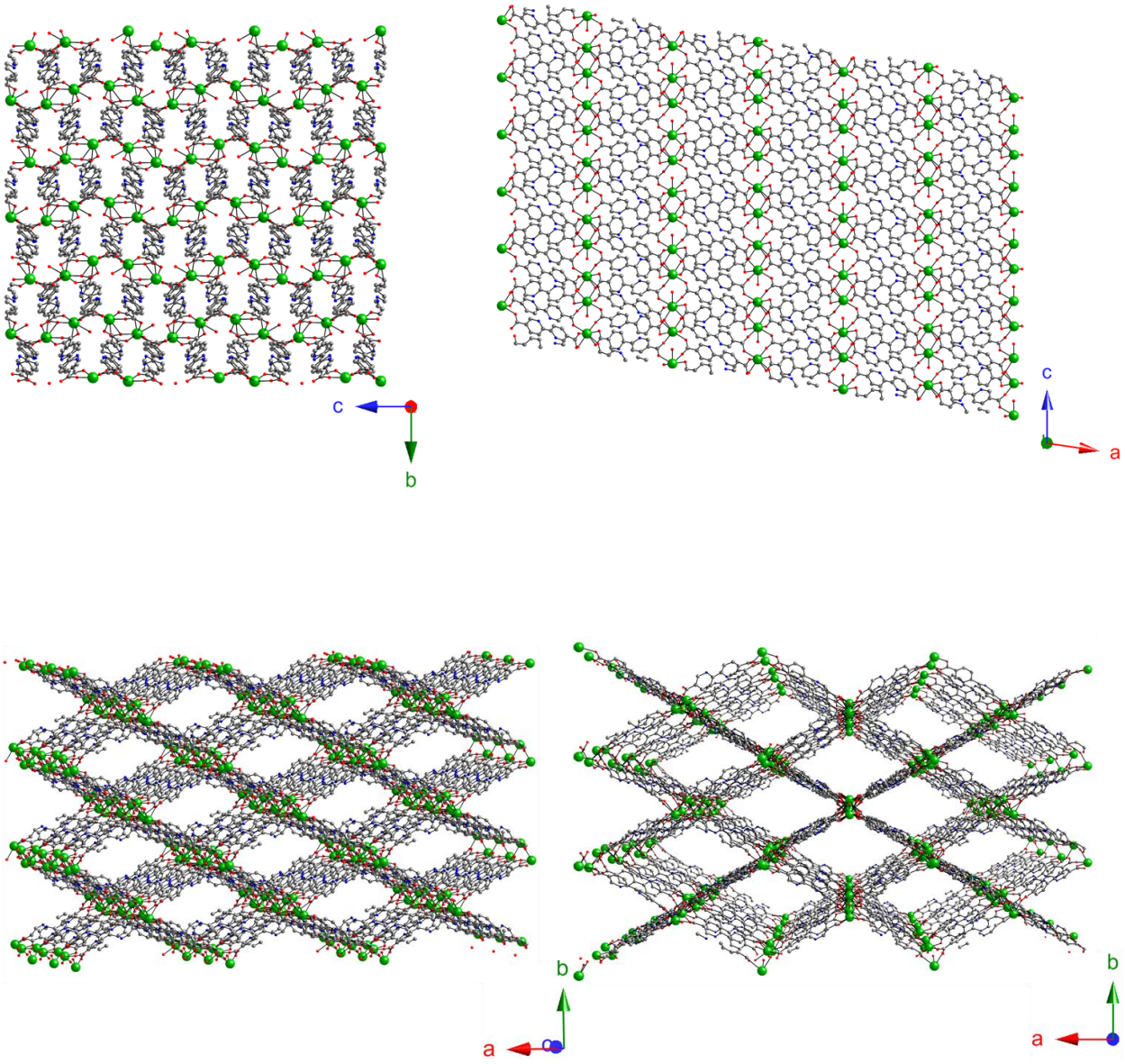

Figure 2.3. Ball-and-stick diagram of single crystal X-ray structure of EuBPDC viewed down the *a* and *b* axes, and tilted and perspective views down the *c* axis. Grey, C; Red, O; Blue, N; Green, Eu. The coordinated and free solvent molecules have been omitted for clarity.

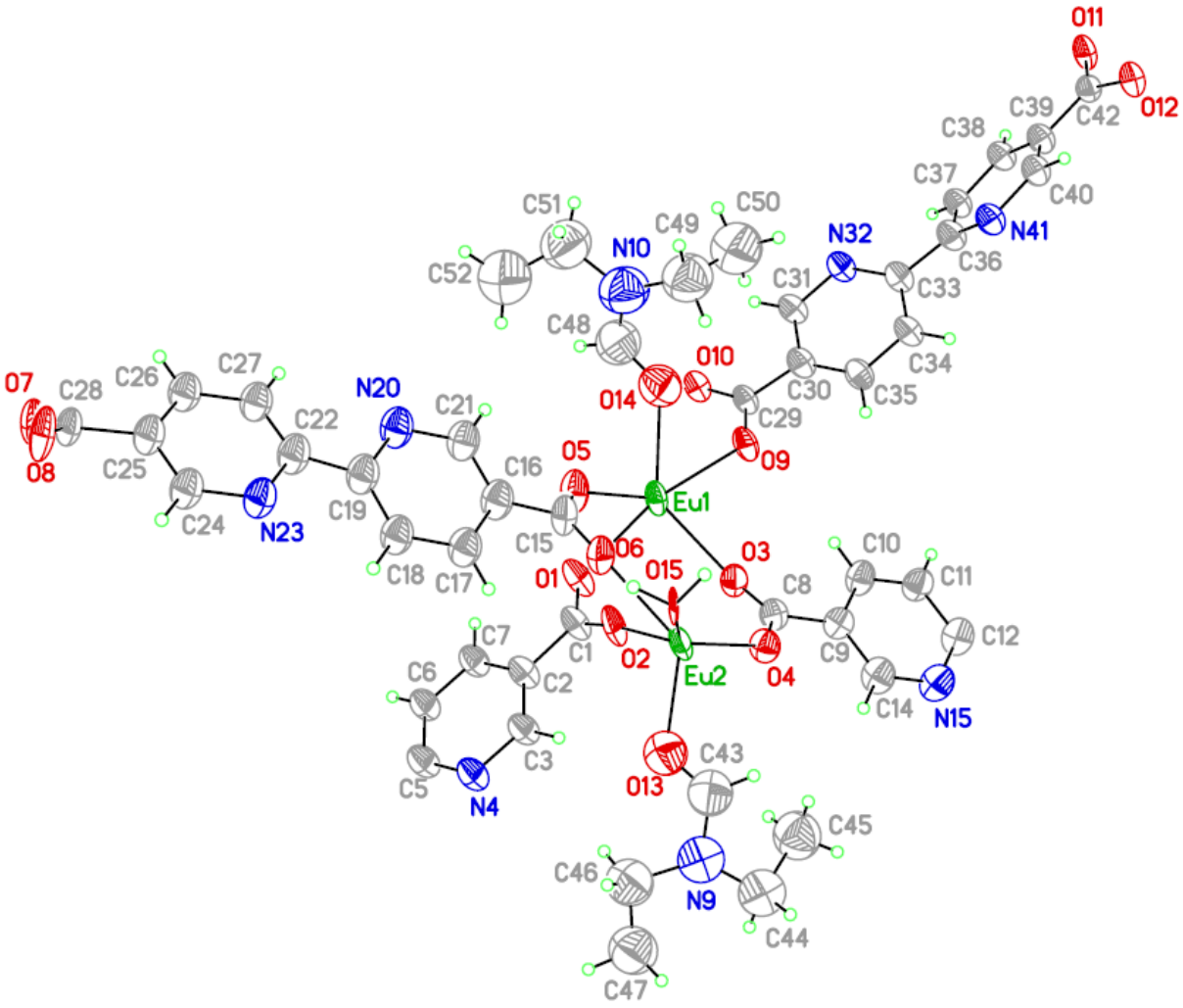

Figure 2.4. ORTEP view of the asymmetric unit of EuBPDC.

Table 2.2. Selected bond distances and angles for EuBPDC.

Bond lengths [Å]		Angles [°]		Angles [°]	
Eu(1)-O(7)#1	2.321(5)	O(7)#1-Eu(1)-O(12)#2	145.9(2)	O(1)-Eu(1)-O(14)	139.5(4)
Eu(1)-O(12)#2	2.381(5)	O(7)#1-Eu(1)-O(3)	142.00(19)	O(14B)-Eu(1)-O(14)	0.9(4)
Eu(1)-O(3)	2.388(5)	O(12)#2-Eu(1)-O(3)	72.08(17)	O(5)-Eu(1)-O(14)	72.8(4)
Eu(1)-O(9)	2.403(4)	O(7)#1-Eu(1)-O(9)	98.51(18)	O(7)#1-Eu(1)-O(2)	114.04(17)
Eu(1)-O(15)#3	2.421(6)	O(12)#2-Eu(1)-O(9)	88.33(16)	O(12)#2-Eu(1)-O(2)	74.77(15)
Eu(1)-O(1)	2.428(5)	O(3)-Eu(1)-O(9)	75.04(18)	O(3)-Eu(1)-O(2)	68.51(17)
Eu(1)-O(14B)	2.440(5)	O(7)#1-Eu(1)-O(15)#3	73.58(19)	O(9)-Eu(1)-O(2)	142.98(17)
Eu(1)-O(5)	2.448(5)	O(12)#2-Eu(1)-O(15)#3	139.07(17)	O(15)#3-Eu(1)-O(2)	101.85(18)
Eu(1)-O(14)	2.457(13)	O(3)-Eu(1)-O(15)#3	69.04(18)	O(1)-Eu(1)-O(2)	46.63(16)
Eu(1)-O(2)	2.951(5)	O(9)-Eu(1)-O(15)#3	69.92(15)	O(14B)-Eu(1)-O(2)	133.71(16)
Eu(1)-C(1)	3.068(7)	O(7)#1-Eu(1)-O(1)	74.4(2)	O(5)-Eu(1)-O(2)	64.64(18)
Eu(2)-O(13)	2.314(18)	O(12)#2-Eu(1)-O(1)	121.39(18)	O(14)-Eu(1)-O(2)	133.7(4)
Eu(2)-O(10)#4	2.325(5)	O(3)-Eu(1)-O(1)	85.27(19)	O(7)#1-Eu(1)-C(1)	93.5(2)
Eu(2)-O(2)	2.338(5)	O(9)-Eu(1)-O(1)	137.24(17)	O(12)#2-Eu(1)-C(1)	98.26(19)
Eu(2)-O(8)#5	2.390(5)	O(15)#3-Eu(1)-O(1)	67.64(17)	O(3)-Eu(1)-C(1)	77.1(2)
Eu(2)-O(6)	2.407(5)	O(7)#1-Eu(1)-O(14B)	73.6(2)	O(9)-Eu(1)-C(1)	147.7(2)
Eu(2)-O(4)	2.410(5)	O(12)#2-Eu(1)-O(14B)	77.35(15)	O(15)#3-Eu(1)-C(1)	85.19(19)
Eu(2)-O(11)#2	2.457(5)	O(3)-Eu(1)-O(14B)	134.2(2)	O(1)-Eu(1)-C(1)	23.14(19)
Eu(2)-O(13B)	2.468(3)	O(9)-Eu(1)-O(14B)	70.7(2)	O(14B)-Eu(1)-C(1)	141.5(2)
Eu(2)-O(12)#2	2.897(5)	O(15)#3-Eu(1)-O(14B)	123.20(17)	O(5)-Eu(1)-C(1)	68.8(2)
Eu(2)-C(42)#2	3.063(7)	O(1)-Eu(1)-O(14B)	140.3(2)	O(14)-Eu(1)-C(1)	141.0(4)
Eu(2)-O(15)	3.086(7)	O(7)#1-Eu(1)-O(5)	78.93(17)	O(2)-Eu(1)-C(1)	23.55(16)
Eu(2)-C(43)	3.185(14)	O(12)#2-Eu(1)-O(5)	75.82(16)	O(7)#1-Eu(1)-Eu(2)	139.10(13)
O(1)-C(1)	1.268(9)	O(3)-Eu(1)-O(5)	128.36(18)	O(12)#2-Eu(1)-Eu(2)	42.01(12)
O(2)-C(1)	1.233(9)	O(9)-Eu(1)-O(5)	142.95(19)	O(3)-Eu(1)-Eu(2)	63.76(12)
C(1)-C(2)	1.491(8)	O(15)#3-Eu(1)-O(5)	140.61(15)	O(9)-Eu(1)-Eu(2)	121.86(12)
C(1)-C(2B)	1.491(8)	O(1)-Eu(1)-O(5)	78.23(19)	O(15)#3-Eu(1)-Eu(2)	123.70(15)
C(2)-C(3)	1.3900	O(14B)-Eu(1)-O(5)	73.2(2)	O(1)-Eu(1)-Eu(2)	79.40(13)
C(2)-C(7)	1.3900	O(7)#1-Eu(1)-O(14)	72.8(4)	O(14B)-Eu(1)-Eu(2)	111.51(6)
C(3)-N(4)	1.3900	O(12)#2-Eu(1)-O(14)	78.1(3)	O(5)-Eu(1)-Eu(2)	65.22(13)
N(4)-C(5)	1.3900	O(3)-Eu(1)-O(14)	135.1(3)	O(14)-Eu(1)-Eu(2)	111.9(3)

Symmetry transformations used to generate equivalent atoms: #1 -x+2,-y,-z+2 #2 -x+3,-y,-z+2 #3 x,-y-1/2,z-1/2 #4 x,-y-1/2,z+1/2 #5 -x+2,y-1/2,-z+5/2 #6 -x+2,-y-1,-z+2 #7 -x+3,-y-1,-z+2 #8 -x+2,y+1/2,-z+5/2

size of a TNT molecule (calculated from the van der Waals surfaces). As a result, EuBPDC has pores that are large enough to enable TNT molecules to diffuse into the framework. Furthermore, the bipyridine nitrogen atoms are accessible to molecules occupying the framework channels.

The surface area of desolvated EuPPDC is 630 $m^2 \cdot g^{-1}$, as judged from a BET adsorption isotherm using N_2 as the working gas, which confirms the presence of permanent porosity. The simulated X-ray powder diffraction pattern derived from the single crystal X-ray data matches well with the pattern obtained from as-synthesized EuBPDC (Figure 2.5). The framework of EuBPDC is reasonably thermally stable. TGA studies show that the desolvated material undergoes no phase change up to 510 ˚C; only above this temperature does the framework begin to decompose (Figure 2.6).

We examined the adsorption of TNT and other vapors in the MOF by using the procedures described by Luebbers et al.[35, 36] Pulses of the various analytes were passed through a short column of the solid MOF and the breakthrough volume was recorded. Methanol, pentane, ethyl acetate, tetrahydrofuran, toluene, acetone, ethanol, and acetonitrile passed essentially freely through EuBPDC. At 40 ˚C, the breakthrough gas volumes were 0.06 L/(gm of MOF) or less in all cases.

In contrast, EuBPDC shows an affinity for TNT. When TNT sample carried by helium passed through EuBPDC and the temperature is ramped to 200 ˚C, no elution of TNT occurs over 2 h. By comparison, at 150 ˚C, TNT elutes in about 5 min from a 1 meter OV5 column under similar elution conditions (Figure 2.7). This result shows that EuBPDC is able to bind TNT, as expected from the calculations of Xiong et al.[28, 29]

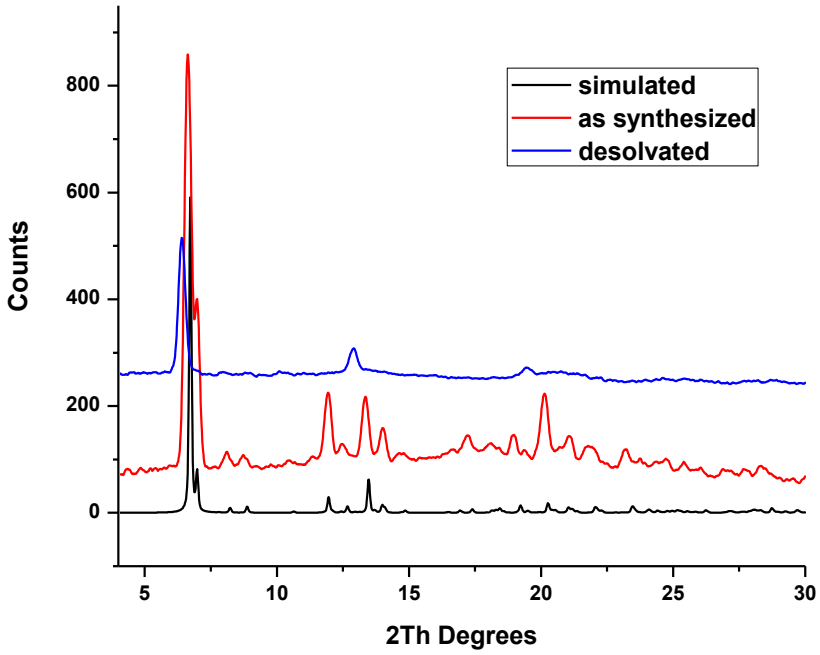

Figure 2.5. Simulated powder XRD pattern from the single crystal data (black), and patterns obtained from as-synthesized EuBPDC (red) and desolvated EuBPDC (blue). The simulated and as-synthesized EuBPDC patterns match very well. After the removal of guest molecules, EuBPDC loses some crystallinity.

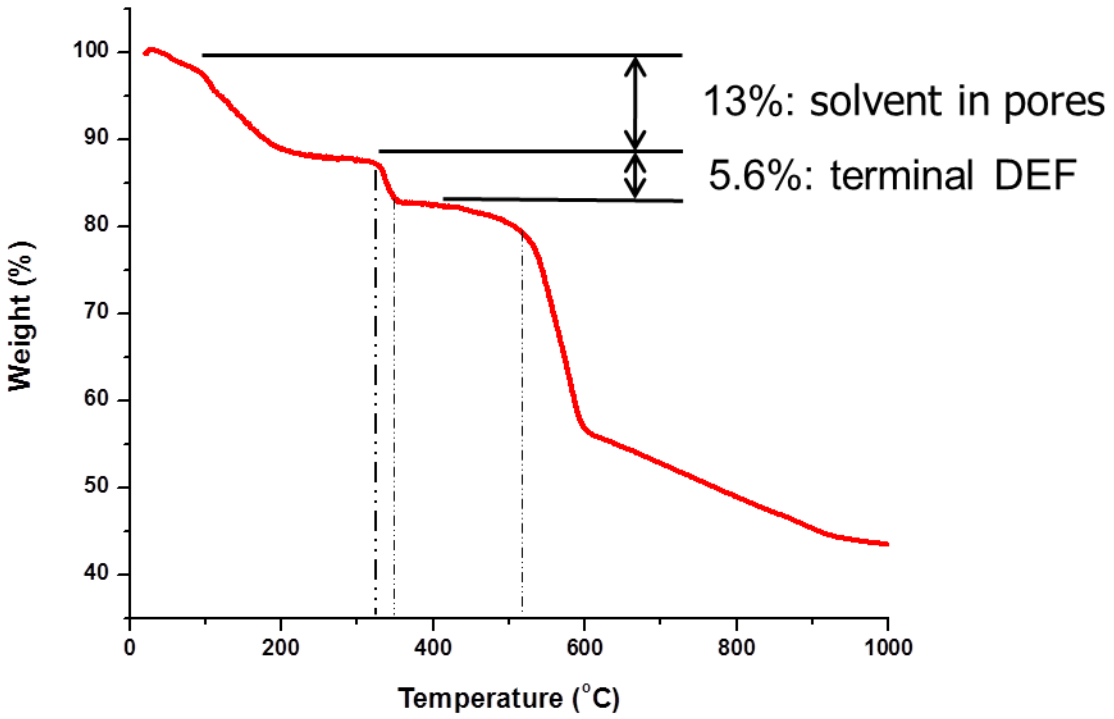

Figure 2.6. TGA data indicate that EuBPDC releases the free and terminal water and DEF molecules in the temperature range of 20-350 ˚C, to form a guest-free phase, which is thermally stable up to 510 ˚C.

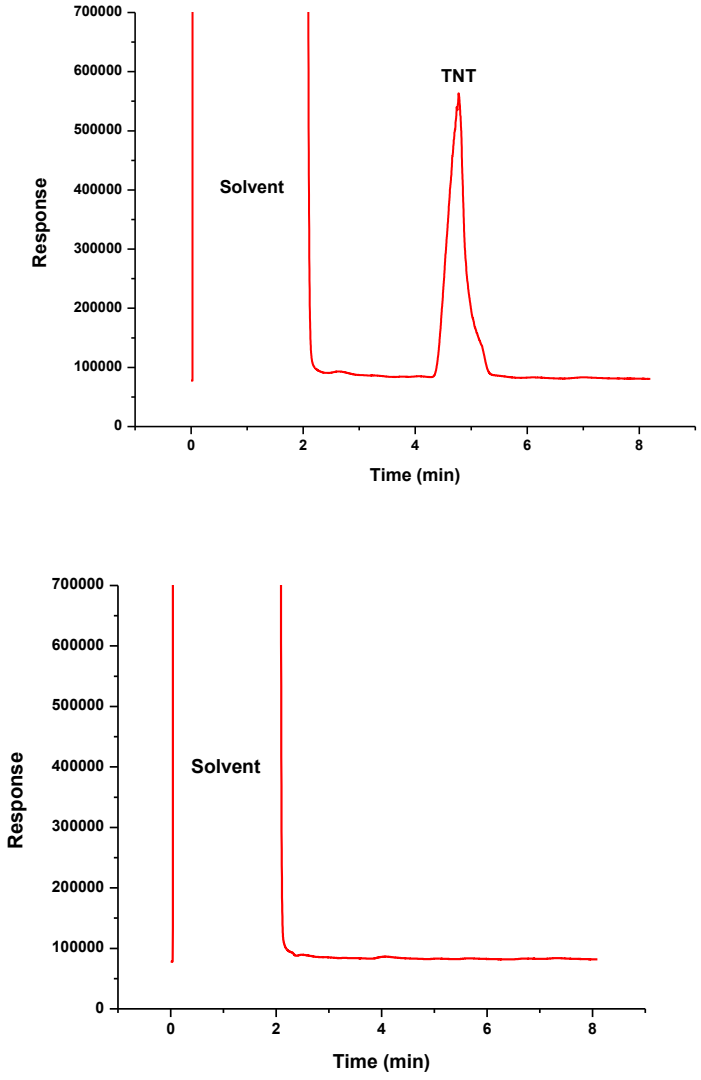

Figure 2.7. (upper) Breakthrough data in which the outlet of the OV5 column was connected to an empty guard column. (lower) Breakthrough data in which the outlet of the OV5 column was connected to a guard column filled with EuBPDC.

Most europium salts exhibit weak fluorescence in the visible region of the EM spectrum because the f-f transitions are forbidden by the Laporte selection rules.[37, 38] In contrast, EuBPDC emits strongly in the red under UV irradiation at 360 nm at room temperature (Figure 2.8). The emission peaks at 579, 591, 610, 651, and 700 nm can be ascribed to the characteristic $^5D_0 \rightarrow {}^7F_0$, $^5D_0 \rightarrow {}^7F_1$, $^5D_0 \rightarrow {}^7F_2$, $^5D_0 \rightarrow {}^7F_3$, and $^5D_0 \rightarrow {}^7F_4$ transitions of the Eu^{3+} ion, respectively. The strong fluorescence is due to an antenna effect[39] in which vibronic coupling leads to efficient energy transfer between the triplet state of the strongly absorbing bipyridine linkers and the emissive state of the Eu^{3+} ion. Because Eu^{3+} binds to the carboxylate oxygen atoms and not to the bipyridine nitrogen atoms, the latter are available to interact with analytes. Specifically, bipyridines – which are relatively electron rich – are known to interact strongly with electron poor aromatic compounds such as TNT.[40, 41] Furthermore, because such interactions are known interfere with the ability of the bipyridines to engage in energy transfer to the europium centers, significant fluorescent quenching of EuBPDC should occur in the presence of TNT.

When EuBPDC is exposed to a series of 0.01 mL aliquots of a 200 ppm solution of TNT in CH_3OH/CH_3CN (v/v = 1/1), the fluorescence intensity decreases monotonically upon the successive addition of each aliquot (Figure 2.9a). After 3 drops, 58 % of the fluorescence had been quenched, as judged from the intensity of the peak at 610 nm. Control experiments obtained by exposing EuBPDC to just the 1:1 CH_3OH/CH_3CN solvent mixture (no analyte) showed essentially no effect on the fluorescence intensity. Additional control experiments employing other common solvents and small molecules (including non-nitrated aromatic molecules such as toluene) showed that the fluorescence of EuBPDC is at best only slightly affected (Figure 2.10). TNT absorbs only weakly at the irradiation wavelength of 360 nm, which militates against the

possibility that the reduced fluorescence in the presence of TNT is simply due to reduced irradiation flux.[42, 43]

In order to determine whether fluorescence quenching requires movement of the TNT molecules through the porous MOF structure, we investigated whether the quenching efficiency depends on the size of the nitroaromatic molecule. We find that 4-tert-butyl-2,6-dinitroanisole, which can also pass through the pores (Figure 2.9b) causes quenching, whereas 1,1-diphenyl-2-picrylhydrazine, which cannot pass through the pores (Figure 2.9c), does not cause quenching. This result provides evidence that the fluorescence quenching is size-dependent, and that the mechanism for quenching involves movement of the analyte through the MOF framework.

In summary, EuBPDC is an easily synthesized MOF which is highly porous, thermally stable, and strongly fluorescent. The fluorescence is strongly quenched in the presence of TNT by a mechanism in which TNT molecules diffuse through the MOF channels, interact with the bipyridine units on the channel walls, and weaken the vibronic coupling between ligands and the Eu^{3+} centers. Owing to the limited volatilities of TNT and similar analytes, however, use of MOFs as "smart dusts" for standoff detection in the field will require more sensitive detection protocols that, for example, involve signal amplification. This goal remains an important challenge for the future.

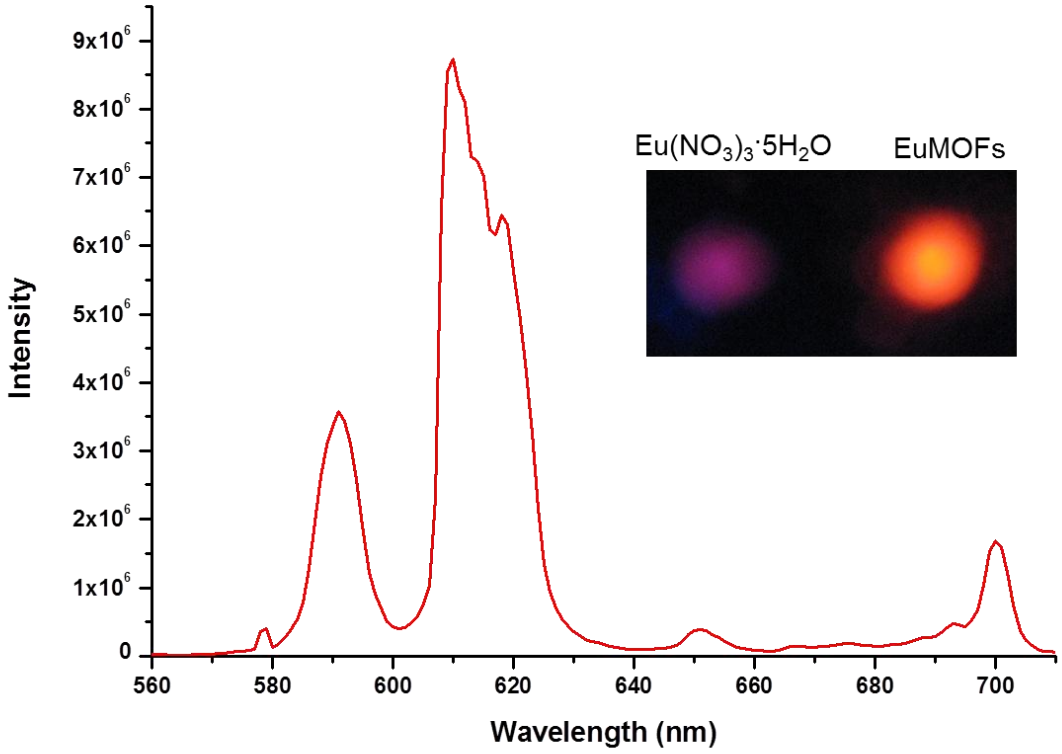

Figure 2.8. Fluorescence spectrum of EuBPDC.

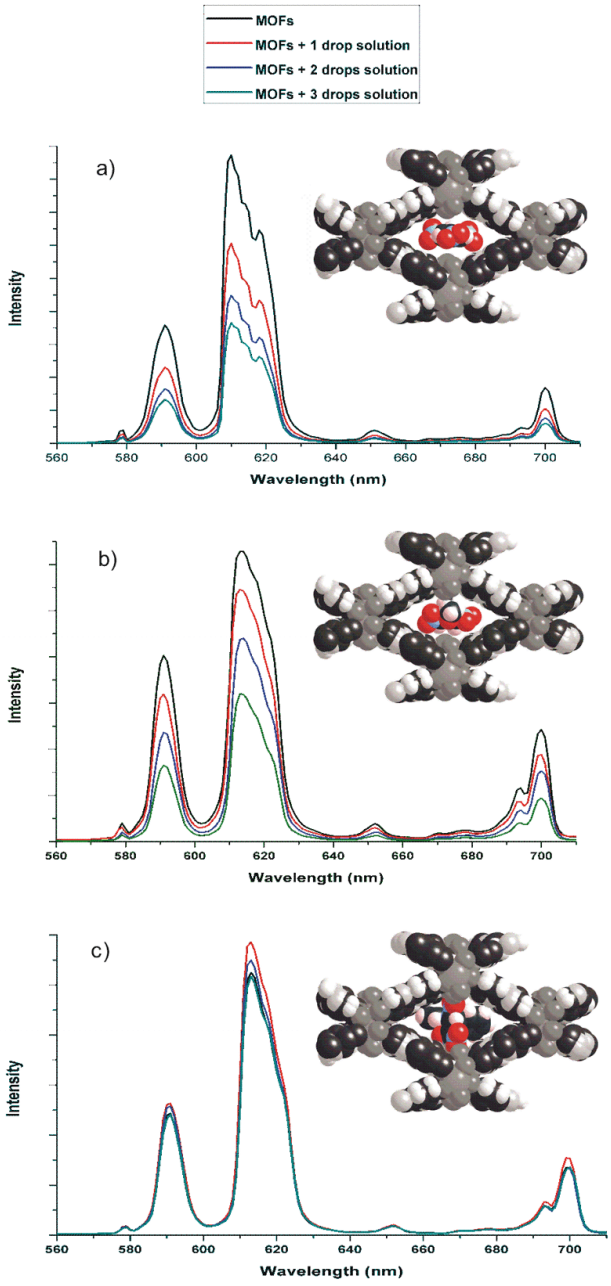

Figure 2.9. Fluorescence quenching of EuBPDC as a function of the size of the nitroaromatic molecule. Fluorescence spectra taken after 0, 1, 2, and 3 drops (0.01 mL each) of a solution of the analyte. The inset shows a spacing filling view of one nitroaromatic molecule fitted as well as possible into the MOF pore. a) 200 ppm TNT in CH_3OH/CH_3CN (v/v = 1/1). b) 110 ppm 4-tert-butyl-2,6-dinitroanisole in CH_3OH (saturated solution). c) 200 ppm 1,1-diphenyl-2-picrylhydrazine in CH_3OH.

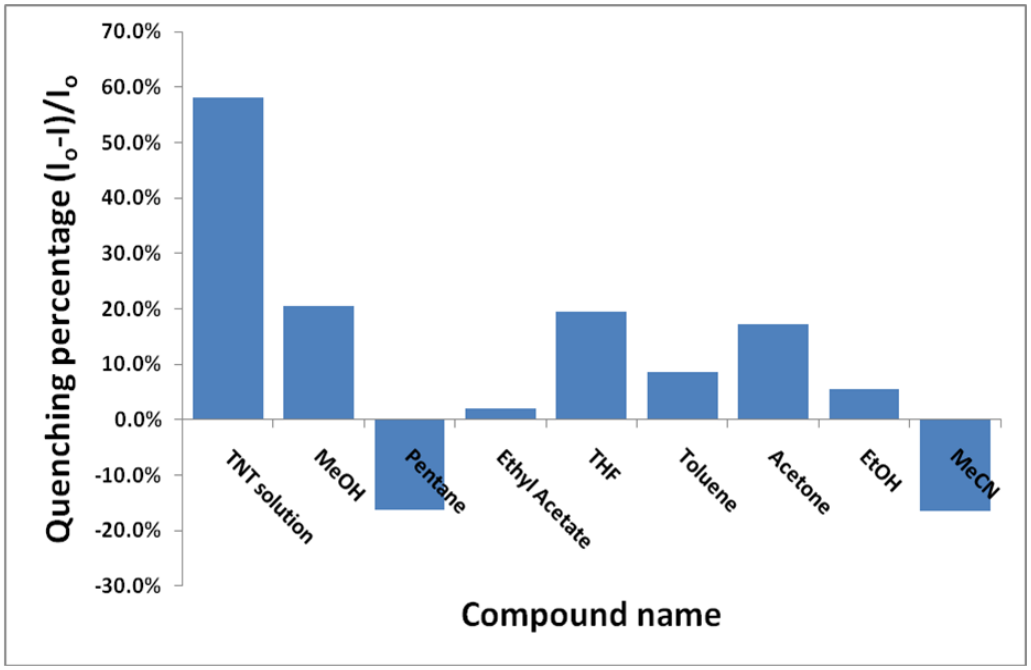

Figure 2.10. Comparison of quenching percentage when EuBPDC is dosed with 0.03 mL of a 1 mg/mL solution of TNT vs. 0.03 mL of a number of pure solvents.

Experimental Section

Synthesis of $Eu_2(C_{12}N_2O_4H_6)_3(H_2O)_3$ (EuBPDC). The chemicals were obtained from Aldrich and used as received. The synthesis was performed under solvothermal conditions. $Eu(NO_3)_3{\cdot}5H_2O$ (0.017 g, 0.04 mmol), and 2,2'-bipyridine-5,5'-dicarboxylic acid (0.015 g, 0.06 mmol) were mixed and dispersed in DEF (5 mL). The resulting white slurry was then put in oven and heated to 100 ℃ for three days to afford light-yellow needle crystals, which were isolated to obtain the "as prepared material." Desolvation to EuBPDC was achieved by immersing the as-prepared crystals in chloroform (5 mL) for three days, with the solvent being changed once daily. The solid was then collected by filtration and dried in a vacuum oven at 120 ℃ for 3 h.

Elemental microanalysis. Elemental analyses were carried out by the University of Illinois Microanalytical Laboratory. Anal. for the as-prepared material: Calcd for $Eu_2(C_{12}N_2O_4H_6)_3(H_2O)_5(DEF)_4$: C, 44.10; H, 4.76; N, 9.18. Found: C, 43.89; H, 4.73; N, 9.21. Anal. for the desolvated material: Calcd for $Eu_2(C_{12}N_2O_4H_6)_3(H_2O)_3$: C, 39.87; H, 2.23; N, 7.75. Found: C, 38.42; H, 2.02; N, 7.48.

Brunauer - Emmett - Teller (BET) measurements. BET measurements were performed on QuantachromeNova 2200e using nitrogen as the working gas.

Powder X-ray diffraction. Powder XRD data were collected on a Bruker General Area Detector Diffraction System (GADDS) equipped with a P4 four-circle diffractometer and HiStar multiwire area detector. A Bruker M18XHF22 rotating anode generator operating at 50kV and 40mA supplied the Cu Kα graphite monochromatized incident beam. The simulated pattern

derived from single X-ray data matches well with the pattern obtained from as-synthesized EuBPDC.

Thermogravimetric analysis (TGA). TGA was performed on Cahn Thermax 500 Thermogravimetric Analyzer.

Fluorescence study of EuBPDC. Fluorescence spectra were obtained on a Jobin Yvon Horiba FluoroMax-3 Spectrofluorometer. The excitation wavelength was 360 nm. During every test, a thin layer of ~1 mg of EuBPDC was placed between two glass slides. The TNT solution and all other solvent or small molecules were dropped onto EuBPDC by a syringe.

Adsorption behavior. Breakthrough volumes were determined by inverse-gas chromatography (IGC) studies. A plug made of IP (intermediate polarity) deactivated borosilicate glass wool about 1 cm long was inserted into one end of an approximately 7 cm long 0.53 mm ID guard column. The mass of the capillary and glass wool plug was measured and recorded. The column was connected to a vacuum pump and a vacuum of around 10 psi was applied using a metering valve for control. Approximately ~2 mg of dry EuBPDC powder was suctioned into the open end of the column with occasional mechanical vibrations used to assist the uniform packing. This amount of MOF fills about 3-4 cm of the column when packed. After reweighing the column (now with MOF), a second glass wool plug was inserted into the open end of the column. Excess guard column was trimmed from the packed bed to reduce dead volume and peak broadening, leaving around 1 cm open on each end. The final weight of the shortened column was recorded. The guard column packed with EuBPDC was then connected to two lengths (7 and 30 cm) of 0.25 mm ID guard using butt connector with M-2B butt connector ferrules. The column assembly was then connected into the split/splitless inlet of an Agilent 6890

gas chromatograph using the shorter length of connecting guard column (oriented in such a way that the direction of flow is the same as that of the suction during the packing process) with the longer length of connecting column left open during the duration of activation. The gas chromatograph was set up using UHP helium as a carrier gas, which was first passed through a 7 μm particle filter and then through a universal trap (Agilent, RMSH 2). A split/splitless fast focus inlet linear with 2.3 mm ID was used in the gas chromatograph inlet. For activation, the inlet of the gas chromatograph was pressurized to 20 psi and the oven temperature was slowly ramped (1 ˚C/min) to 200 ˚C, at which point the temperature was held for 10 h before the column was slowly returned to room temperature. This step was done to remove any residual guest molecules in the EuBPDC and to increase the available porosity for IGC measurements. The packed column was then disassembled and reweighed to account for any mass changes due to removal of residual solvent in the EuBPDC. The packed column was then reassembled, a 1 meter OV5 column was placed on the inlet to the column, the effluent at the end of the column was connected to a flow meter (Omega, FMA-A2300), and the flow rates were recorded for all combinations of temperature and pressure investigated. The flow meter readings were converted to values appropriate for helium by multiplication by a conversion factor. After the flow rates for each set of temperature and pressure were measured and recorded, the outlet of the column was connected to a flame ionization detector (FID), and the inlet and pulse injections were performed. At the start of the experiment, 0.2 mL of analyte (200 ppm TNT in 1:1 CH3OH/CH3CN) was injected using an auto injector (Agilent, 7683B) equipped with a 10 mL gastight syringe (Agilent, 5181-3354).

X-ray single crystal diffraction (performed by Dr. Danielle Gray). Single-crystal X-ray diffraction data were collected with the use of monochromatized Cu Kα radiation (λ =

1.54186 Å) at 150 K on a Rigaku Saturn944+ CCD diffractometer.[44] Combinations of nine 0.5° φ and ω scans were used to collect the data. The collection, cell refinement, integration of intensity data, and absorption correction were carried out with the CrystalClear-SM Expert suite of software.[45] The structure was solved using direct methods, SHELXS,[46] and refined with the full-matrix least-squares SHELXL program. The asymmetric unit of the framework consists of two Eu^{3+} ions, three [$^{-}OOC(C_5NH_3)_2COO^{-}$] ligands, and three coordinated solvent sites. Two of the coordinated solvent molecules bond to a single Eu atom through the O atom. These two sites are disordered between diethylformamide (DEF) and water. The third solvent site is a bridging water molecule bonded to two Eu atoms. The location of the remaining guest molecules were poorly defined so their contributions were removed from the diffraction data using the SQUEEZE bypass procedure in PLATON.[47] Additional restraints were added to aid in modeling the framework and coordinated ligands as described in the Supplemental Information. For all $(C_{12}H_6N_2O_4)^{2-}$ ligands, the N atoms were arbitrarily assigned owing to the unreliable bond lengths because of positional disorder. The N atoms could either be cis or trans with each other within the individual ligands. CCDC 797192 contains supplementary crystallographic data for this paper. These data can be obtained free of charge from The Cambridge Crystallographic Data Centre via www.ccdc.cam.ac.uk/data_request/cif.

References

1. M. G. Ryon and R. H. Ross, *Regul. Toxicol. Pharmacol.*, 1990, **11**, 104-113.
2. G. P. Anderson, S. C. Moreira, P. T. Charles, I. L. Medintz, E. R. Goldman, M. Zeinali and C. R. Taitt, *Anal. Chem.*, 2006, **78**, 2279-2285.

3. A. W. Czarnik, *Nature*, 1998, **394**, 417-418.

4. J. A. Laramee and M. L. Deinzer, *Anal. Chem.*, 1994, **66**, 719-724.

5. M. Krausa and K. Schorb, *J. Electroanal. Chem.*, 1999, **461**, 10-13.

6. S. Content, W. C. Trogler and M. J. Sailor, *Chem.--Eur. J.*, 2000, **6**, 2205-2213.

7. J. R. Link and M. J. Sailor, *Proc. Natl. Acad. Sci. U. S. A.*, 2003, **100**, 10607-10610.

8. T. A. Schmedake, F. Cunin, J. R. Link and M. J. Sailor, *Adv. Mater. (Weinheim, Ger.)*, 2002, **14**, 1270-1272.

9. A. Rose, Z. G. Zhu, C. F. Madigan, T. M. Swager and V. Bulovic, *Nature*, 2005, **434**, 876-879.

10. C. J. Cumming, C. Aker, M. Fisher, M. Fox, M. J. la Grone, D. Reust, M. G. Rockley, T. M. Swager, E. Towers and V. Williams, *IEEE Trans. Geosci. Remote Sens.*, 2001, **39**, 1119-1128.

11. T. Naddo, X. M. Yang, J. S. Moore and L. Zang, *Sens. Actuators, B*, 2008, **134**, 287-291.

12. T. Naddo, Y. K. Che, W. Zhang, K. Balakrishnan, X. M. Yang, M. Yen, J. C. Zhao, J. S. Moore and L. Zang, *J. Am. Chem. Soc.*, 2007, **129**, 6978-6979.

13. M. Eddaoudi, J. Kim, N. Rosi, D. Vodak, J. Wachter, M. O'Keeffe and O. M. Yaghi, *Science*, 2002, **295**, 469-472.

14. N. L. Rosi, J. Eckert, M. Eddaoudi, D. T. Vodak, J. Kim, M. O'Keeffe and O. M. Yaghi, *Science*, 2003, **300**, 1127-1129.

15. U. Mueller, M. Schubert, F. Teich, H. Puetter, K. Schierle-Arndt and J. Pastre, *J. Mater. Chem.*, 2006, **16**, 626-636.

16. A. R. Millward and O. M. Yaghi, *J. Am. Chem. Soc.*, 2005, **127**, 17998-17999.

17. C. Prestipino, L. Regli, J. G. Vitillo, F. Bonino, A. Damin, C. Lamberti, A. Zecchina, P. L. Solari, K. O. Kongshaug and S. Bordiga, *Chem. Mater.*, 2006, **18**, 1337-1346.

18. H. Furukawa, N. Ko, Y. B. Go, N. Aratani, S. B. Choi, E. Choi, A. O. Yazaydin, R. Q. Snurr, M. O'Keeffe, J. Kim and O. M. Yaghi, *Science*, 2010, **329**, 424-428.

19. M. Hirscher, *Angew. Chem., Int. Ed.*, 2011, **50**, 581-582.

20. M. Fuentes-Cabrera, D. M. Nicholson, B. G. Sumpter and M. Widom, *J. Chem. Phys.*, 2005, **123**, 124713-124719.

21. Q. R. Fang, G. S. Zhu, M. Xue, J. Y. Sun, F. X. Sun and S. L. Qiu, *Inorg. Chem.*, 2006, **45**, 3582-3587.

22. Z. D. Lu, L. L. Wen, Z. P. Ni, Y. Z. Li, H. Z. Zhu and Q. J. Meng, *Cryst. Growth Des.*, 2007, **7**, 268-274.

23. C. Serre, F. Millange, C. Thouvenot, N. Gardant, F. Pelle and G. Ferey, *J. Mater. Chem.*, 2004, **14**, 1540-1543.

24. D. T. de Lill, N. S. Gunning and C. L. Cahill, *Inorg. Chem.*, 2005, **44**, 258-266.

25. M. D. Allendorf, C. A. Bauer, R. K. Bhakta and R. J. T. Houk, *Chem. Soc. Rev.*, 2009, **38**, 1330-1352.

26. L. E. Kreno, K. Leong, O. K. Farha, M. Allendorf, R. P. Van Duyne and J. T. Hupp, *Chem. Rev.*, 2012, **112**, 1105-1125.

27. Y. J. Cui, Y. F. Yue, G. D. Qian and B. L. Chen, *Chem. Rev.*, 2012, **112**, 1126-1162.

28. R. Xiong, D. J. Keffer, M. Fuentes-Cabrera, D. M. Nicholson, A. Michalkova, T. Petrova, J. Leszczynski, K. Odbadrakh, B. L. Doss and J. P. Lewis, *Langmuir*, 2010, **26**, 5942-5950.

29. R. Xiong, K. Odbadrakh, A. Michalkova, J. P. Luna, T. Petrova, D. J. Keffer, D. M. Nicholson, M. A. Fuentes-Cabrera, J. P. Lewis and J. Leszczynski, *Sens. Actuators, B*, 2010, **B148**, 459-468.

30. H. Xu, F. Liu, Y. Cui, B. Chen and G. Qian, *Chem. Commun. (Cambridge, U. K.)*, 2011, **47**, 3153-3155.

31. F. P. Doty, C. A. Bauer, A. J. Skulan, P. G. Grant and M. D. Allendorf, *Adv. Mater.*, 2009, **21**, 95-101.

32. A. J. Lan, K. H. Li, H. H. Wu, D. H. Olson, T. J. Emge, W. Ki, M. C. Hong and J. Li, *Angew. Chem., Int. Ed.*, 2009, **48**, 2334-2338.

33. B. Chen, L. Wang, Y. Xiao, F. R. Fronczek, M. Xue, Y. Cui and G. Qian, *Angew. Chem., Int. Ed.*, 2009, **48**, 500-503.

34. A. L. Spek, *J. Appl. Crystallogr.*, 2003, **36**, 7-13.

35. M. T. Luebbers, T. Wu, L. Shen and R. I. Masel, *Langmuir*, 2010, **26**, 11319-11329.

36. M. T. Luebbers, T. Wu, L. Shen and R. I. Masel, *Langmuir*, 2010, **26**, 15625-15633.

37. K. A. White, D. A. Chengelis, K. A. Gogick, J. Stehman, N. L. Rosi and S. Petoud, *J. Am. Chem. Soc.*, 2009, **131**, 18069-18071.

38. M. D. Allendorf, C. A. Bauer, R. Bhakta and R. Houk, *Chem. Soc. Rev.*, 2009, **38**, 1330-1352.

39. N. Sabbatini, M. Guardigli and J. M. Lehn, *Coord. Chem. Rev.*, 1993, **123**, 201-228.

40. K. C. Szeto, K. O. Kongshaug, S. Jakobsen, M. Tilset and K. P. Lillerud, *Dalton Trans.*, 2008, 2054-2060.

41. K. C. Szeto, K. P. Lillerud, M. Tilset, M. Bjorgen, C. Prestipino, A. Zecchina, C. Lamberti and S. Bordiga, *J. Phys. Chem. B*, 2006, **110**, 21509-21520.

42. T. Abe, *Bull. Chem. Soc. Jpn.*, 1958, **31**, 904-907.

43. T. Abe, *Bull. Chem. Soc. Jpn.*, 1959, **32**, 339-344.

44. Rigaku (2010). Saturn944+. Rigaku Americas Corporation, The Woodlands, Texas, USA

45. Rigaku (2010). CrystalClear-SM Expert 2.0 r5. Rigaku Americas Corporation, The Woodlands, Texas, USA.

46. Sheldrick, G. M. SHELXS-97, 97-2; University of Göttingen, Germany: 1997.

47. P. Vandersluis and A. L. Spek, *Acta Crystallogr A*, 1990, **46**, 194-201.

CHAPTER 3: Synthesis and Characterization of a Zinc Metal-Organic Framework with Chiral Nano-Pores

Introduction

Metal-organic frameworks (MOFs), inorganic-organic hybrid crystalline solids with large internal surface areas,[1, 2] and easily tunable structures, pores sizes, and surface functionalities.[3, 4] They are being investigated as potential materials for a variety of applications including gas storage,[5-9] gas separation,[10-14] catalysis,[15-18] sensing,[19-22] and drug delivery.[23-26] MOF syntheses usually take place under relatively mild conditions, which allows direct incorporation of even delicate functional groups into the framework.

Chiral MOFs are of interest due to their potential applications as heterogeneous asymmetric catalysts and as stationary phases for enantioselective separations.[27] Most chiral MOFs are prepared with the use of readily available chiral organic linkers.[28] For example, Lin and co-workers[29-31] have successfully synthesized a variety of homochiral MOFs using enantiopure binaphthyl-derived ligands, such as 1,1′ -binaphthalene-2,2′ -diol (BINOL) and 2,2′ -bis(diphenylphosphino)-1,1′ -binaphthyl (BINAP). Homochiral MOFs have also been obtained from achiral components via self-resolution during crystal growth.[32-35] Aoyama *et al.* synthesized a homochiral MOF $Cd(apd)(NO_3)_2 \cdot H_2O \cdot EtOH$ from achiral 5-(9-anthracenyl)pyrimidine (*apd*) and Cd^{2+} by using enantiopure seed crystals.[36] Bu and coworkers developed a method for homochiral crystallization of MOFs through the use of chiral catalysts: five different MOFs were obtained using different combination of reactants, solvents, and catalysts.[37] Morris and coworkers prepared chiral MOFs by employing a chiral solvent: an ionic liquid containing L-aspartate.[38]

Here we report the synthesis of a new MOF with chiral nano-pores by spontaneous resolution from achiral components. This MOF shows permanent porosity: removal of the solvent does not result in collapse of the chiral nano-pores.

Results and Discussion

A mixture of $Zn(NO_3)_2 \cdot 6H_2O$, formic acid, and 2,2′-bipyridine-5,5′-dicarboxylic acid in DEF (DEF = *N*,*N*′-diethylformamide) was heated at 100 ˚C for 3 weeks to give light yellow crystals formulated as $Zn_3(BPDC)_2(O_2CH)_2$•2DEF (**1**•2DEF) (Figure 3.1). A BPDC/formic acid ratio of ca. 1.0 is critical to the formation of **1**•2DEF. A few other MOFs containing formate ligands are known, but most of these groups were claimed to have been generated by decomposition of a formamide solvent.[39, 40]

Crystals of **1**•2DEF conform to the chiral space group $P4_12_12$; the specimen examined was a racemic twin. The single crystal X-ray diffraction data are given in Table 4.1, and important bond distances and angles are listed in Table 3.2. The zinc atoms are linked by carboxylate groups into nearly-linear trinuclear units (Figure 3.2). The Zn-Zn-Zn angle is 173.4 °. The central atom in the chain (Zn2) has an octahedral ZnO_6 coordination environment with Zn-O bond distances in the range 1.951-2.093 Å. The two terminal atoms (Zn1) have distorted square pyramidal ZnO_3N_2 coordination environments, in which the bipyridine nitrogens occupy two of the equatorial positions. One unidentate formate and two bidentate BPDC carboxylate groups bridge between the central Zn atom and each of the two terminal Zn atoms. Thus, formate oxygen O6 is not bound to the framework and this anion evidently can pivot in the solvent cavity about the O5-C13 axis, which results in large displacement parameters for atoms C13 and O6.

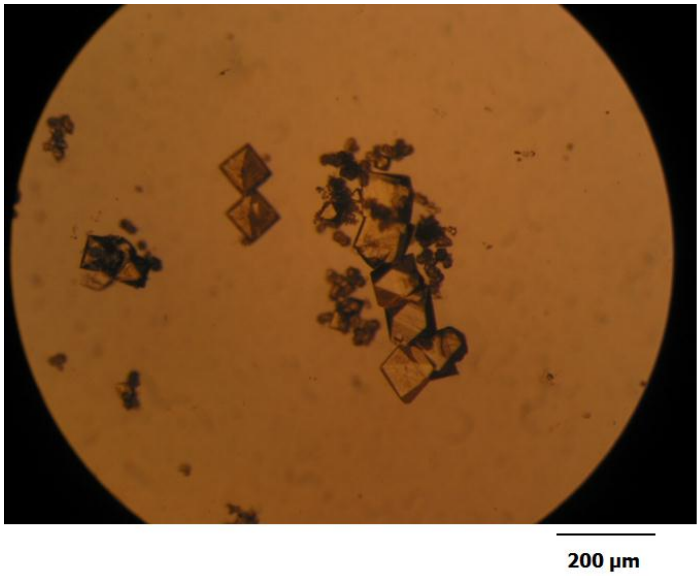

Figure 3.1. Crystals of $Zn_3(BPDC)_2(O_2CH)_2$•2DEF.

Table 3.1. Crystal data and structure refinement for $Zn_3(BPDC)_2(O_2CH)_2$•2DEF.

Empirical formula	C36 H36 N6 O14 Zn3	
Formula weight	972.82	
Temperature	100(2) K	
Wavelength	1.54178 Å	
Crystal system	Tetragonal	
Space group	P4(1)2(1)2	
Unit cell dimensions	a = 15.1751(3) Å	α= 90 °.
	b = 15.1751(3) Å	β= 90 °.
	c = 22.5604(8) Å	γ = 90 °.
Volume	5195.3(2) $Å^3$	
Z	4	
Density (calculated)	1.244 Mg/m^3	
Absorption coefficient	2.111 mm^{-1}	
F(000)	1984	
Crystal size	0.164 x 0.072 x 0.07 mm^3	
Theta range for data collection	4.12 to 67.73 °.	
Index ranges	-18<=h<=14, -17<=k<=18, -26<=l<=27	
Reflections collected	57131	
Independent reflections	4672 [R(int) = 0.0466]	
Completeness to theta = 67.73 °	99.4 %	
Absorption correction	Integration	
Max. and min. transmission	0.9322 and 0.8488	
Refinement method	Full-matrix least-squares on F^2	
Data / restraints / parameters	4672 / 503 / 324	
Goodness-of-fit on F^2	1.099	
Final R indices [I>2sigma(I)]	R1 = 0.0422, wR2 = 0.1174	
R indices (all data)	R1 = 0.0427, wR2 = 0.1178	
Absolute structure parameter	0.50(4)	
Largest diff. peak and hole	1.109 and -0.400 e.$Å^{-3}$	

Table 3.2. Selected bond distances and angles for $Zn_3(BPDC)_2(O_2CH)_2$•2DEF.

Bond lengths [Å]		Angles [°]		Angles [°]	
Zn(1)-O(2)#1	2.006(2)	O(2)#1-Zn(1)-O(5)	103.45(10)	O(3)#3-Zn(2)-O(5)	93.4(13)
Zn(1)-O(5)	2.037(2)	O(2)#1-Zn(1)-O(4)#2	96.27(12)	O(1)#4-Zn(2)-O(5)	91.42(10)
Zn(1)-O(4)#2	2.051(2)	O(5)-Zn(1)-O(4)#2	99.14(11)	O(1)#1-Zn(2)-O(5)	93.21(10)
Zn(1)-N(1)	2.101(5)	O(2)#1-Zn(1)-N(1)	100.7(5)	O(5)#5-Zn(2)-O(5)	173.54(15)
Zn(1)-N(1B)	2.111(6)	O(5)-Zn(1)-N(1)	151.4(4)	O(3)#2-Zn(2)-O(3B)#2	12.0(10)
Zn(1)-N(2B)	2.158(6)	O(4)#2-Zn(1)-N(1)	93.1(2)	O(3)#3-Zn(2)-O(3B)#2	84.0(13)
Zn(1)-N(2)	2.176(5)	O(2)#1-Zn(1)-N(1B)	99.7(7)	O(1)#4-Zn(2)-O(3B)#2	176.8(7)
Zn(2)-O(3)#2	1.951(16)	O(5)-Zn(1)-N(1B)	153.0(6)	O(1)#1-Zn(2)-O(3B)#2	90.0(7)
Zn(2)-O(3)#3	1.951(16)	O(4)#2-Zn(1)-N(1B)	91.8(3)	O(5)#5-Zn(2)-O(3B)#2	84.2(5)
Zn(2)-O(1)#4	2.055(3)	N(1)-Zn(1)-N(1B)	1.8(8)	O(5)-Zn(2)-O(3B)#2	91.3(5)
Zn(2)-O(1)#1	2.055(3)	O(2)#1-Zn(1)-N(2B)	91.6(9)	O(3)#2-Zn(2)-O(3B)#3	84.0(13)
Zn(2)-O(5)#5	2.091(2)	O(5)-Zn(1)-N(2B)	88.3(5)	O(3)#3-Zn(2)-O(3B)#3	12.0(10)
Zn(2)-O(5)	2.091(2)	O(4)#2-Zn(1)-N(2B)	167.6(5)	O(1)#4-Zn(2)-O(3B)#3	90.0(7)
Zn(2)-O(3B)#2	2.093(15)	N(1)-Zn(1)-N(2B)	75.9(4)	O(1)#1-Zn(2)-O(3B)#3	176.8(7)
Zn(2)-O(3B)#3	2.093(15)	N(1B)-Zn(1)-N(2B)	77.4(4)	O(5)#5-Zn(2)-O(3B)#3	91.3(5)
O(1)-C(11)	1.236(5)	O(2)#1-Zn(1)-N(2)	91.9(6)	O(5)-Zn(2)-O(3B)#3	84.2(5)
O(1)-Zn(2)#6	2.055(3)	O(5)-Zn(1)-N(2)	87.4(3)	O(3B)#2-Zn(2)-O(3B)#3	91.8(14)
O(2)-C(11)	1.266(4)	O(4)#2-Zn(1)-N(2)	168.0(4)	C(11)-O(1)-Zn(2)#6	134.2(2)
O(2)-Zn(1)#6	2.006(2)	N(1)-Zn(1)-N(2)	76.7(2)	C(11)-O(2)-Zn(1)#6	128.2(2)
O(3)-C(12)	1.271(8)	N(1B)-Zn(1)-N(2)	78.2(4)	C(12)-O(3)-Zn(2)#7	155(3)
O(3)-Zn(2)#7	1.951(16)	N(2B)-Zn(1)-N(2)	0.9(9)	C(12)-O(3B)-Zn(2)#7	137.6(15)
O(3B)-C(12)	1.268(6)	O(3)#2-Zn(2)-O(3)#3	78(2)	C(12)-O(4)-Zn(1)#4	120.7(2)
O(3B)-Zn(2)#7	2.093(15)	O(3)#2-Zn(2)-O(1)#4	171.2(14)	C(13)-O(5)-Zn(1)	106.1(3)
O(4)-C(12)	1.251(4)	O(3)#3-Zn(2)-O(1)#4	97.4(12)	C(13)-O(5)-Zn(2)	131.4(3)
O(4)-Zn(1)#4	2.051(2)	O(3)#2-Zn(2)-O(1)#1	97.4(12)	Zn(1)-O(5)-Zn(2)	110.67(11)
		O(3)#3-Zn(2)-O(1)#1	171.2(14)	C(1)-N(1)-C(5)	120.1(5)
		O(1)#4-Zn(2)-O(1)#1	88.25(18)	C(1)-N(1)-Zn(1)	122.9(5)
		O(3)#2-Zn(2)-O(5)#5	93.4(13)	C(5)-N(1)-Zn(1)	116.4(4)
		O(3)#3-Zn(2)-O(5)#5	81.5(13)	C(10)-N(2)-C(6)	118.0(6)
		O(1)#4-Zn(2)-O(5)#5	93.21(10)	C(10)-N(2)-Zn(1)	127.4(5)
		O(1)#1-Zn(2)-O(5)#5	91.42(10)	C(6)-N(2)-Zn(1)	114.3(4)
		O(3)#2-Zn(2)-O(5)	81.5(13)		

Symmetry transformations used to generate equivalent atoms: #1 y-1/2,-x+1/2,z-1/4 #2 -x+1/2,y+1/2,-z+1/4 #3 y+1/2,-x+1/2,z-1/4 #4 -x+1/2,y-1/2,-z+1/4 #5 y,x,-z #6 -y+1/2,x+1/2,z+1/4 #7 -y+1/2,x-1/2,z+1/4

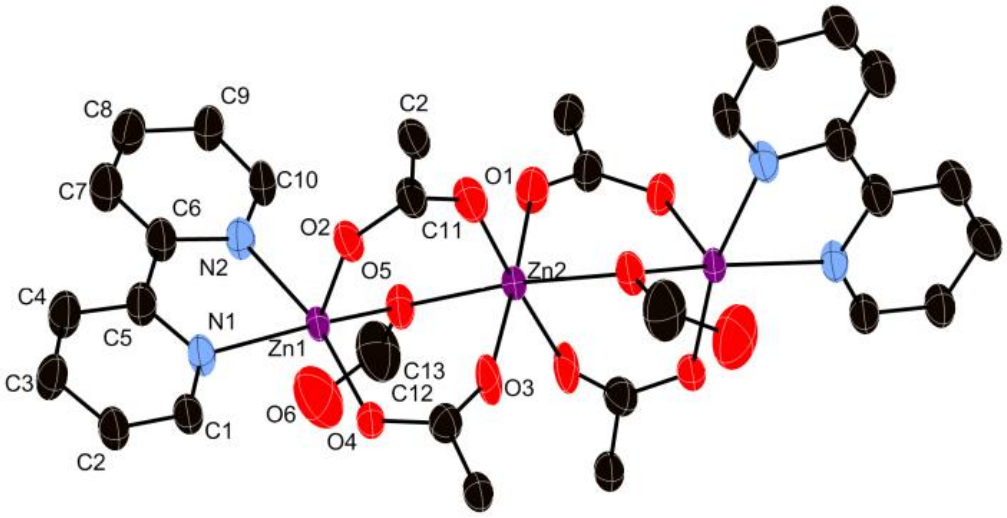

Figure 3.2. ORTEP view of the asymmetric unit of **1** (50% probability level). The red, black, purple and blue spheres correspond to oxygen, carbon, zinc, and nitrogen atoms, respectively. (Hydrogen atoms are omitted for clarity.)

This MOF is nanoporous, and highly disordered DEF molecules occupy the framework cavities. The pore openings, as viewed along the *c* axis, are rectangular in shape and have dimensions of about 0.78 × 1.53 nm. Within a layer perpendicular to the *c* axis, the pores are arranged in a herringbone fashion, but adjacent layers are stacked along the *c* axis in such a way that the pattern appears to have four-fold symmetry in projection (Figure 3.3a).

Actually, the layers are related not by a four-fold rotation axis, but by four-fold screw axes (Figure 3.3b). The BPDC-Zn framework is arranged in a helical fashion about these axes, which are the source of the chirality of the nanopores. If the network is viewed along the [111] direction (Figure 3.3c), the pores form a pseudo-hexagonal arrangement in which the pore openings are about 0.75 × 1.2 nm. The view of **1** along *a* axis is shown in Figure 3.4.

The centers of all the pores are occupied by disordered solvent molecules. The calculated void volume is about 2780 $Å^3$ per unit cell, which is about 53.6% of the total volume. Thermogravimetic analysis of **1**•2DEF reveals that 10% of the weight (corresponding to removal of all of the DEF solvent molecules) is lost between 20 and 200 ˚C (Figure 3.5). If crystals of **1**•2DEF are solvent exchanged three times with $CHCl_3$ and then exposed to vacuum at 120 ˚C, the resulting material is free of DEF and has the stoichiometry $Zn_3(BPDC)_2(O_2CH)_2$ (**1**). This material has a surface area (by BET analysis) of 570 $m^2 \cdot g^{-1}$, which shows that the nanoporous structure is maintained upon removal of the solvent. The framework is thermally stable up to at least 200 ˚C. The PXRD pattern of solvent-free **1** closely resembles that calculated from the single crystal data for **1**•2DEF, thus indicating that the host framework is retained (Figure 3.6).

In conclusion, we have successfully synthesized a new chiral MOF constructed from achiral components. If homochiral samples can be generated, such a material may be useful in

catalysis and separations.

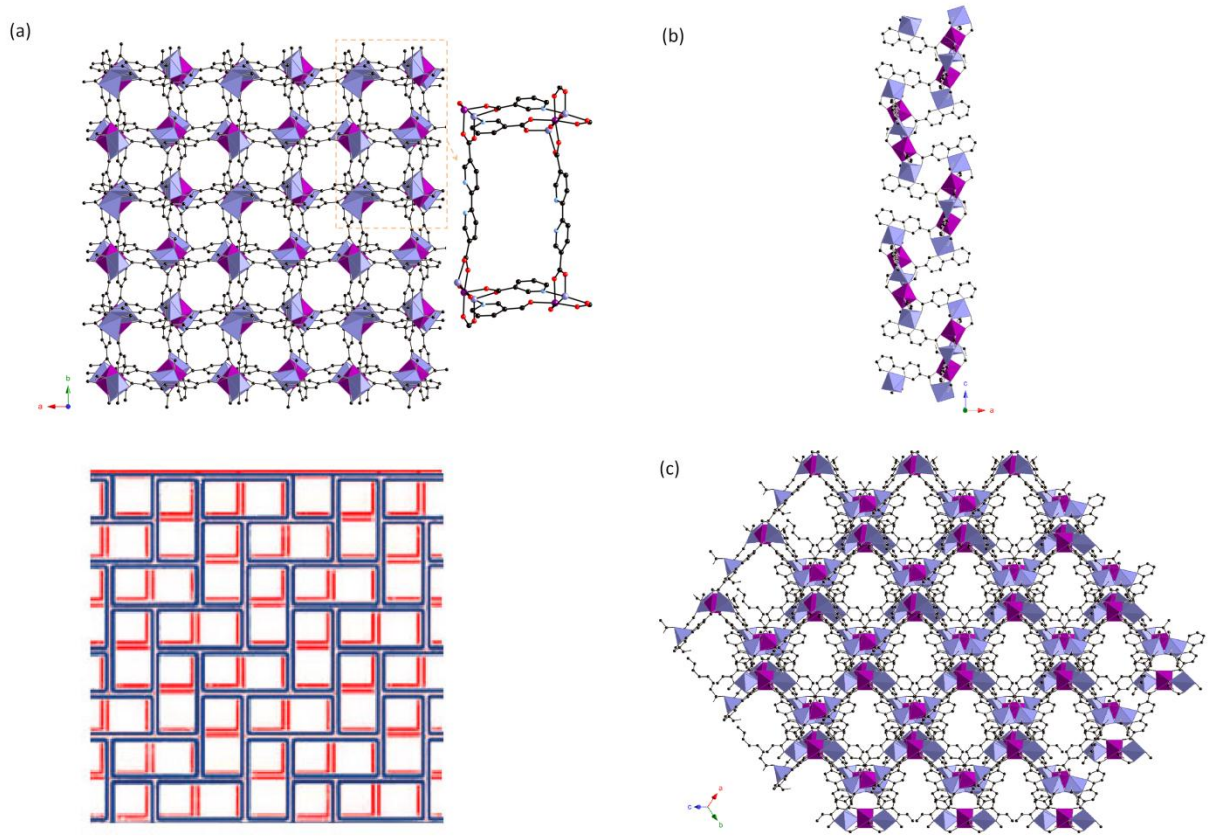

Figure 3.3. Representation of the structure of **1** (C, black; O, red; N, blue; Zn1, light purple polyhedron; Zn2, purple polyhedron; H, omitted). (a) View along *c* axis, along with a representation of two adjacent layers, each having a herringbone arrangement of rectangular pores; one such rectangular subunit is shown at upper right. (b) BPDC-Zn^{2+} helical arrays related by the chiral 4_1 screw axis. (c) View along [111].

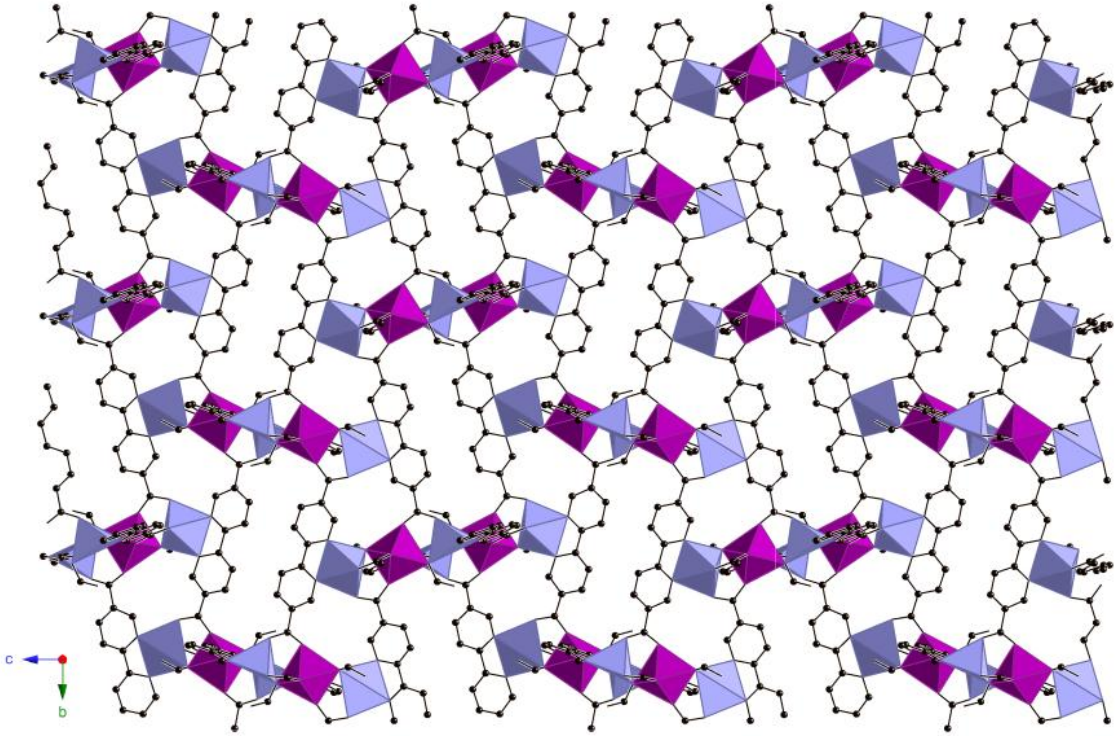

Figure 3.4. Representation of the structure of **1** along the *a* axis (C, black; Zn1, light purple polyhedron; Zn2, purple polyhedron; H, omitted).

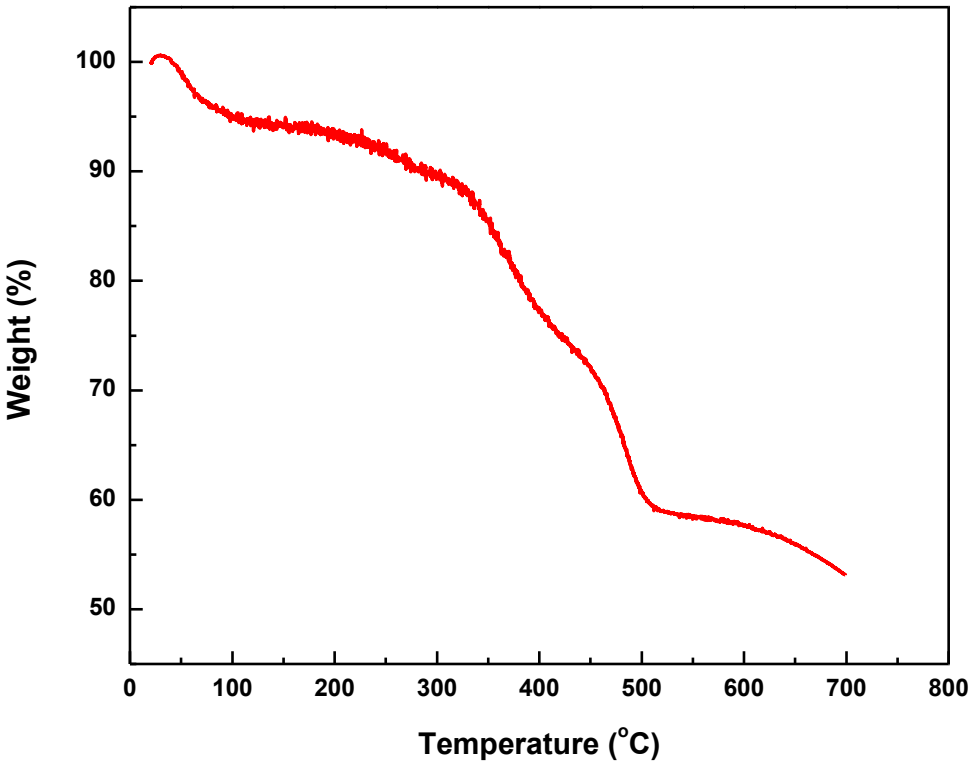

Figure 3.5. Thermogravimetric analysis of a freshly prepared sample of **1•2DEF.**

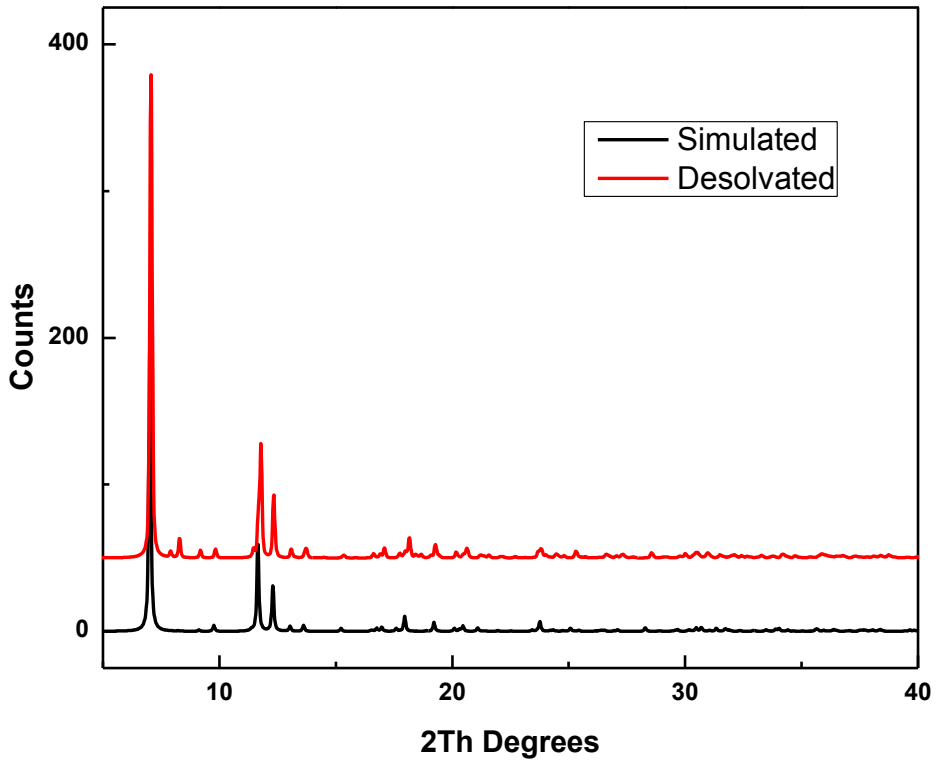

Figure 3.6. Powder X-ray diffraction pattern of desolvated **1** (red), and pattern calculated from the single crystal structure of **1•2DEF** (black).

Experimental Section

Synthesis of $Zn_3(BPDC)_2(O_2CH)_2$•2DEF (1•2DEF). The chemicals were obtained from Aldrich and used as received. The synthesis was performed under solvothermal conditions. $Zn(NO_3)_2 \cdot 6H_2O$ (0.0446 g, 0.15 mmol), 2,2′-bipyridine-5,5′-dicarboxylic acid (0.0244 g, 0.10 mmol) and formic acid (0.8 mL of a 75% aqueous solution) were mixed and dispersed in DEF (5 mL). The resulting white slurry was then heated in an oven at 100 ℃ for 3 weeks to afford octahedron-shaped crystals. Yield: 70%. Anal. for the as-prepared material (University of Illinois Microanalytical Laboratory): Calc. for $Zn_3(BPDC)_2(O_2CH)_2$•2DEF: C, 43.1; H, 3.42; N, 8.38. Found: C, 42.8; H, 3.13; N, 8.35. Desolvation to **1** was achieved by immersing the as-prepared crystals in chloroform (5 mL) for three days, with the solvent being changed once daily. The solid was then collected by filtration and dried in a vacuum oven at 120 ℃ for 3 h.

Brunauer - Emmett - Teller (BET) measurements. 3 point BET (P/P_0 = 0.1-0.3) surface area measurements were performed on QuantachromeNova 2200e gas adsorption surface area apparatus at liquid nitrogen temperature using nitrogen as the adsorbate.

Powder X-ray diffraction. Powder XRD data were collected on a Bruker General Area Detector Diffraction System (GADDS) equipped with a P4 four-circle diffractometer and HiStar multiwire area detector. A Bruker M18XHF22 rotating anode generator operating at 50kV and 40mA supplied the Cu Kα graphite monochromatized incident beam. The simulated pattern derived from single X-ray data matches well with the pattern obtained from desolvated **1**.

X-ray single crystal diffraction. The data crystal was mounted on a glass fiber using Paratone-N oil (Exxon). One distinct cell was identified using APEX2 (Bruker, 2010). Twenty

frame series were integrated and filtered for statistical outliers using SAINT (Bruker, 2005) then corrected for absorption by integration using SHELXTL/XPREP V2005/2 (Bruker, 2005) before using SADABS (Bruker, 2005) to sort, merge, and scale the combined data. The absorption correction was done prior to the squeeze process using an absorption coefficient that included the contribution from the two diethylformamide molecules per formula unit. No decay correction was applied. The final refinements excluded the 0 2 3 and 0 1 3 reflections. The structure was phased by direct methods (Sheldrick, 2008). Systematic conditions were consistent with both of the enantiomorphic space groups $P4_12_12$ or $P4_32_12$. The racemic mixture is almost 50/50. The space group $P4_12_12$ was chosen over the other space group because the refined portion of this enantiomer was slightly greater. The highest peaks in the final difference Fourier map were in the vicinity of atom Zn2; the final map had no other significant features. A final analysis of variance between observed and calculated structure factors showed little dependence on amplitude and some dependence on resolution.

References

1. C. Serre, C. Mellot-Draznieks, S. Surble, N. Audebrand, Y. Filinchuk and G. Ferey, *Science*, 2007, **315**, 1828-1831.
2. S. Horike, S. Shimomura and S. Kitagawa, *Nature Chem.*, 2009, **1**, 695-704.
3. J. R. Long and O. M. Yaghi, *Chem. Soc. Rev.*, 2009, **38**, 1213-1214.
4. G. Ferey, *Chem. Soc. Rev.*, 2008, **37**, 191-214.
5. B. Panella and M. Hirscher, *Adv. Mater.*, 2005, **17**, 538-541.
6. M. P. Suh, H. J. Park, T. K. Prasad and D. W. Lim, *Chem. Rev.*, 2012, **112**, 782-835.

7. A. C. McKinlay, B. Xiao, D. S. Wragg, P. S. Wheatley, I. L. Megson and R. E. Morris, *J. Am. Chem. Soc.*, 2008, **130**, 10440-10444.

8. A. C. Sudik, A. R. Millward, N. W. Ockwig, A. P. Cote, J. Kim and O. M. Yaghi, *J. Am. Chem. Soc.*, 2005, **127**, 7110-7118.

9. T. Duren, L. Sarkisov, O. M. Yaghi and R. Q. Snurr, *Langmuir*, 2004, **20**, 2683-2689.

10. K. L. Kauffman, J. T. Culp, A. J. Allen, L. Espinal, W. Wong-Ng, T. D. Brown, A. Goodman, M. P. Bernardo, R. J. Pancoast, D. Chirdon and C. Matranga, *Angew. Chem., Int. Ed.*, 2011, **50**, 10888-10892.

11. Y. S. Bae, K. L. Mulfort, H. Frost, P. Ryan, S. Punnathanam, L. J. Broadbelt, J. T. Hupp and R. Q. Snurr, *Langmuir*, 2008, **24**, 8592-8598.

12. B. Wang, A. P. Cote, H. Furukawa, M. O'Keeffe and O. M. Yaghi, *Nature*, 2008, **453**, 207-211.

13. R. Babarao, Z. Q. Hu, J. W. Jiang, S. Chempath and S. I. Sandler, *Langmuir*, 2007, **23**, 659-666.

14. B. L. Chen, C. D. Liang, J. Yang, D. S. Contreras, Y. L. Clancy, E. B. Lobkovsky, O. M. Yaghi and S. Dai, *Angew. Chem., Int. Ed.*, 2006, **45**, 1390-1393.

15. S. Y. Ding, J. Gao, Q. Wang, Y. Zhang, W. G. Song, C. Y. Su and W. Wang, *J. Am. Chem. Soc.*, 2011, **133**, 19816-19822.

16. K. K. Tanabe and S. M. Cohen, *Angew. Chem., Int. Ed.*, 2009, **48**, 7424-7427.

17. F. X. L. I. Xamena, A. Abad, A. Corma and H. Garcia, *J. Catal.*, 2007, **250**, 294-298.

18. D. N. Dybtsev, A. L. Nuzhdin, H. Chun, K. P. Bryliakov, E. P. Talsi, V. P. Fedin and K. Kim, *Angew. Chem., Int. Ed.*, 2006, **45**, 916-920.

19. B. L. Chen, Y. Yang, F. Zapata, G. N. Lin, G. D. Qian and E. B. Lobkovsky, *Adv. Mater.*, 2007, **19**, 1693-1696.

20. J. He, K. K. Yee, Z. T. Xu, M. Zeller, A. D. Hunter, S. S. Y. Chui and C. M. Che, *Chem. Mater.*, 2011, **23**, 2940-2947.

21. G. Lu, O. K. Farha, L. E. Kreno, P. M. Schoenecker, K. S. Walton, R. P. Van Duyne and J. T. Hupp, *Adv. Mater.*, 2011, **23**, 4449-4452.

22. K. L. Wong, G. L. Law, Y. Y. Yang and W. T. Wong, *Adv. Mater.*, 2006, **18**, 1051-1054.

23. P. Horcajada, R. Gref, T. Baati, P. K. Allan, G. Maurin, P. Couvreur, G. Ferey, R. E. Morris and C. Serre, *Chem. Rev.*, 2012, **112**, 1232-1268.

24. A. C. McKinlay, R. E. Morris, P. Horcajada, G. Ferey, R. Gref, P. Couvreur and C. Serre, *Angew. Chem., Int. Ed.*, 2010, **49**, 6260-6266.

25. P. Horcajada, C. Serre, M. Vallet-Regi, M. Sebban, F. Taulelle and G. Ferey, *Angew. Chem., Int. Ed.*, 2006, **45**, 5974-5978.

26. C. Y. Sun, C. Qin, C. G. Wang, Z. M. Su, S. Wang, X. L. Wang, G. S. Yang, K. Z. Shao, Y. Q. Lan and E. B. Wang, *Adv. Mater.*, 2011, **23**, 5629-5632.

27. G. Nickerl, A. Henschel, R. Grunker, K. Gedrich and S. Kaskel, *Chem-Ing-Tech*, 2011, **83**, 90-103.

28. C. Livage, N. Guillou, P. Rabu, P. Pattison, J. Marrot and G. Ferey, *Chem. Commun. (Cambridge, U. K.)*, 2009, 4551-4553.

29. L. Q. Ma and W. B. Lin, *J. Am. Chem. Soc.*, 2008, **130**, 13834-13835.

30. L. Q. Ma, J. M. Falkowski, C. Abney and W. B. Lin, *Nature Chem.*, 2010, **2**, 838-846.

31. C. D. Wu, L. Zhang and W. B. Lin, *Inorg. Chem.*, 2006, **45**, 7278-7285.

32. X. D. Zheng, M. Zhang, L. Jiang and T. B. Lu, *Dalton Trans.*, 2012, **41**, 1786-1791.

33. W. T. Liu, Y. C. Ou, Z. J. Lin and M. L. Tong, *CrystEngComm*, 2010, **12**, 3487-3489.

34. Q. Y. Liu, Y. L. Wang, N. Zhang, Y. L. Jiang, J. J. Wei and F. Luo, *Cryst. Growth Des.*, 2011, **11**, 3717-3720.

35. R. E. Morris and X. H. Bu, *Nature Chem.*, 2010, **2**, 353-361.

36. T. Ezuhara, K. Endo and Y. Aoyama, *J. Am. Chem. Soc.*, 1999, **121**, 3279-3283.

37. J. Zhang, S. M. Chen, T. Wu, P. Y. Feng and X. H. Bu, *J. Am. Chem. Soc.*, 2008, **130**, 12882-12883.

38. Z. J. Lin, A. M. Z. Slawin and R. E. Morris, *J. Am. Chem. Soc.*, 2007, **129**, 4880-4881.

39. H. F. Clausen, R. D. Poulsen, A. D. Bond, M. A. S. Chevallier and B. B. Iversen, *J. Solid State Chem.*, 2005, **178**, 3342-3351.

40. J. H. He, Y. T. Zhang, Q. H. Pan, J. H. Yu, H. Ding and R. R. Xu, *Microporous Mesoporous Mater.*, 2006, **90**, 145-152.

CHAPTER 4: Structural Stability of IRMOF-1 under High Pressure

Introduction

Metal-organic frameworks (MOFs) have attracted increasing attention as a new class of porous materials with high internal surface areas, well defined crystalline structures, and controllable surface functionalities. They have been considered as promising materials for many applications such as gas storage,[1, 2] gas separation,[3, 4] sensing,[5] and heterogeneous catalysis.[6] Because many of these applications involve exposing MOFs to high pressures and high temperatures, it is fundamentally important to understand the structural stability of MOFs under extreme conditions. However, relatively few studies on this topic have been reported to date, most of which are performed by nanoindentation[7-10] or diamond anvil cell methods.[11-15] Alldendorf et al. measured the elastic modulus of IRMOF-1 crystals using two different nanoindentation techniques.[7] Zeolitic imidazolate frameworks (ZIFs), a type of MOF built from imidazoles and metal ions, have also been studied using both nanoindentation and computational approaches to establish their structure-mechanical property relationships.[8] High pressure experiments on ZIF-8 Zn(2-methyllimidazole)$_2$ (ZIF-8) and $[Zn_2(C_3H_3N_2)_4]_n$ (ZnIm) in diamond anvil cells were performed at pressures up to 1.2 GPa.[12, 13]

The zinc 1,4-benzenedicarboxylate (BDC) material $Zn_4O(BDC)_3$, which is known as IRMOF-1 or MOF-5, is the prototype of a widely studied series of MOF materials.[16] There have been two previous studies of the structure of IRMOF-1 as a function of pressure: one study reported that pressurization of IRMOF-1 to 3.5 MPa (35 atm) converts it irreversibly to an amorphous solid.[17] A second study reported that single crystals of IRMOF-1 immersed in *N*,*N*-diethylformamide (DEF) converted to an amorphous solid at 3.21 GPa (32 100 atm).[14] Here we

report an *in situ* high pressure study of IRMOF-1 up to 8.93 GPa. Our results, which differ from those in the lower pressure investigations, shed light on the stability of this important MOF under pressure.

Results and Discussion

"As-synthesized" IRMOF-1 samples were prepared solvothermally in *N*,*N*-diethylformamide.[16] Samples of the as-synthesized IRMOF-1 were crushed while still immersed in their mother liquor, which was used as a pressure medium for the diamond anvil cell (Figure 4.1). At the lowest pressure studied, 0.70 GPa (7 000 atm), the three strongest peaks are the (200), (220), and (400) reflections due to IRMOF-1 (Figure 4.2), which crystallizes in the cubic space group $Fm\bar{3}m$.[16] There is one additional small peak at a d-spacing of 10.12 Å ($2\theta = 2.341$ °) that is not due to IRMOF-1. At pressures up to 6.57 GPa, the peaks for IRMOF-1 broaden and decrease in integrated intensity (Figure 4.3). The (200) reflection of IRMOF-1 moves slightly toward smaller d-spacings (from 12.78 Å to 12.74 Å). The extra peak (HP peak 1) moves toward larger d-spacings (reaching 10.97 Å at 6.57 GPa), but its intensity is essentially unchanged. Between 6.57 and 8.93 GPa, all the peaks in the PXRD pattern disappear, indicating destruction of the crystallinity. No reversion to crystalline phases occurs upon release of the pressure.

Compared with an earlier study,[14] our samples of IRMOF-1 retain crystallinity to higher pressures (6.57 vs 3.24 GPa). The sudden decrease of intensity of the IRMOF-1 peaks above 0.7 GPa agrees with the previous study. The decrease of the d-spacings in our experiment also matches their conclusion that the unit cell compresses above 0.7 GPa. As we will see below, the pores in the as-synthesized IRMOF-1 are packed with DEF molecules, which help the MOF resist compression.

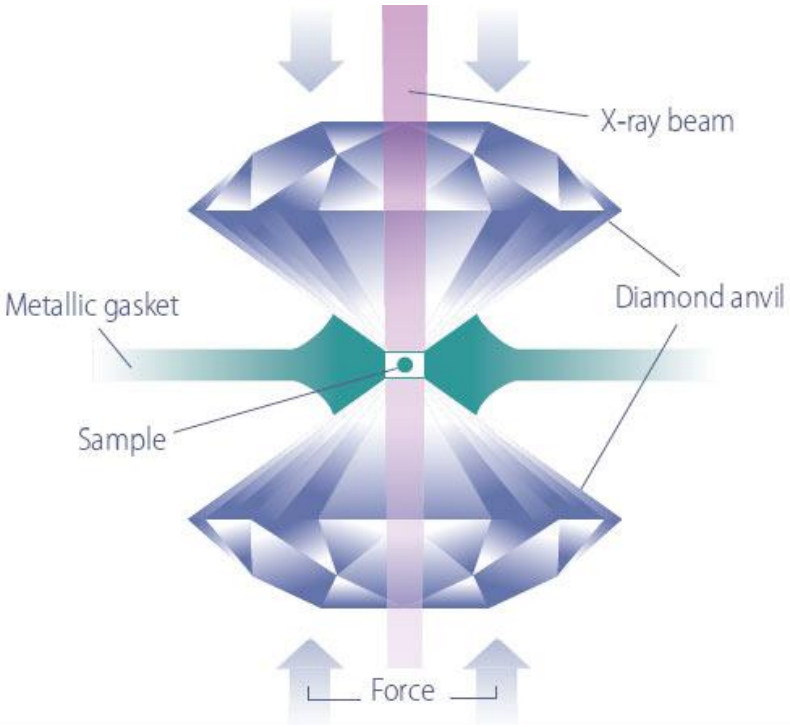

Figure 4.1. Illustration of a diamond anvil cell.[18]

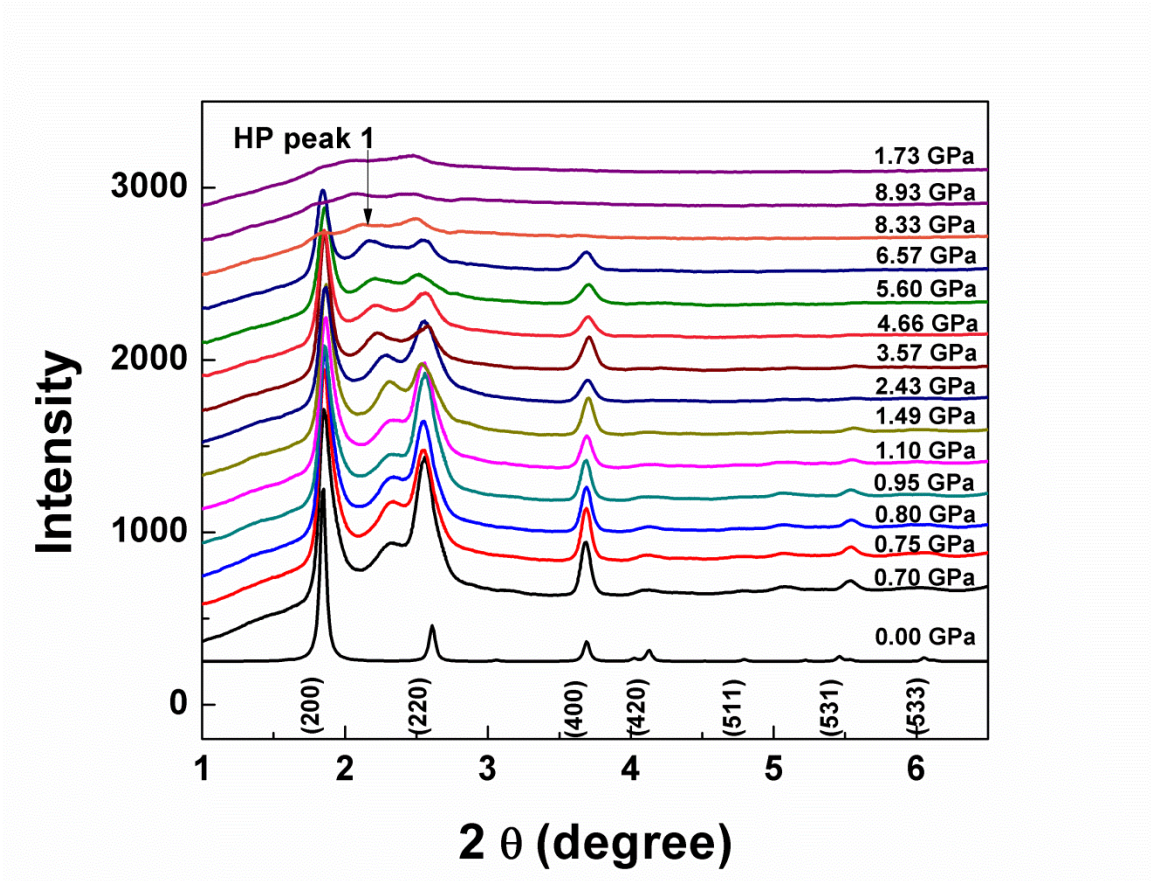

Figure 4.2. PXRD patterns of as-synthesized IRMOF-1 as a function of pressure. The time sequence proceeds from bottom to top.

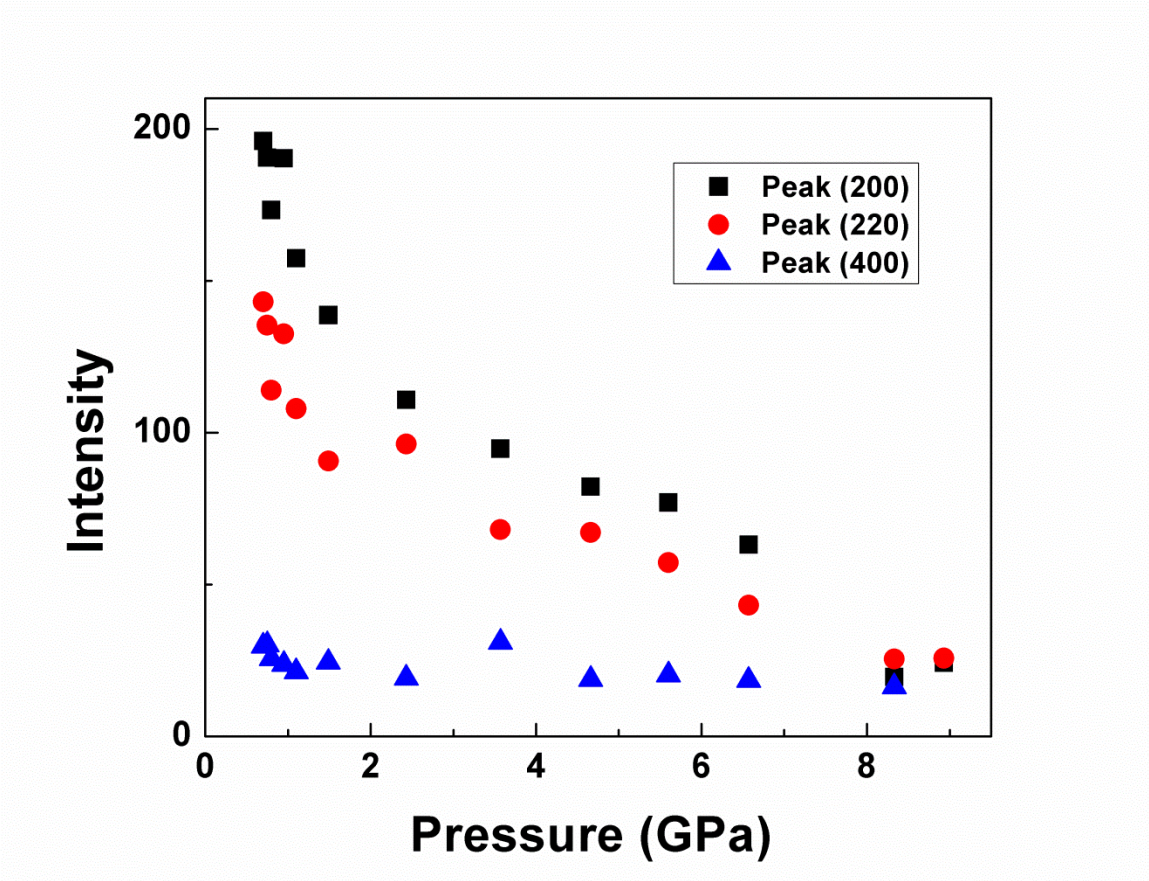

Figure 4.3. The integrated intensities of the (200), (220), and (400) reflections of as-synthesized IRMOF-1 as a function of pressure.

We then studied the pressurization of desolvated IRMOF-1, which was prepared from the as-synthesized material by solvent exchange with dichloromethane, followed by heating in vacuum to 120 ℃. The desolvated samples were then powdered in air and reheated in vacuum. No pressure medium was used for this experiment. At the lowest pressure we studied, 0.21 GPa (2 100 atm), the three most intense peaks in the diffraction pattern (Figure 4.4a) again correspond to those calculated from the known IRMOF-1 structure. As seen for the as-prepared sample, there is an additional peak (HP peak 2) due to a different material at a d-spacing of 9.97 Å ($2\theta = 2.376$ °). When the pressure is increased, the 9.97 Å peak grows stronger, while the peaks due to IRMOF-1 diminish (but see below). By 5.17 GPa, the conversion of IRMOF-1 to the new material is essentially complete. No additional peaks appear at pressures up to 7.43 GPa; furthermore, no reversion of the new phase to IRMOF-1 occurs when the pressure is subsequently reduced (Figure 4.4b).

Substantially different behavior was observed in a previous pressure study of desolvated IRMOF-1.[17] Whereas our samples retained some crystallinity to 4.32 GPa (43 200 atm), the prior study found that the application of even a small pressure of 3.5 MPa (35 atm) caused irreversible collapse of the pores and conversion to an amorphous material. We believe that the difference relates to the contents of the pores in the two samples. Our "desolvated" samples were handled briefly in air when they were loaded into the pressure cell, and we have evidence (see below) that the pores adventitiously adsorb water molecules when so treated. The consequent filling (or partial filling) of the pores again lends the MOF considerable mechanical stability toward pressurization. The previous study evidently involved IRMOF-1 whose pores were largely vacant. Together with our data, it is now clear that MOFs with vacant pores collapse and

become amorphous very easily upon compression, but that MOFs with filled pores are mechanically much more robust.

The integrated intensities of the (200), (220), and (400) reflections of the desolvated IRMOF-1 show that there are two regions of differing behavior. At pressures below about 0.7 GPa (yellow region of Figure 4.5), the intensities of all the peaks increase; we ascribe this behavior to pressure induced texturing. At higher pressures, the diffraction rings become more intense in some directions and form bright spots, which suggest the onset of pressure-induced texturing (Figure 4.6). Above 0.7 GPa, the intensities of the (220) and (400) reflections decrease monotonically, whereas the intensity of the (220) reflection appears essentially constant. We believe that the (220) reflection decreases in intensity in concert with the (200) and (400) reflections but that it is replaced by a broad peak at the same d-spacing that is due to a new substance with medium-range order (MRO) at a length scale around 9.5 Å.[19]

The peak due to the new substance shifts slightly with pressure owing to changes in the unit cell volume. Specifically, the most intense peak moves from d = 9.97 Å (2θ = 2.376 °) at 0.21 GPa to d = 9.84 Å (2θ = 2.407 °) at 7.43 GPa, which corresponds to a 1.3 % decrease of the d-spacing. Upon subsequent return of the pressure to 0.17 GPa, the peak moves to d = 9.94 Å (2θ = 2.383 °), which corresponds to a 1.0 % increase of the d-spacing. Therefore, in this pressure regime the new phase is not fully elastic and some of the compression is irreversible.

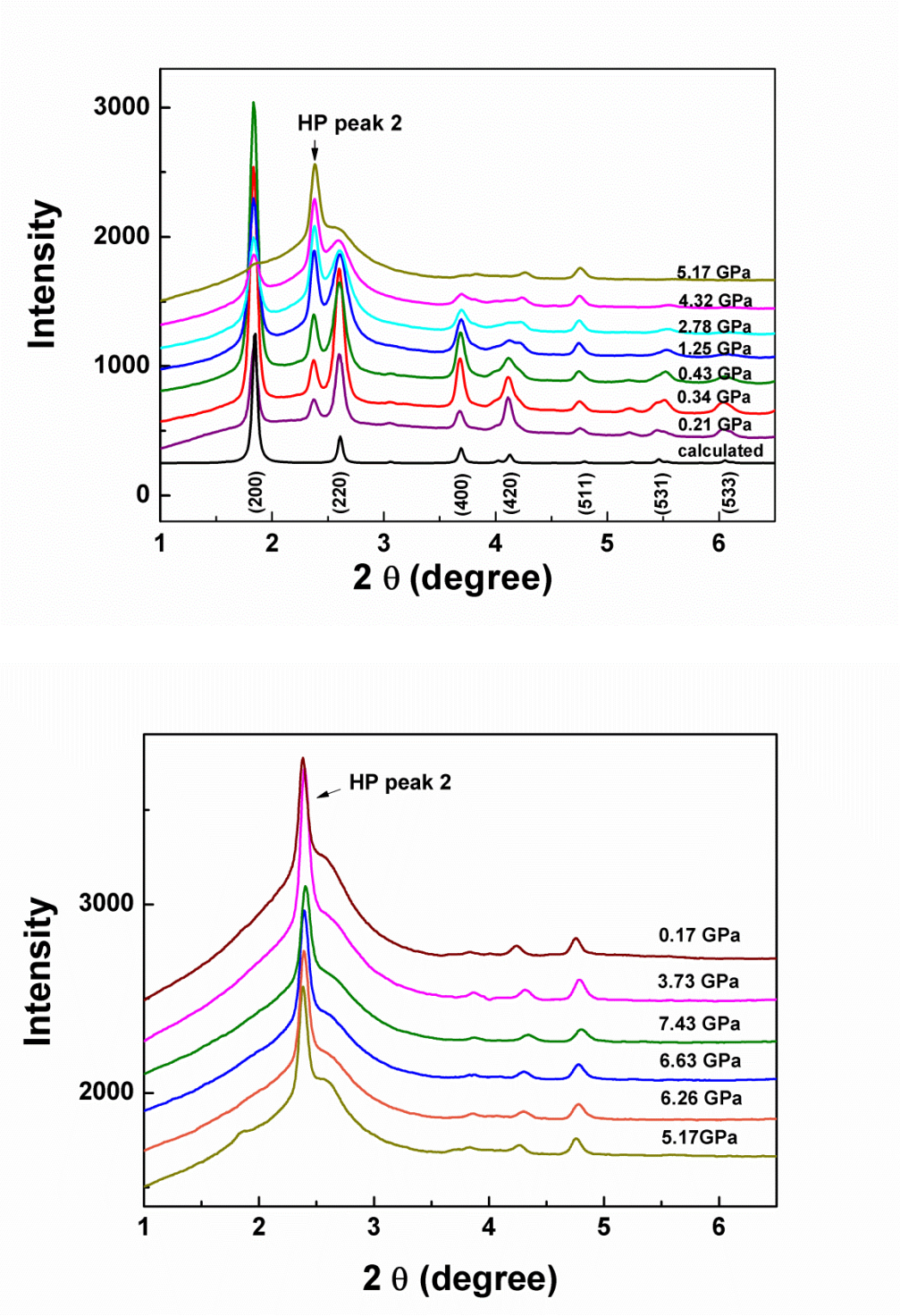

Figure 4.4. (a) PXRD patterns obtained upon pressurizing desolvated IRMOF-1 (bottom to top), showing conversion to a new material. (b) PXRD patterns of the new material upon compression and decompression (bottom to top).

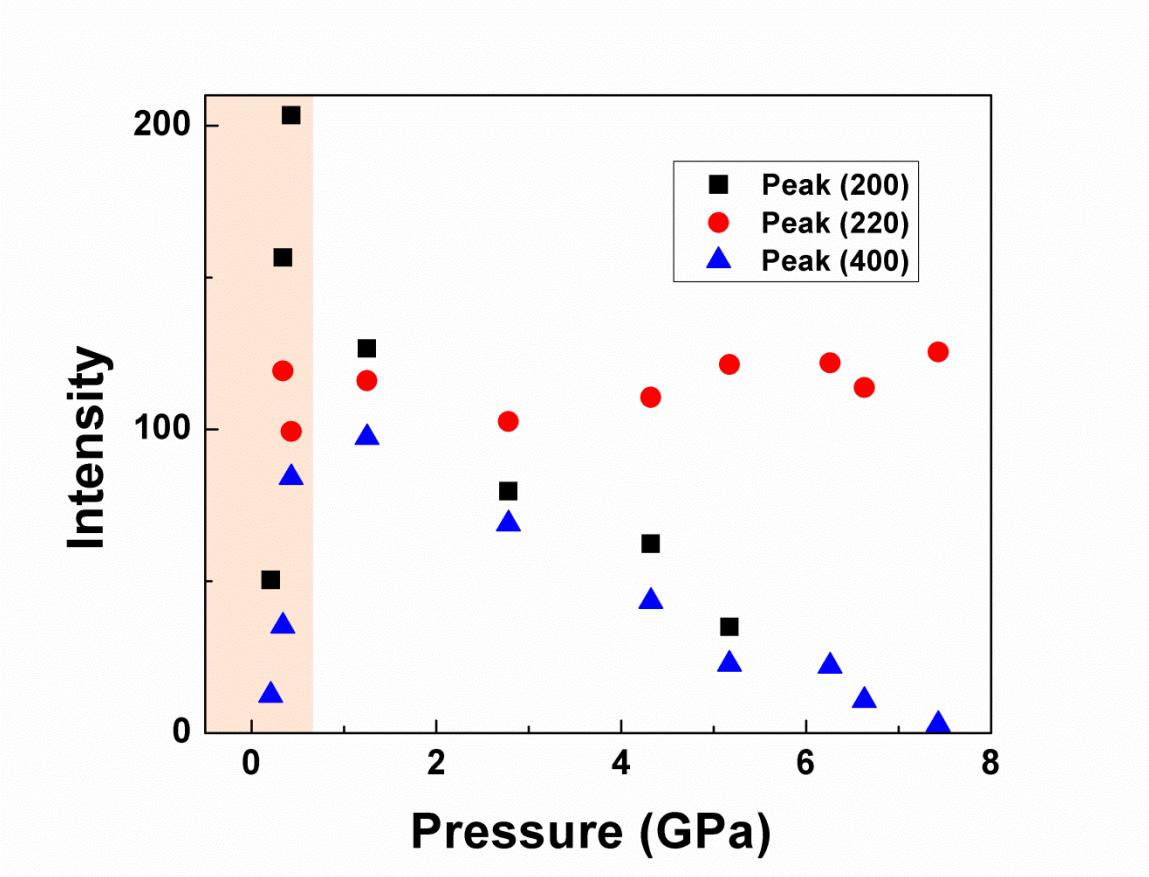

Figure 4.5. The intensities of the (200), (220), and (400) reflections of desolvated IRMOF-1 as a function of pressure.

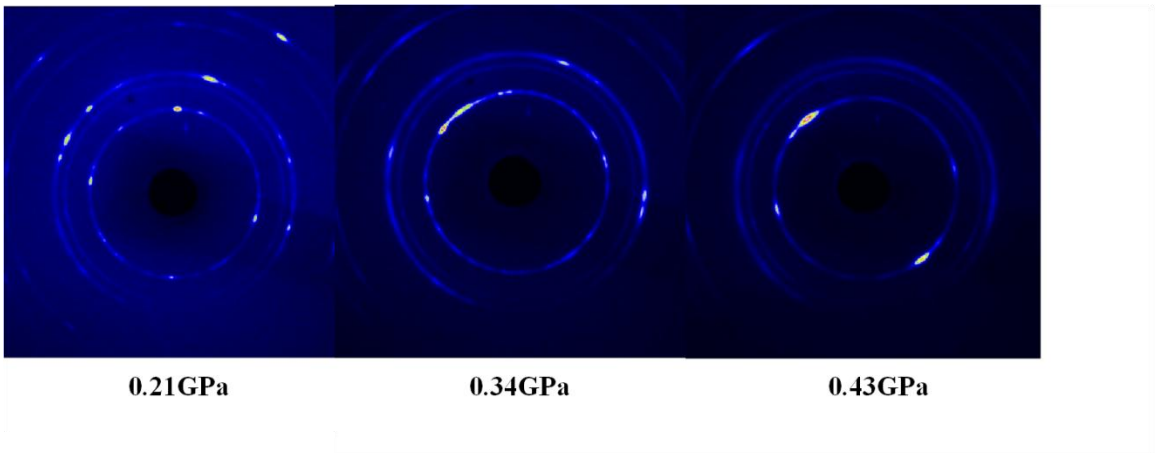

Figure 4.6. Diffraction patterns of IRMOF-1 at different pressures.

We now turn to an identification of the species responsible for the new peaks in the two experiments discussed above. Under pressure, desolvated IRMOF-1 converts into the new phase (quantitatively if we assume that no amorphous products are formed), whereas as-synthesized IRMOF-1 converts only partially. Although the changes in the PXRD patterns resemble those expected for a pressure-induced phase transition, the identifiable diffraction peaks match in both intensity and d-spacings with those reported by Kaye *et al* for the phase generated by air hydrolysis of IRMOF-1.[20] This latter study suggested that the hydrolysis product is a solid with the formula $C_{24}H_{22}O_{18}Zn_4$.

As a control experiment, we measured the PXRD pattern of IRMOF-1 both before and after exposure to air for one day under ambient conditions (Figure 4.7). Both diffraction patterns match very well with that calculated from the published single crystal structure of IRMOF-1.[16] This result confirms that the hydrolysis process does not take place spontaneously over the time frame of our experiments, but instead is stimulated by the application of pressure. The water needed to carry out the hydrolysis was almost certainly absorbed by the desolvated MOF during the ca. 10 minute time required to load the powdered sample into the diamond anvil cell, a procedure that was conducted in air.

During the pressurization process, the integrated intensity of HP peak 1 (from as-synthesized IRMOF-1) remains essentially constant whereas HP peak 2 (from "desolvated" IRMOF-1) becomes more intense (Figure 4.8). The d-spacing of HP peak 1 decreases, whereas HP peak 2 increases slightly, with increasing pressure (Figure 4.9). The increase in the d-spacing with increasing pressure seen for the as-synthesized IRMOF-1 sample is unusual; typically, increasing pressure results in a decrease in d-spacings. We believe this unusual behavior is due to

a pressure-induced solvolysis reaction involving the included DEF molecules, in which Zn-carboxylate bonds are broken and some of the coordination sites on the Zn centers are occupied by DEF molecules. As the pressure increases, this slow displacement reaction increases the average d-spacing. Possibly, the large size of the DEF molecules relative to water explains why the DEF solvolysis reaction increases the d-spacing, whereas the hydrolysis reaction observed for the "desolvated" samples results in little change in the d-spacing with further reaction.

Our results on the pressurization of IRMOF-1 are summarized in Scheme 4.1. Our results clearly demonstrate that IRMOF-1 can sustain significantly higher pressures when its pores are filled with solvent molecules rather than with air. Furthermore, in the presence of adsorbed water, IRMOF-1 begins to convert to a new material even at the lowest pressure we studied, 0.21 GPa. This conversion process is essentially complete at 5.17 GPa; some amorphous material is also generated. This new material is the result of a pressure-driven hydrolysis reaction; the product is a previously described material of approximate stoichiometry $C_{24}H_{22}O_{18}Zn_4$. At higher pressures, the hydrolysis product could be further compressed; it re-expands but not fully elastically upon releasing the pressure. Not surprisingly, the hydrolysis reaction is irreversible, and no IRMOF-1 is regenerated upon return to ambient pressure. When the amount of water is less (as in our study of as-synthesized material), IRMOF-1 is converted to a chemically-related material generated by pressure-induced hydrolysis and solvolysis.

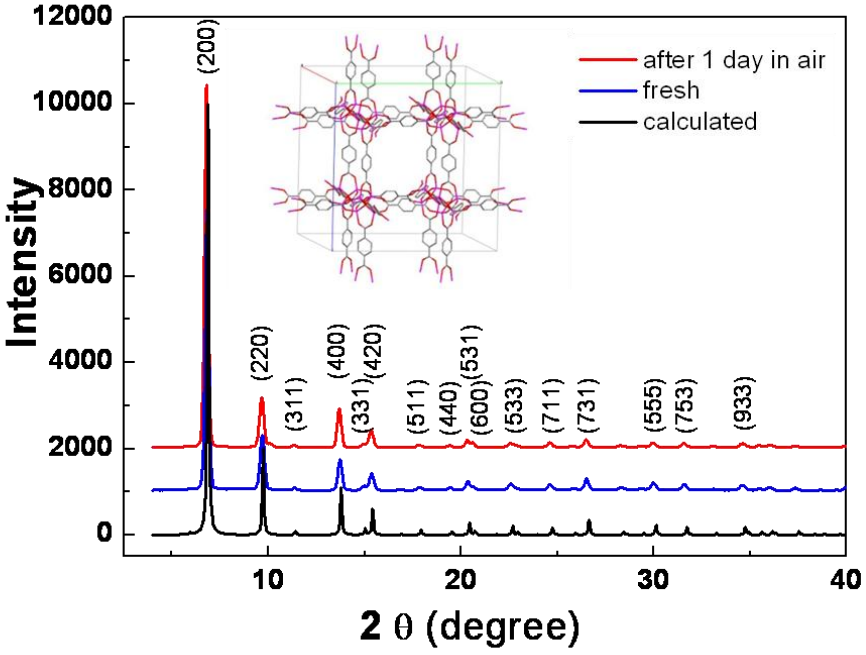

Figure 4.7. Comparison of calculated PXRD of IRMOF-1, fresh IRMOF-1 and IRMOF-1 exposed in air for one day obtained at room temperature. Inset picture shows the unit cell of IRMOF-1.

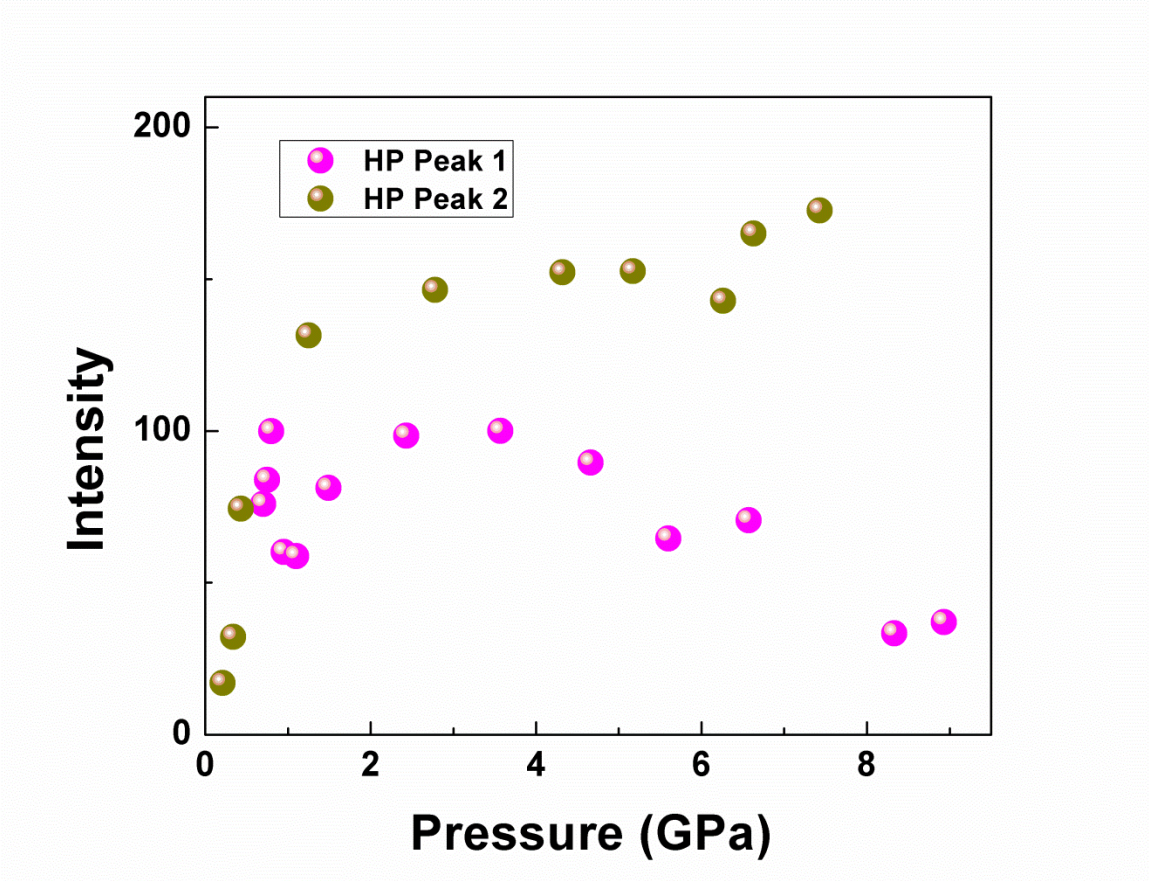

Figure 4.8. Pressure dependence of the integrated intensities of the peak near 10.00 Å due to the new phase.

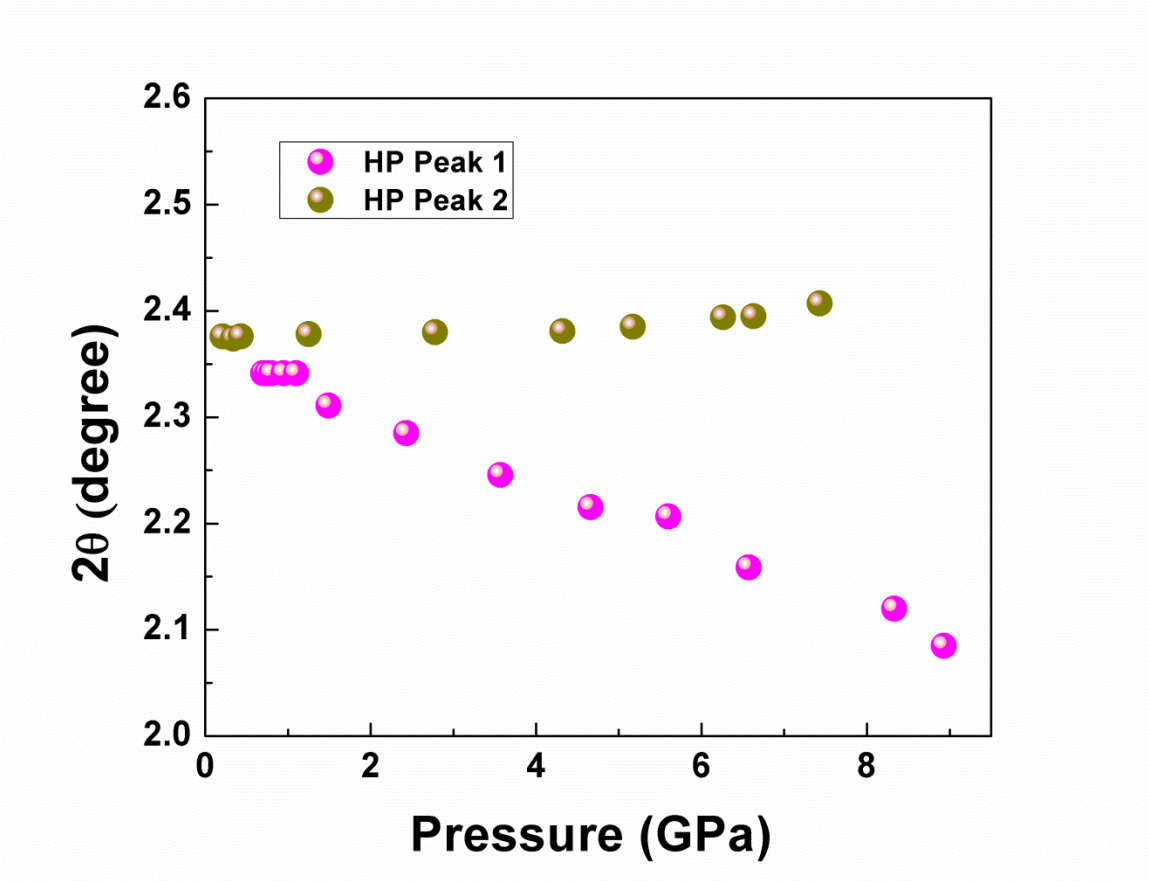

Figure 4.9. HP peak position changes upon the increase of pressure.

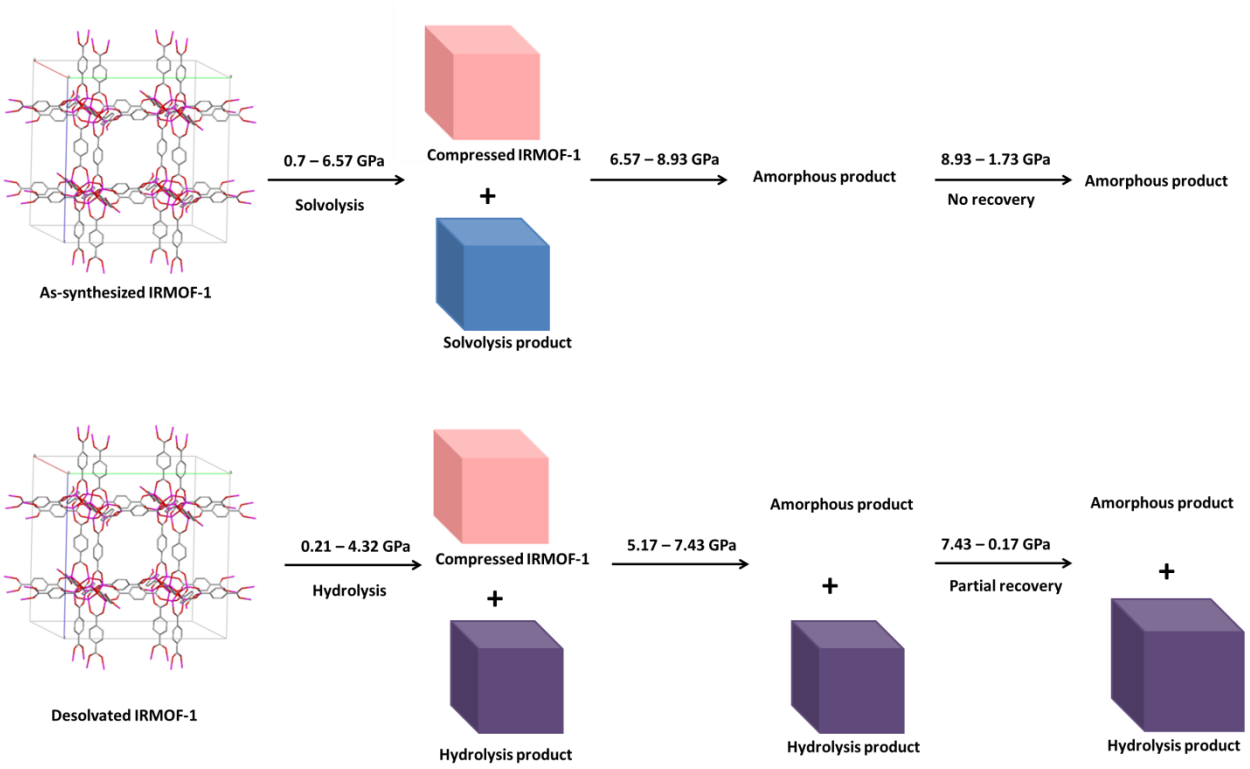

Scheme 4.1 Structural change of IRMOF-1 with increasing pressure

Experimental Section

Synthesis of IRMOF-1. IRMOF-1 crystals were synthesized by the solvothermal method. Zinc nitrate hexahydrate (156 mg, 0.60 mmol) and 1,4-benzenedicarboxylic acid (33 mg, 0.20 mmol) were dissolved in *N*,*N*-diethylformamide (10 mL) in a Teflon lined glass vessel. The vessel was kept at 90 ℃ for three days. The resulting cubic crystals were collected, and subjected to solvent exchange by soaking them in three successive solutions of chloroform over a period of one day. The chloroform was then decanted and the crystals were dried in an oven at 120 ℃ for one day to remove the remaining chloroform in the pores. The IRMOF-1 crystals were then crushed to a fine powder.

Powder X-ray diffraction data collection at ambient pressure. Studies of the air stability of IRMOF-1 were carried out by collecting powder X-ray diffraction (PXRD) data on a Bruker General Area Detector Diffraction System (GADDS) equipped with a P4 four-circle diffractometer and HiStar multiwire area detector. A Bruker M18XHF22 rotating anode generator operating at 50 kV and 60 mA supplied the Cu Kα (1.54056 Å) graphite monochromatized incident beam.

Powder X-ray diffraction data collection at high pressure. A Mao-bell type diamond anvil cell[21] equipped with a 800 μm culet diamonds was used for the *in situ* high pressure X-ray diffraction studies. A stainless steel gasket was preindented to a thickness of 90 μm, and a 250 μm diameter hole was drilled in the center of the indentation as a sample chamber. Pressures were determined by measuring the shift in the fluorescence energy of a ruby sphere loaded in the chamber along with the sample.[22] *In situ* angle dispersive X-ray diffraction experiments were performed at HPCAT beamline 16-BMD at the Advanced Photon Source (APS) at Argonne

National Laboratory with a focused monochromatic X-ray beam (λ = 0.4134 Å). Powder X-ray diffraction (PXRD) patterns were collected with a MAR345 imaging plate, and the experimental geometry was calibrated with a sample of NIST standard CeO_2 powder.

TOPAS analysis of diffraction patterns of IRMOF-1. The software program TOPAS was used to refine the powder diffraction patterns between 1 and 3.9 °(2θ). Each pattern was fit with a 6 fold Chebyshev polynomial background curve and pseudo-Voigt (PVII) or split-Pearson (SPVII) type peaks.[23]

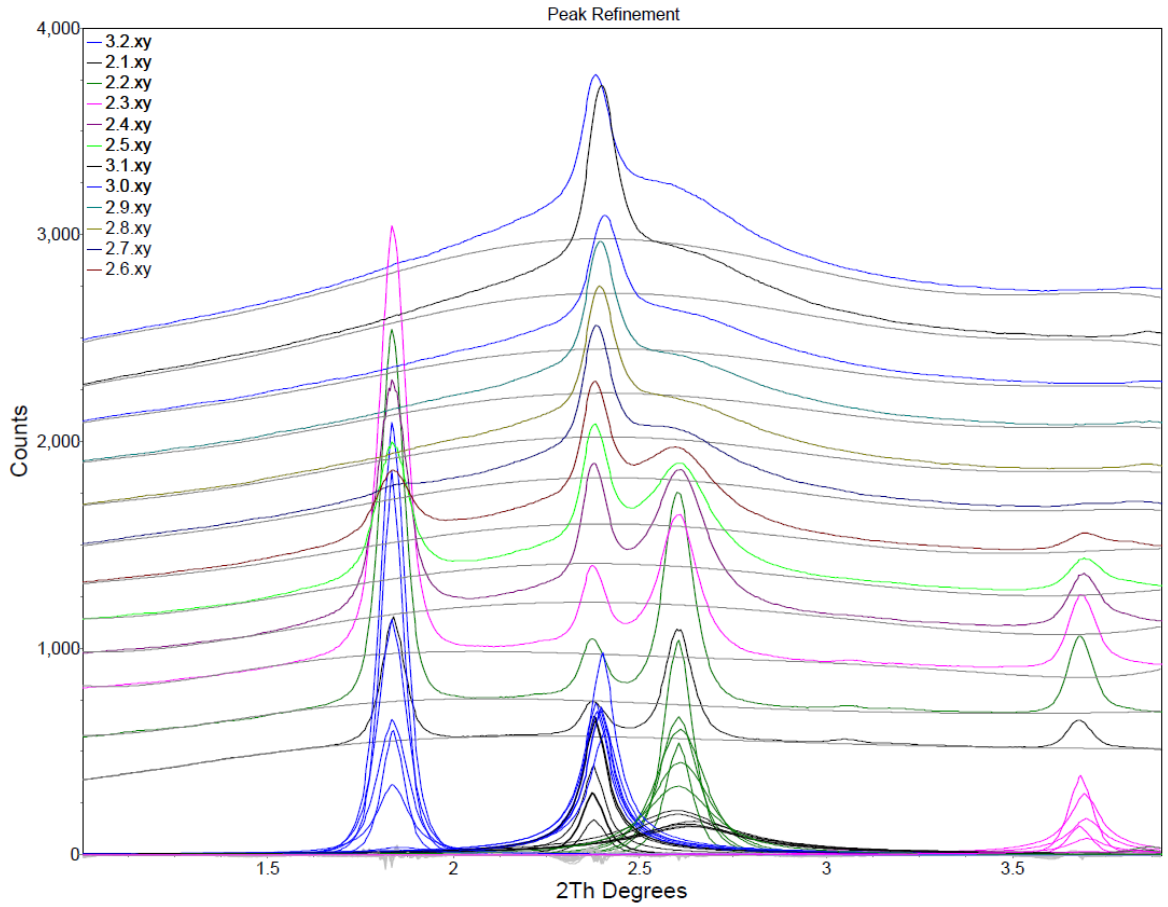

Figure 4.10. Illustration of the process to fit the PXRD patterns using TOPAS.

References

1. J. L. C. Rowsell, A. R. Millward, K. S. Park and O. M. Yaghi, *J. Am. Chem. Soc.*, 2004, **126**, 5666-5667.
2. D. J. Collins and H. C. Zhou, *J. Mater. Chem.*, 2007, **17**, 3154-3160.
3. Y. S. Bae, K. L. Mulfort, H. Frost, P. Ryan, S. Punnathanam, L. J. Broadbelt, J. T. Hupp and R. Q. Snurr, *Langmuir*, 2008, **24**, 8592-8598.
4. B. L. Chen, C. D. Liang, J. Yang, D. S. Contreras, Y. L. Clancy, E. B. Lobkovsky, O. M. Yaghi and S. Dai, *Angew. Chem., Int. Ed.*, 2006, **45**, 1390-1393.
5. A. J. Lan, K. H. Li, H. H. Wu, D. H. Olson, T. J. Emge, W. Ki, M. C. Hong and J. Li, *Angew. Chem., Int. Ed.*, 2009, **48**, 2334-2338.
6. C. D. Wu and W. B. Lin, *Angew. Chem., Int. Ed.*, 2007, **46**, 1075-1078.
7. D. F. Bahr, J. A. Reid, W. M. Mook, C. A. Bauer, R. Stumpf, A. J. Skulan, N. R. Moody, B. A. Simmons, M. M. Shindel and M. D. Allendorf, *Phys. Rev. B*, 2007, **76**, 184106-184113.
8. M. Kosa, J. C. Tan, C. A. Merrill, M. Krack, A. K. Cheetham and M. Parrinello, *ChemPhysChem*, 2010, **11**, 2332-2336.
9. J. C. Tan, T. D. Bennett and A. K. Cheetham, *Proc. Natl. Acad. Sci. U. S. A.*, 2010, **107**, 9938-9943.
10. J. C. Tan and A. K. Cheetham, *Chem. Soc. Rev.*, 2011, **40**, 1059-1080.
11. K. W. Chapman, G. J. Halder and P. J. Chupas, *J. Am. Chem. Soc.*, 2009, **131**, 17546-17547.
12. E. C. Spencer, R. J. Angel, N. L. Ross, B. E. Hanson and J. A. K. Howard, *J. Am. Chem. Soc.*, 2009, **131**, 4022-4026.

13. K. W. Chapman, G. J. Halder and P. J. Chupas, *J. Am. Chem. Soc.*, 2008, **130**, 10524-10526.

14. A. J. Graham, D. R. Allan, A. Muszkiewicz, C. A. Morrison and S. A. Moggach, *Angew. Chem., Int. Ed.*, 2011, **50**, 11138-11141.

15. S. A. Moggach, T. D. Bennett and A. K. Cheetham, *Angew. Chem., Int. Ed.*, 2009, **48**, 7087-7089.

16. M. Eddaoudi, J. Kim, N. Rosi, D. Vodak, J. Wachter, M. O'Keeffe and O. M. Yaghi, *Science*, 2002, **295**, 469-472.

17. Y. H. Hu and L. Zhang, *Phys. Rev. B*, 2010, **81**, 174103-117418.

18. http://www.esrf.eu/AboutUs/Upgrade/science/extremeconditions

19. S. R. Elliott, *Phys. Rev. Lett.*, 1991, **67**, 711-714.

20. S. S. Kaye, A. Dailly, O. M. Yaghi and J. R. Long, *J. Am. Chem. Soc.*, 2007, **129**, 14176-14177.

21. H. K. Mao, P. M. Bell, K. J. Dunn, R. M. Chrenko and R. C. Devries, *Rev. Sci. Instrum.*, 1979, **50**, 1002-1009.

22. H. K. Mao, J. Xu and P. M. Bell, *J. Geophys. Res.-Solid*, 1986, **91**, 4673-4676.

23. Bruker (2005). TOPAS Version 3. Bruker AXS, Inc., Madison, Wisconsin, USA.